

AN ABSTRACT OF THESIS OF

Patrick Byfield for the degree of Master of Science in Nuclear Engineering presented on June 7, 2013.

Title: A Thermal Hydraulics Analysis of a Molybdenum Production Element for Implementation in TRIGA[®] Reactors

Abstract approved: _____

Wade R. Marcum

The metastable isotope of technetium-99 (Tc-99m) is an important diagnostic tool used in the field of nuclear medicine due to the isotope's 6.0 hour half-life, 140.5 keV γ -decay mechanism, and multiple oxidation states [1,2]. Approximately 70% of the world's nuclear medicine procedures involve the use of Tc-99m [3]. The conventional source of Tc-99m comes from the β -decay of molybdenum-99 (Mo-99), an isotope which may be produced via the fission of uranium-235 (U-235) atoms [2].

As Mo-99 has a half-life of 2.7 hours [2]; it is difficult to produce anything but short-term stockpiles of Tc-99m. A handful of geographically dispersed facilities maintain a continuous production of Mo-99 via U-235 fission as a means to satisfy the demand of nuclear medicine worldwide [4]. However, 96% of all Mo-99 production is concentrated among only 4 facilities [4]. This centralized production dynamic has been shown to leave the world susceptible to Tc-99m shortages in the event of multiple reactor shutdowns [5].

Oregon State University (OSU) has undertaken a study to investigate the safety of implementing a fueled experiment, known as the "molybdenum element," within the OSU TRIGA[®] reactor (OSTR) for the purpose of producing Mo-99. This study investigates both steady-state and select transient conditions within the OSTR core with the use of the lumped parameter code RELAP5-3D version 2.4.2. Key thermal hydraulic parameters which may impact the safety of the OSTR are identified and presented, and discussed herein.

© Copyright by Patrick Byfield

June 7, 2013

All Rights Reserved

A Thermal Hydraulics Analysis of a Molybdenum Production Element for
Implementation in TRIGA[®] Reactors

by
Patrick Byfield

A THESIS
Submitted to
Oregon State University

in partial fulfillment of
the requirements for the
degree of
Master of Science

Presented June 7, 2013
Commencement June 2013

Master of Science thesis of Patrick Byfield presented on June 7, 2013.

APPROVED:

Major Professor, representing Nuclear Engineering

Head of the Department of Nuclear Engineering and Radiation Health Physics

Dean of the Graduate School

I understand that my thesis will become part of the permanent collection of Oregon State University libraries. My signature below authorizes release of my thesis to any reader upon request.

Patrick Byfield, Author

ACKNOWLEDGEMENTS

I would like to thank my advisor, Dr. Marcum, who has taught me so much through both instruction and example. I leave OSU a better person thanks to his lessons, guidance, and leadership.

I would like to thank the members of the OSU Molybdenum Production Project whose work is included within this study, Mr. Todd Keller, Ms. Madicken Munk, Dr. Todd Palmer, and Dr. Steve Reese.

I would like to thank my friends and colleagues in the OSU NE/RHP department. In particular, I would like to thank Mr. Timothy Adams, Mr. Robert Aldridge, Mr. John Utberg Jr., and Mr. Aaron Weiss.

Finally, I would like to thank my family for their support, my parents, De Yule, Clyde Byfield, Bridget Byfield, and my fiancée, Marissa Dubay.

TABLE OF CONTENTS

| <u>Section</u> | <u>Page</u> |
|---|-------------|
| 1 INTRODUCTION | 1 |
| 1.1 Purpose | 2 |
| 1.2 Objectives | 2 |
| 1.3 Document Overview | 4 |
| 2 LITERATURE REVIEW | 5 |
| 2.1 Medical Applications of Metastable Technetium-99 | 5 |
| 2.2 Production of Molybdenum-99 | 5 |
| 2.3 The Applications of RELAP5-3D to OSTR Modeling | 7 |
| 2.4 Natural Circulation | 8 |
| 2.5 Critical Heat Flux | 9 |
| 3 OREGON STATE TRIGA [®] REACTOR DESCRIPTION | 15 |
| 3.1 OSTR Fuel Rods | 18 |
| 3.2 Molybdenum Element Design | 19 |
| 3.3 Molybdenum Element Fuel Material Description | 22 |
| 3.4 Molybdenum Element Material Temperature Limits | 25 |
| 3.4.1 Shear Stress Limitation | 25 |
| 3.4.2 Internal Pressure Limitation | 26 |
| 4 RELAP5-3D MODEL | 29 |
| 4.1 Model Summary and Justification | 29 |
| 4.2 Model Description | 30 |
| 4.3 Calculated Form Losses | 34 |
| 4.4 Fuel Core Source Profiles | 38 |
| 4.5 Material Models and Description | 41 |
| 4.5.1 RELAP5-3D Model Thermal Conductivity Data | 41 |
| 4.5.2 RELAP5-3D Model Volumetric Heat Capacity Data | 44 |
| 5 RESULTS AND DISCUSSION | 47 |

| | | |
|-------|---|----|
| 5.1 | Steady-State Results | 47 |
| 5.1.1 | Thermal Hydraulic Characteristics at Full Power | 47 |
| 5.1.2 | Limiting Thermal Hydraulic Characteristics | 53 |
| 6 | CONCLUSION | 59 |
| 6.1 | Observations | 59 |
| 6.2 | Assumptions and Limitations | 61 |
| 6.3 | Future Work | 61 |
| 7 | REFERENCES..... | 63 |
| 8 | NOMENCLATURE..... | 69 |
| 9 | APPENDIX A: LOCA EVENT ANALYSIS | 73 |
| 9.1 | Description | 73 |
| 9.2 | Approach | 74 |
| 9.3 | Results | 75 |
| 9.4 | Closing..... | 87 |
| 10 | APPENDIX B: FLOW BLOCKAGE ANALYSIS | 90 |
| 10.1 | Description..... | 90 |
| 10.2 | Approach..... | 90 |
| 10.3 | Results..... | 90 |
| 10.4 | Closing..... | 98 |

LIST OF FIGURES

| <u>Figure</u> | <u>Page</u> |
|--|-------------|
| Figure 2-1: Sketch of ONB (left) and DNB (right)..... | 10 |
| Figure 3-1: Vertical section of TRIGA [®] Mark II Reactor [8,32]..... | 15 |
| Figure 3-2: Horizontal section of TRIGA [®] Mark II Reactor [8,32] | 16 |
| Figure 3-3: OSTR Normal core configuration [8,32] | 17 |
| Figure 3-4: Top-down representation of molybdenum element [47]..... | 20 |
| Figure 3-5: Axial representation of the molybdenum element [47]..... | 21 |
| Figure 3-6: An OSTR fuel rod and molybdenum element [47]..... | 22 |
| Figure 3-7: Sketch of molybdenum element fuel material packing..... | 23 |
| Figure 3-8: Sketch of internal pressure imposed on (a) outer clad and (b) inner clad. 26 | |
| Figure 3-9: Molybdenum element internal pressure as a function of temperature | 29 |
| Figure 4-1: Sketch of RELAP5-3D model..... | 30 |
| Figure 4-2: RELAP5-3D inner and outer channel sub-volumes | 32 |
| Figure 4-3: Sketch of flow sudden expansion (left) and sudden contraction (right) ... | 35 |
| Figure 4-4: Sketch of flow through outer and inner channels..... | 37 |
| Figure 4-5: MCNP5 calculated OSTR element power at 1.1 MW [48] | 39 |
| Figure 4-6: Axial power distribution of molybdenum element | 40 |
| Figure 4-7: Radial power distribution of molybdenum element..... | 40 |
| Figure 4-8: Thermal conductivity of aluminum..... | 43 |
| Figure 4-9: Thermal conductivity of fueled region materials | 43 |
| Figure 4-10: Volumetric heat capacity of aluminum | 45 |
| Figure 4-11: Volumetric heat capacity of helium | 45 |
| Figure 4-12: Volumetric Heat Capacity of UO ₂ vs. Temperature..... | 46 |
| Figure 5-1: Steady state - fuel temperature | 48 |
| Figure 5-2: Steady state - fuel temperature | 48 |
| Figure 5-3: Steady state - fuel material, axial hot band | 49 |
| Figure 5-4: Steady state - fuel material, radial hot band..... | 49 |
| Figure 5-5: Steady state - channel coolant temperature | 51 |
| Figure 5-6: Steady state - channel coolant velocity | 51 |
| Figure 5-7: Steady-state – CHF..... | 52 |

| | |
|--|----|
| Figure 5-8: Power variation - maximum fuel and clad temperature | 54 |
| Figure 5-9: Power variation - fuel material, axial hot bands..... | 55 |
| Figure 5-10: Power variation - fuel material, radial hot bands | 55 |
| Figure 5-11: Power variation – channel outlet coolant temperature | 56 |
| Figure 5-12: Power variation - channel outlet mass flow rate | 57 |
| Figure 5-13: Power variation - MCHFR | 58 |
| Figure 9-1: Decay power profile | 73 |
| Figure 9-2: LOCA event scenarios - maximum fuel temperature..... | 76 |
| Figure 9-3: LOCA event scenario I - fuel temperature at peak..... | 78 |
| Figure 9-4: LOCA event scenario I - fuel temperature at peak..... | 78 |
| Figure 9-5: LOCA event scenario II - fuel temperature at peak | 79 |
| Figure 9-6: LOCA event scenario II - fuel temperature at peak | 79 |
| Figure 9-7: LOCA event scenario III - fuel temperature at peak..... | 80 |
| Figure 9-8: LOCA event scenario III - fuel temperature at peak..... | 80 |
| Figure 9-9: LOCA event scenario IV - fuel temperature at peak..... | 81 |
| Figure 9-10: LOCA event scenario IV - fuel temperature at peak..... | 81 |
| Figure 9-11: LOCA event scenario I & II - fuel material, axial hot bands at peak..... | 82 |
| Figure 9-12: LOCA event scenario I & II - fuel material, radial hot bands at peak | 82 |
| Figure 9-13: LOCA event scenario III & IV - fuel material, axial hot bands at peak . | 83 |
| Figure 9-14: LOCA event scenario III & IV - fuel material, radial hot bands at peak | 83 |
| Figure 9-15: LOCA event scenario I & II - nitrogen temperature at peak..... | 85 |
| Figure 9-16: LOCA event scenario I & II - nitrogen velocity at peak..... | 85 |
| Figure 9-17: LOCA event scenario III & IV - nitrogen temperature at peak | 86 |
| Figure 9-18: LOCA event scenario III & IV - nitrogen velocity at peak..... | 86 |
| Figure 10-1: Blockage event - fuel temperature | 92 |
| Figure 10-2: Blockage event - fuel temperature | 92 |
| Figure 10-3: Blockage event - fuel material, axial hot band..... | 93 |
| Figure 10-4: Blockage event - fuel material, radial hot band | 93 |
| Figure 10-5: Blockage event - channel water temperature profile..... | 95 |
| Figure 10-6: Blockage event - channel water velocity profile..... | 95 |
| Figure 10-7: Blockage event - CHF | 97 |

LIST OF TABLES

| <u>Table</u> | <u>Page</u> |
|--|-------------|
| Table 2-1: Global molybdenum production as of 2009 | 6 |
| Table 3-1: Physical characteristics of OSTR fuel rods [32] | 18 |
| Table 3-2: OSTR fuel rod maximum temperatures [8,32]..... | 19 |
| Table 3-3: OSTR fuel rod and molybdenum element comparison [32]..... | 22 |
| Table 3-4: Molybdenum element fuel material characteristics..... | 24 |
| Table 3-5: Molybdenum element composition melting temperatures | 25 |
| Table 4-1: Molybdenum element and fuel rod calculated form loss values | 38 |
| Table 5-1: Steady-state results | 47 |
| Table 5-2: Power variation - steady-state results | 53 |
| Table 9-1: LOCA event scenario results | 74 |
| Table 9-2: LOCA event scenario maximum temperatures | 75 |
| Table 10-1: Blockage event results | 91 |

A Thermal Hydraulics Analysis of a Molybdenum Production Element for Implementation in TRIGA[®] Reactors

1 INTRODUCTION

The metastable isotope of technetium-99 (Tc-99m) is widely employed in the field of nuclear medicine; so much so that Tc-99m is used in approximately 70% of the world's nuclear medicine procedures [3]. Due to the relatively short half-life of Tc-99m (approximately 6.008 hours) along with its 140.5 keV gamma-ray decay mechanism, the isotope enables efficient detection and imaging when used in conjunction with modern medical diagnostics tools [1,2,6]. This metastable technetium isotope is produced by the beta-particle decay of molybdenum-99 (Mo-99), which has a half-life of 2.7476 days [6]. Due to the relatively short half-lives of these two isotopes, it is functionally and economically difficult to create anything but short-term stockpiles of Tc-99m; thus continuous production is needed to satisfy the demand for the isotope. This demand poses a unique problem to the nuclear medicine community. **Equation Section (Next)**

Oregon State University (OSU) has initiated a program to design a fueled experiment intended to serve as a means to produce quantities of Mo-99. The fueled experiment designed for this program, dubbed the "molybdenum element," is of a hollow annular design and has an overall length and width which allow for integration into the Oregon State TRIGA[®] (Training, Research, Isotopes, General Atomic) Reactor (OSTR) core. The design of the molybdenum element is composed of three main sections, the upper fitting, the lower fitting, and the clad-bound fueled region. The element's upper and lower end fittings are formed of aluminum. Within the fueled region of the molybdenum element, the interior annular region that comprises a quantity of 200 μm diameter uranium oxide (UO_2) micro-spheres; the fuel microspheres are contained by aluminum cladding which covers the molybdenum element's interior and exterior surface. Oregon State University intends to position up to three of these molybdenum

elements within the OSTR core and to perform a “proof-of-concept” on this design and technology.

1.1 Purpose

A safety analysis pertaining to the placement of molybdenum elements within the OSTR is to be completed using RELAP5-3D version 2.4.2, a code developed by the Idaho National Laboratory (INL) [7]. This version of RELAP5-3D has been previously used to perform safety analyses pertaining to the OSTR during its 2008 fuel conversion from highly enriched uranium (HEU) to low enriched uranium (LEU) fuel [8,9,10]. The safety analysis relating to the molybdenum element will characterize how the element will respond during deployment as a means to determine if that response lies within the OSTR’s conservative safety limit and limiting safety system setting. Currently, maximum fuel rod temperature is the sole safety limit of the OSTR; therefore, the maximum fuel temperature within the molybdenum element is assumed to be of significant relevance with regard to the element’s limiting characteristics.

1.2 Objectives

The objective of this study is to determine and characterize the thermal hydraulic aspects related to the safety of deploying up to three molybdenum elements within the OSTR core during normal, full power operations. Limiting thermal hydraulic parameters include (1) maximum fuel temperature, (2) maximum cladding temperature, and (3) critical heat flux (CHF) ratios during steady-state operation. Each of these limiting parameters are quantified, presented, and interpreted. This objective is accomplished using RELAP5-3D version 2.4.2 through the completion of the following tasks:

- Development of a model representative of a single molybdenum element within the OSTR using the most conservative flow channel geometry possible – the OSTR’s B ring “hot channel.”

- **Task Outcome:** This development produced a model that can be used to analyze thermal hydraulic parameters for a single molybdenum element when subject to a variety of conditions within the OSTR.
- Employment of the model to analyze the steady-state operation of a single molybdenum element within the OSTR using a steady element power input and steady-state conditions for the surrounding coolant in the OSTR pool.
 - **Task Outcome:** This analysis determined and characterized limiting thermal hydraulics parameters for the single molybdenum element during steady-state operations.
- Employment of the model to analyze a loss of coolant accident (LOCA) with a single molybdenum element within the OSTR to determine limiting thermal hydraulics parameters.
 - **Task Outcome:** This analysis determined and characterized the outcomes resulting from varying time windows between a reactor shutdown (SCRAM) of the OSTR core and a LOCA.
- Employment of the model to analyze a channel blockage event within the molybdenum element's inner channel at full power with a single molybdenum element within the OSTR to determine limiting thermal hydraulics parameters in the event of foreign object placement or boil-off inside the molybdenum element.
 - **Task Outcome:** This analysis demonstrated and characterized the outcomes resulting from the molybdenum element running at full power with heat removal taking place only on the molybdenum element's exterior surface via the outer channel.

To summarize, this work characterizes the thermal hydraulic behavior of molybdenum elements deployed within the OSTR core during steady-state operations of the OSTR, loss of coolant accident (LOCA) scenarios, and flow blockage events.

1.3 Document Overview

This document is organized as follows:

Chapter 1: Introduction – An introduction to the study’s focus and the motivation behind the work presented.

Chapter 2: Survey of Literature – A section containing the requisite background information needed to frame the study, presented as a survey of available literature on several topics including the medical applications of technetium-99m, the process of molybdenum production, the applications of RELAP5-3D to OSTR modelling, natural circulation, and critical heat flux.

Chapter 3: Oregon State TRIGA[®] Reactor Description – A thorough description of the OSTR with a focus on its potential application as molybdenum production facility.

Chapter 4: RELAP5-3D Description – An overview and discussion relating to the RELAP5-3D model developed to meet the objectives of this study.

Chapter 5: Results and Discussion – A presentation of RELAP5-3D model results and a discussion of the observed phenomena.

Chapter 6: Conclusions – A section containing concluding observations which relate to this study and to future work opportunities for improvement of applied methods and for opportunities to extend the applicability of predicted characteristics.

This document concludes with lists of referenced works, nomenclature and symbols, and appendices with additional details not contained within the chapters.

2 LITERATURE REVIEW

2.1 Medical Applications of Metastable Technetium-99

Technetium, discovered in 1937 by C. Perrier and E. Segre [11], is a metallic element with the atomic number 43 [2]. The metastable state of the element with an atomic mass of 99 atomic mass units (amu), Tc-99m, was discovered by E. Serge and G. Seaborg in 1937 [11]. To date Tc-99m is one of the most widely used isotopes in nuclear medicine applications around the world [11,3,4].

The widespread deployment of Tc-99m in the field of nuclear medicine is a direct result of three of the isotopes' most attractive characteristics – its multitude of oxidation states [3], its low gamma energy, or photon emission (140.5 keV) [2, 4], and its short half-life (approximately 6.01 hours) [2,4]. Specific examples of Tc-99m applications include brain imaging [12], tumor imaging [13,14], thyroid imaging [15], renal imaging [16], and joint imaging [17]. Tc-99m is considered as one of the key tools of modern nuclear medicine, serving as the imaging isotope for the large majority of diagnostic nuclear medical procedures performed worldwide each year (20-25 million as of 2004) [3,4]. Particular attention should be given to the role of Tc-99m in cardiology imaging procedures, which compose a large portion of all worldwide nuclear medicine procedures, which are performed almost entirely with Tc-99m [3]. [Equation Section \(Next\)](#)

2.2 Production of Molybdenum-99

As sufficient quantities of Tc-99m are not readily available for extraction from nature, a supply of the isotope must be produced by artificial means to satisfy the medical demand. Tc-99m may be produced from the β -decay of Mo-99, a fission product of U-235 with a half-life of approximately 2.75 days [2]. As such, supplies of Mo-99 have been produced over the last several decades by the neutron bombardment and subsequent fission of U-235 fuels or targets of both high and low enrichments [4,5]. Since the 1980's, the key source for the United States' supply of Tc-99m has come

from nuclear reactors located within Canada [11,18] which produced approximately 38% of the world's supply of Mo-99 as of 2009 [4].

Although there are Mo-99 production facilities located across at least three continents [4], approximately 96% of the world's supply of Mo-99 originates from only four facilities, as illustrated in Table 2-1 [4]. Because of this concentrated production dynamic, the shutdown of any one of the world's largest Mo-99 production facility may cause a significant drop in the supply of Tc-99m [5,18], as has been demonstrated in 2012 when the Canadian Nordion and the Tyco Healthcare facilities were taken offline [5]. In addition, rare cases of concurrent production reactor shutdowns are capable of drastically reducing the world's supply of Tc-99m, such as the 2008 multi-reactor shutdown which caused approximately 94% of the world's Mo-99 production to be offline for a period of several weeks [4].

Table 2-1: Global molybdenum production as of 2009

| Producer | Location | World Production [%] |
|-----------------|-----------------|----------------------|
| MDS Nordion | Canada | 38 |
| Tyco Healthcare | The Netherlands | 26 |
| IRE | Belgium | 16 |
| NTP | South Africa | 16 |

Radioisotope drug shortages caused by reactor shutdowns may have serious effects on the ability of doctors to adequately treat patients [5], and due to Mo-99's relatively short half-life (approximately 2.7 days), it is very difficult to create a Mo-99 stockpile which could prevent Tc-99m shortages when reactor shutdowns occur [18]. For years, the International Atomic Energy Agency (IAEA) and governments around the world have been attempting to combat Tc-99m shortages by moving forward on plans to construct new reactors and by converting existing reactors for the purpose of Mo-99 production [4,5,18]. Alternative approaches to Mo-99 production have also been considered via the neutron bombardment of Mo-98 [2], a naturally occurring stable isotope, with the use of high flux reactors or accelerators [4]. However, the economic

cost and requisite time needed for the construction or conversion of Mo-99 production facilities has historically been prohibitive [5,18].

An approach which could allow for existing reactors to produce Mo-99 without extensive conversions would provide a more dispersed and less economically volatile supply of Mo-99 in addition to requiring less investment. In addition, a dispersed Mo-99 production approach could help alleviate processing and delivery delays associated with concentrated large-scale Mo-99 production facilities, which occur due to the physical distances between Mo-99 production facilities, Mo-99 processing facilities, and patients, all of which may or may not reside in the same country or region [4]. A potential “dispersed” Mo-99 production approach may be implemented through use of TRIGA[®] Reactors, which are located throughout numerous regions of the world. This study seeks to characterize the thermal hydraulic aspects of utilizing a molybdenum element design for production of Mo-99 in the OSTR using RELAP5-3D.

2.3 The Applications of RELAP5-3D to OSTR Modeling

RELAP5-3D Version 2.4.2 is a lumped parameter code developed by the INL which may be utilized in simulations of both nuclear and nonnuclear systems involving thermal hydraulic transients of liquids, vapors, and non-condensable gas mixtures [7]. The RELAP5-3D code has been employed to simulate reactors of all different designs all around the world, examples of which include the Gas Fast Reactor (GFR) design by the INL [19], the Syrian Miniature Neutron Source Reactor (MNSR) [20], the Tehran Research Reactor [21], and the Ignalina (Lithuania) Reaktor Bolshoy Moshchnosti Kanalnyi (RBMK) [22]. In addition, RELAP5 has been used to simulate various TRIGA[®] (Training, Research, and Isotope Production General Atomic) reactors from around the world with much success, including the Pennsylvania State TRIGA[®] reactor [23], the Instituto de Pesquisas Radiativas – Reactor 1 (IPR-R1) TRIGA[®] reactor in Brazil [24], the UC Davis McClellan Nuclear Radiation Center (MNRC) TRIGA[®] reactor [25], the Reattore Casaccia-1 (RC-1) TRIGA[®] reactor in Italy [26], and the Oregon State TRIGA[®] Reactor [8].

Prior to the 2008 OSTR fuel conversion, a RELAP5-3D thermal hydraulic analysis was performed to determine various parameters of relevance to reactor's safety in multiple reactor configurations and operating conditions [8]. This Nuclear Regulatory Commission (NRC)-accepted study explored both steady-state and rapid reactivity transient ("pulse") analyses [8]. This study concluded that a RELAP5-3D steady-state analysis produced a conservative set of results, consistent with previous analyses of the OSTR, and that a similar pulse analysis produced results within a reasonable margin of error [8]. These conclusions are the key motivation for a RELAP5-3D analysis of Molybdenum Elements loaded within the OSTR.

2.4 Natural Circulation

A form of convection characterized by a lack of imposed force (force supplied with the use of active components such as pumps or blowers), natural circulation is a gravity-driven phenomenon caused by heating a volume of fluid from below while cooling it from above [27,28,29]. Natural circulation occurs by the formation of a density gradient within a fluid, and in the case of nuclear reactors, the density gradient is created by the heat produced via nuclear fission events within the core region, and the cooling capability is provided by the heat sink (heat exchangers, steam generators, etc.) [29]. The single-phase natural circulation of light water provides cooling to the OSTR, wherein the fluid is heated by fuel rods near the bottom of the reactor pool and cooling is provided by heat rejection to the atmosphere [8,31,32].

Oscillations may arise in natural circulation flows, including steady-state flows, which may lead to instabilities and flow reversals [29]. Because the ability of a moving fluid to remove heat from a stationary solid is highly dependent on the mass flux of that fluid [33], sudden changes in flow conditions within natural circulation flows may have a large effect on the heat removal capabilities of liquid water to cool a nuclear fuel rod. It is therefore important to analyze the behavior of natural circulation systems

to determine and characterize the likeliness and consequence of events which may disrupt steady-state flows.

2.5 Critical Heat Flux

As previously mentioned, in a natural circulation reactor such as the OSTR, the localized heating of water near the fuel rods results in a density gradient which allows for circulation to occur without the aid of active components; the hydraulic driving force is supplied by the reactor itself [34]. When operating at elevated power levels, the fuel temperature increases, thus increasing the heat flux between the fuel cladding and surrounding fluid. When the external cladding has reached temperatures near the saturation temperature of the liquid moderator, nucleate boiling will begin to occur, a transition referred to as the onset of nucleate boiling (ONB) [35]. During nucleate boiling, small bubbles are formed upon the external cladding, allowing both vapor and liquid to remain in contact with the rod [36]. The fluid disturbances caused by bubble formation are sufficient to lower the thermal resistance of the more thermally insulating vapor regions [35]; in addition, localized boiling further enhances the fluid's cooling ability, as additional energy is drawn from the cladding due to the fluid's phase change and removal of latent heat.

As fuel temperature increases further, the heat flux will increase, eventually causing departure from nucleate boiling (DNB) or "burnout," wherein the coalescence of bubbles forms an insulating vapor blanket around the heated fuel rod [35,36,37]. This heat flux, which leads to vapor blanket formation, is known as the critical heat flux (CHF) and will lead to a sudden rise in fuel temperature due to the vapor blanket's high thermal resistance [35,36,37]. A graphical depiction of ONB and DNB is given in Figure 2-1.

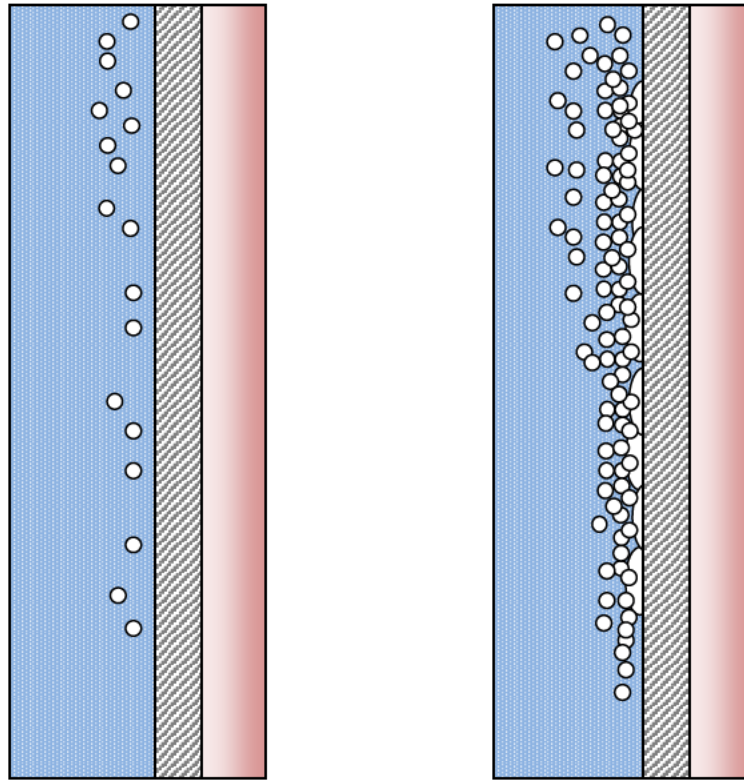


Figure 2-1: Sketch of ONB (left) and DNB (right)

The fuel temperature spike caused by DNB may result in fuel or cladding damage, which may then lead to a release of radionuclides, and is thus of great importance with regard to the operation of nuclear facilities [33,35,37]. Though significant work has been undertaken to quantify the heat-transfer which occurs in light water convection post-CHF conditions [33,35,38], this study focuses on determining the onset conditions of CHF such that an objective determination regarding the safety of the OSTR may be made by investigating the implementation of molybdenum elements within the core.

RELAP5-3D tabulates and reports CHF ratios (CHFRs) by sourcing the 1986 CHF look-up table [36] as its default source, though user specifications allow for tabulations with other CHF data sources [39]. Since 1986, the Atomic Energy of Canada Ltd. – University of Ottawa (AECL-UO) has updated the empirical reference data in the look up tables twice, in 1995, and again in 2006 [33,41]. These updated

databases are desirable sources for CHF predictions due to the abundance of empirical data that is available within them, lending to additional credibility beyond that of other potential empirical correlations [33,41].

CHF values presented within the 2006 look-up table are functions of pressure, mass flux, and equilibrium quality [33]. A CHF value may be interpolated from the table for any range of these three values which lie within the domain of the table. Once an interpolated value has been obtained from a look-up table, correction factors, denoted as k_1 through k_6 , must be included to accurately convert the interpolated value to one which relates to the geometry of the system. CHF values (kW/m) from the 2006 look-up table are calculated as [36,48]:

$$CHF = k_1 \cdot k_2 \cdot k_3 \cdot k_4 \cdot k_5 \cdot k_6 \cdot CHF_{\text{interpolated}} \quad (2-1)$$

where

$$k_1 = \left(\frac{8}{D_h} \right)^{1/2} \quad \text{for } 2 < D_h < 16 \quad (2-2)$$

$$k_2 = \min \left[0.8, 0.8 \exp(-0.5X^{1/3}) \right] \quad (2-3)$$

and

$$k_4 = \exp \left(\frac{D_H}{L} \exp \left(2 \left(\frac{X}{X + \frac{\rho_g(1-X)}{\rho_f}} \right) \right) \right) \quad (2-4)$$

note that k_1 represents the diameter factor, k_2 represents the rod-bundle geometry factor, k_3 represents the grid spacer factor, k_4 represents the heated length factor, k_5 represents the axial flux distribution factor, k_6 represents the vertical flow factor, D_h represents the hydraulic diameter (m), X represents the fluid equilibrium quality, D_H represents the hydraulic diameter (m), L represents the heated length from the channel inlet (m), ρ_g represents the density of the vapor (kg/m^3), and ρ_f represents the density of the fluid (kg/m^3). Note that for the cases presented within this study, k_3 , k_5 , and k_6 are assumed to be unity [36,48].

Other CHF correlations have been developed through both empirical and theoretical means. However, most of the empirical data sets are limited by traits of the experimental equipment used in their production, and as such may not be applicable to non-identical conditions. A second traditionally referenced source when predicting CHF with regards to TRIGA[®] reactors is the Bernath correlation [37], which has a history of application TRIGA[®] reactors and was presented in the original OSTR Safety Analysis Report (SAR) [8,36]. Previous examinations of CHF within TRIGA[®] reactors have concluded that a combined application of the 2006 CHF look-up table and the Bernath correlation produces the most conservative and credibly updated predictive values for those specific conditions which relate to TRIGA[®] reactors when compared with other relevant correlations, and previous versions of the CHF look-up tables [8,36].

CHF values (W/m^2) from the Bernath correlation are calculated as [36,37,48]:

$$\left(\frac{Q}{A}\right)_{BO} = 56.68 h_{BO} (T_w - T_b)_{BO} \quad (2-5)$$

where [36,37,48]

$$h_{BO} = 10,890 \left(\frac{D_h}{D_h - D_H} \right) + \Delta v, \quad (2-6)$$

$$\Delta = \begin{cases} \left(\frac{48}{D_h^{3/5}} \right) & \in D_h \leq 0.1 \\ \left(\frac{10}{D_h} \right) + 90 & \in D_h \geq 0.1 \end{cases} \quad (2-7)$$

and

$$T_w = 57 \ln(P_{abs}) - 54 \left(\frac{P_{abs}}{P_{abs} + 15} \right) - \frac{v}{4}. \quad (2-8)$$

Note that $(Q/A)_{BO}$ represents the critical heat flux (W/m^2), h_{BO} represents the limiting film coefficient ($\text{W}/\text{m}^2 \cdot ^\circ\text{C}$), T_w represents the temperature of the wall at CHF ($^\circ\text{C}$), T_b represents the bulk temperature of the fluid ($^\circ\text{C}$), D_h represents the hydraulic diameter

(m), D_H represents the heated diameter (m), Δ represents the slope, P_{abs} represents the absolute pressure (Pa), and v represents the velocity of the fluid (m/s).

In addition to the 2006 AECL-UO look-up tables and the Bernath correlation, the Hall-Mudawar correlation has been considered within this study. This correlation presents CHF as a function of Weber number, liquid and gas densities, surface tension, equilibrium quality, heated length, and heated diameter [42]. Evaluations of the Hall-Mudawar correlation have concluded that it, along with the 2006 AECL-UP look-up tables, provide reliable results when applied to research reactors with pressure ranges from 0.101 MPa to 5.05 MPa [43].

The Hall-Mudawar correlation calculates CHF values as [42]:

$$\frac{q_c}{Gh_{fg,o}} = \frac{C_1 We_D^{C_2} \left(\rho_f / \rho_g\right)^{C_3} \left[1 - C_4 \left(\rho_f / \rho_g\right)^{C_5} X_{i,*}\right]}{1 + 4C_1 C_4 We_D^{C_2} \left(\rho_f / \rho_g\right)^{C_3 + C_5} (L/D_H)} \quad (2-9)$$

with [42,43]

$$We = \left(\frac{G^2 D_H}{\rho_f \sigma} \right) \quad (2-10)$$

$$X_{i,*} = \left(\frac{h_i - h_{f,o}}{h_{fg,o}} \right) \quad (2-11)$$

and

$$C_1 = 0.0722$$

$$C_2 = -0.312$$

$$C_3 = -0.6644$$

$$C_4 = 0.900$$

$$C_5 = 0.724$$

Note that q_c represents the critical heat flux (kW/m^2), G represents the mass flux ($\text{kg/m}^2\text{-s}$), h_i represents the enthalpy at the inlet, $h_{f,o}$ represents the enthalpy at the outlet, $h_{fg,o}$ represents the latent heat of vaporization at the outlet (kJ/kg), σ represents

the surface tension (N/m), L represents the heated length (m), and D_H represents the heated diameter.

3 OREGON STATE TRIGA[®] REACTOR DESCRIPTION

Located in Corvallis, Oregon, the OSTR is a Mark II design TRIGA reactor licensed to a steady-state power level of 1.1 MW_{th} [8,32]. The reactor is of a pool-type design, which includes a 0.6 m tall, 1.07 m diameter core submerged beneath a 1.98 m diameter, 6.09 m deep pool of light water as detailed in Figure 3-1 [8]. The pool itself is clad with a layer of aluminum and surrounded by a layer of concrete which serves as a biological shield [44]. The OSTR Irradiation facilities utilize in-core positions, the core-adjacent rotating rack, the pneumatic transfer system, two of the reactor's four beam ports, thermal neutron column, and thermalizing column detailed in Figure 3-2 [44]. The core itself, shown in Figure 3-3, is of a cylindrical layout containing low-enriched uranium (LEU) stainless steel-clad uranium-zirconium hydride (UZrH) 30/20 fuel rods [32]. In addition, the core contains stainless steel-clad reflector elements, three fuel-followed electro-servo driven control rods, one void-followed pneumatically driven control rod, and several experimental positions [8,32]. **Equation Section (Next)**

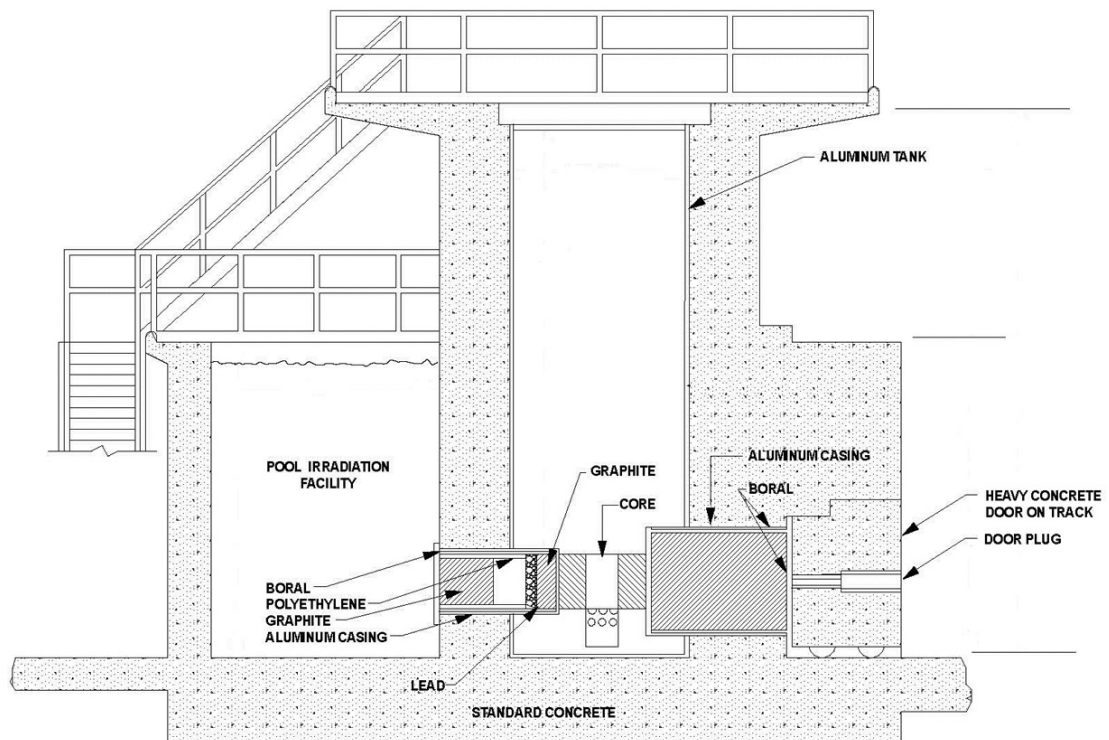


Figure 3-1: Vertical section of TRIGA[®] Mark II Reactor [8,32]

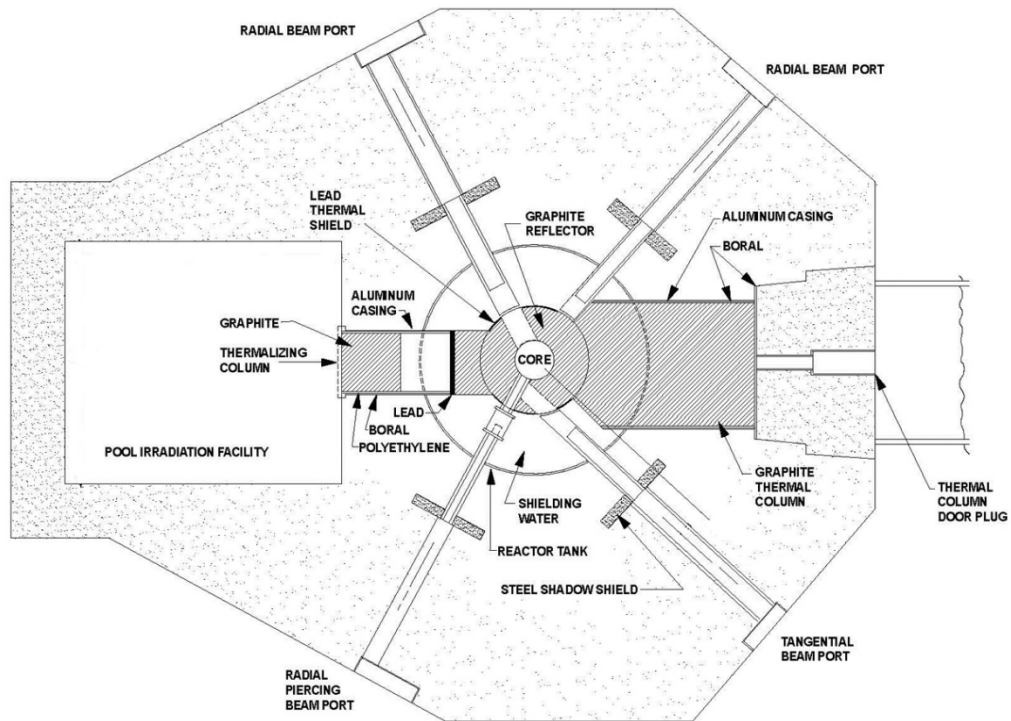


Figure 3-2: Horizontal section of TRIGA[®] Mark II Reactor [8,32]

As shown in Figure 3-3, the core layout is composed of cylindrical “rings” labeled A (central position) through G (outer ring), which contain the fuel rods, control rods, and other core elements [32]. Due to the size of elements within the core and the core’s overall dimensions, subchannel flow areas are not consistent throughout the core [8].

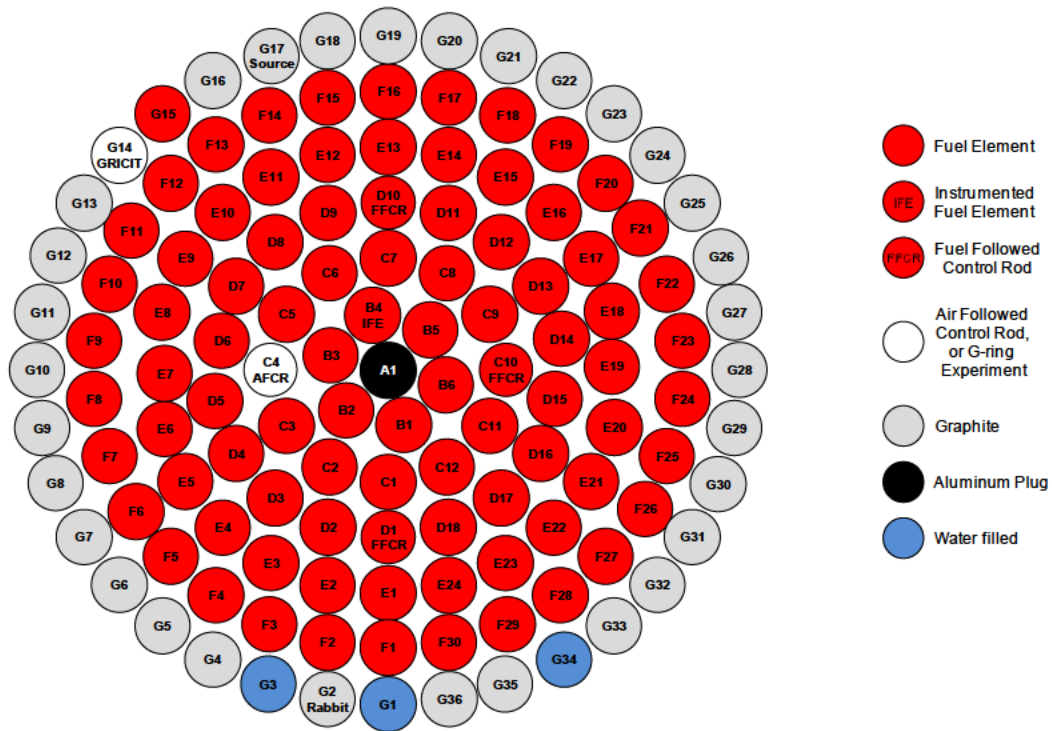


Figure 3-3: OSTR Normal core configuration [8,32]

The lanthanoid erbium (Er) is a metallic element which provides a strong negative temperature feedback (an effect which acts to reduce the likelihood of fission events within the fuel through erbium's increase in ability to absorb neutrons) when added to uranium fuels even in small quantities [2,45]. The inclusion of 1.1 mass percent erbium [32] and a single void-followed pneumatic “transient” control rod, which may be physically ejected from the core via a pneumatic system [32], endow the OSTR with the capability to pulse [8]. During a pulse, the reactor power and fuel temperatures reach elevated levels very rapidly due to the sudden removal of negative reactivity through pneumatic ejection of the transient control rod from the core region. It has been calculated that the reactor, in its current “beginning of life” (BOL) state, reaches a maximum power level of 4138.70 MW_{th} and a maximum fuel temperature of 835.90°C during a \$2.00 reactivity pulse [8,32,46]. Although the OSTR core as a whole has been designed with the ability to pulse, it is not the intent of the reactor administration to perform pulsing operations when the molybdenum elements are

located within the core, and therefore a pulsing analysis has been excluded from this study.

3.1 OSTR Fuel Rods

The LEU fuel rods contained within the OSTR core are composed of UZrH within stainless steel cladding [32,47]. Each rod contains a fueled length between two graphite reflectors (upper and lower), and terminates at each end with a stainless steel fitting which facilitates integration with the reactor grid plates [32]. The physical characteristics of the OSTR fuel rods are detailed in Table 3-1 below.

Table 3-1: Physical characteristics of OSTR fuel rods [32]

| Parameter | Description |
|---------------------------------------|-----------------|
| Fuel material | UZrH 30/20 fuel |
| Uranium content [mass %] | 30 |
| Fuel enrichment [mass % U^{235}/U] | 19.75 |
| Erbium content [mass % Er] | 1.1 |
| Cladding material | SS 304 |
| Cladding thickness [mm] | 0.508 |
| Gap thickness [mm] | 0.05 to 0.4 |
| Active length [mm] | 381 |
| Upper reflector Length [mm] | 87.38 |
| Lower reflector Length [mm] | 88.138 |
| External diameter [mm] | 37.465 |

The fuel-related safety limit imposed upon the OSTR by its technical specifications pertains to maximum fuel rod temperature, which may not exceed 1150 °C under any mode of operation [32]. This limit is enacted to ensure that cladding failure, which may result in a release of fission fragments, will not occur by pressure buildup within a high temperature fuel rod [32]. Although many factors contribute to the internal pressure within a fuel rod, fuel temperature is a single value that may be easily measured during operations [32].

The OSTR core is presently licensed to be arranged in any one of three core configurations – the Normal configuration, in-core irradiation tube (ICIT)

configuration, and cadmium-lined ICIT (CLICIT) configuration [32]. These configurations vary by the placement of elements in the B1 position. The thermal hydraulic characterization performed for the OSTR 2008 fuel conversion SAR examined each core configuration during the core’s BOL, “middle-of-life” (MOL), and “end-of-life” (EOL) phases [8,32]. A summary of maximum fuel temperature of the ICIT core at each discrete point in the core’s life during steady and pulsed mode tabulated during the 2008 study is shown in Table 3-2.

Table 3-2: OSTR fuel rod maximum temperatures [8,32]

| OSTR Configuration | Maximum Fuel Temperature [°C] |
|------------------------|-------------------------------|
| Steady-state, BOL ICIT | 448.13 |
| Steady-state, MOL ICIT | 457.66 |
| Steady-state, EOL ICIT | 438.38 |
| \$2.00 pulse, BOL ICIT | 835.90 |
| \$2.00 pulse, MOL ICIT | 1016.20 |
| \$2.00 pulse, EOL ICIT | 967.40 |

Table 3-2 illustrates that fuel temperatures are well within acceptable ranges with regard to technical specifications during steady-state operation, and that elevated temperatures reached during pulse conditions do not exceed values higher than approximately 88% of the technical specifications limit [8,32]. The OSTR is designed with a limiting safety system setting that prevents fuel rod temperature excursions beyond 510°C in non-pulse scenarios [32]. The maximum fuel temperatures given in Table 3-2 and the limiting safety system setting values provide reference values with regards to acceptable molybdenum element temperatures during implementation within the OSTR.

3.2 Molybdenum Element Design

The molybdenum element is of a hollow annular design, as illustrated in Figure 3-4 and Figure 3-5, which allows for coolant to flow via natural convection through a cylindrical inner channel and outer channel. It should be noted that the inner channel contains tri-supports at two axial locations along its length near the lower and upper

end fittings, respectively. The element's dual-channel design allows for heat transfer from within the element's fuel material to occur in both radial directions through the inner and outer aluminum cladding. Additionally, the element's design facilitates a fuel material geometry with a high surface area to volume ratio. The combination of these two features provides substantial cooling of the molybdenum element's fuel material.

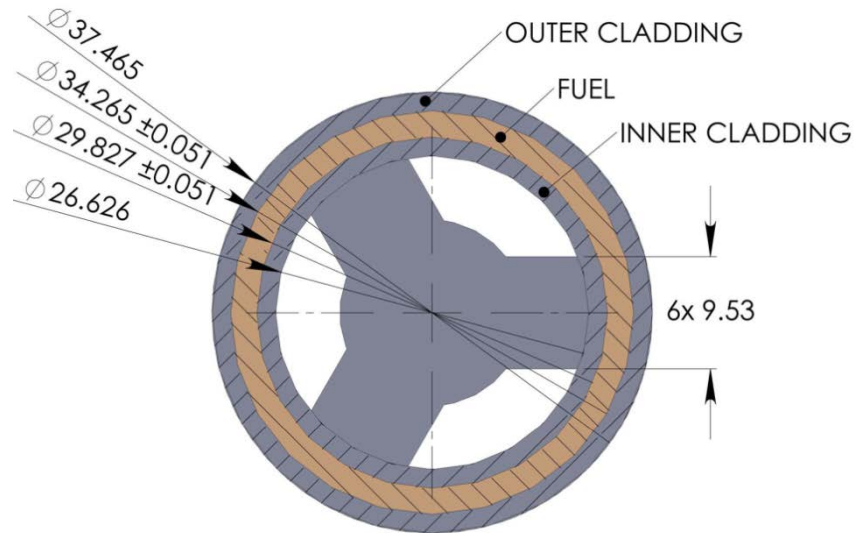


Figure 3-4: Top-down representation of molybdenum element [47]

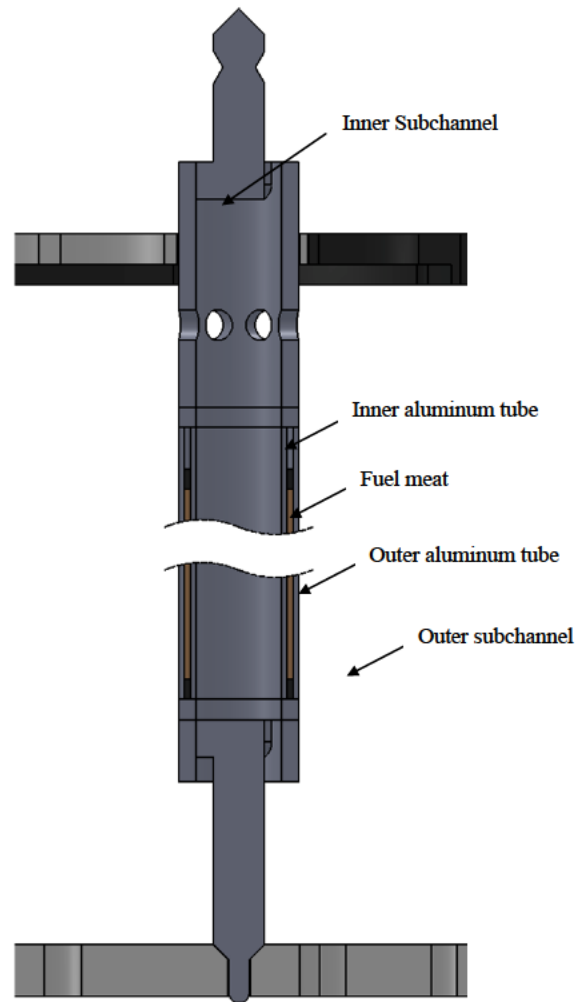


Figure 3-5: Axial representation of the molybdenum element [47]

The molybdenum element is designed with external dimensions nearly identical to those of an OSTR fuel rod to allow for equivalent outer cooling channel geometries. While the end fittings of a molybdenum element are identical to those of an OSTR fuel rod, the molybdenum element design does not include the upper and lower fins present on OSTR fuel rods. The design of the molybdenum element allows for compatibility within a standard OSTR grid location between the upper and lower grid plates. As such, the molybdenum element's design could in future application, mechanically allow for placement within any grid location of the core. A comparison of the geometry and composition of a molybdenum element and an OSTR fuel rod is shown in Table 3-3 and Figure 3-6.

Table 3-3: OSTR fuel rod and molybdenum element comparison [32]

| Parameter | OSTR Fuel Rod | Molybdenum Element |
|---|---------------|--------------------|
| Fueled Region Material | UZrH | UO ₂ |
| Fuel Enrichment [mass% U ²³⁵ /U] | 19.75 | 20 |
| Erbium Content [mass %] | 1.1% | -- |
| Cladding Material | SS 304 | Aluminum |
| Cladding Thickness [mm] | 0.508 | 3.2004 |
| Gap Thickness [mm] | 0.05 to 0.4 | -- |
| Active Length [mm] | 381 | 418.1 |
| Upper Reflector Length [mm] | 87.38 | -- |
| Lower Reflector Length [mm] | 88.138 | -- |
| External Diameter [mm] | 37.465 | 37.465 |

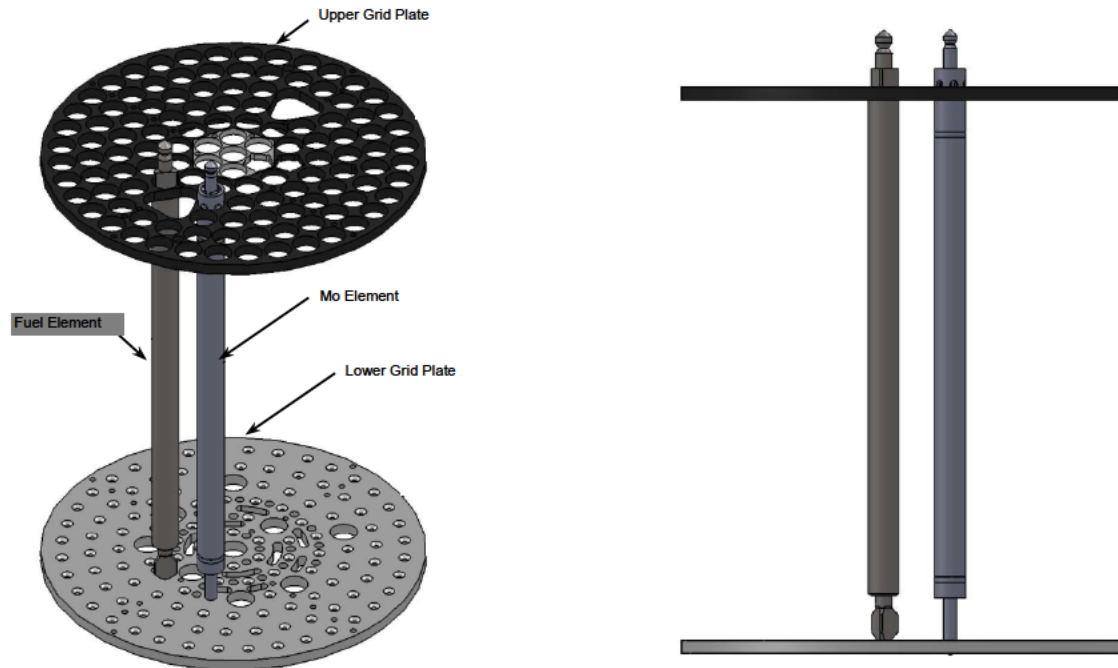


Figure 3-6: An OSTR fuel rod and molybdenum element [47]

3.3 Molybdenum Element Fuel Material Description

The molybdenum element fuel material design comprises 200 μm UO₂ microspheres of an assumed 20 % enrichment with an air fill gas. This region is radially bound by aluminum cladding and axially contained by an upper and lower aluminum washer [48]. The geometries of sphere-type fuels vary in several aspects from those of solid

fuel forms [49]. The most obvious difference is the overall density of the fuel material due to the limitations of sphere packing, as spheres of any volume will settle in a fashion which will produce gas-filled regions, as illustrated in an exaggerated fashion in Figure 3-7.

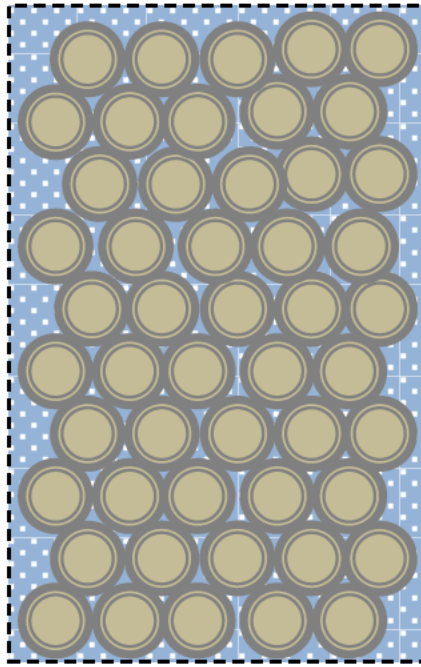


Figure 3-7: Sketch of molybdenum element fuel material packing

The ratio of volume encompassed by solid spheres to the volume encompassed by the gas-filled regions is known as the packing factor. The packing factor has a large impact on the overall density of a sphere-pac material. Studies which examined the packing of 200 μm spheres have measured packing factors applicable to the molybdenum element's fuel material region. In one particular study, the packing factors were found to range from 0.661 to 0.676 [50]. As a result, calculations within this safety analysis will assume that the conservative packing factor of 0.676 will occur within the element's fuel core, and that UO_2 has a density of approximately $10.9\text{E}3 \text{ kg/m}^3$ at temperatures ranging from 300 to 500 K [51]. The higher packing factor is assumed to be more conservative as it increases local fuel loading and

therefore increases power density, which results in relatively larger temperatures when compared to lower power densities.

The total height of the fuel material region is derived from the total microsphere loading held to a nominal mass of 800 grams of UO₂ microspheres per molybdenum element. Given this constraint, the total volume of the element's fuel material may be tabulated by dividing the nominal mass of the fuel material by the density of the fuel. This fuel density is found by multiplying the packing factor by the density of solid UO₂. The volume may then be converted to a fuel height by assuming a fuel area of

$$A_{fuel\ core} = \frac{\pi(D_{outer}^2 - D_{inner}^2)}{4}, \quad (3-1)$$

note that $A_{fuel\ core}$ is the total cross sectional area of the inner fueled region (m²), D_{outer} is the outer diameter of the fueled region (m), given in Figure 3-4 as 34.265 ± 0.051 mm, and D_{inner} is the inner diameter of the fueled region (m), given in Figure 3-4 as 29.827 ± 0.051 mm. By assuming a minimum value for D_{outer} and a maximum value for D_{inner} , the fuel area is found to be 218.26 mm². This area corresponds to a fuel core height of 496.79 mm. A geometric description of the element's fuel core is given in

Table 3-4.

Table 3-4: Molybdenum element fuel material characteristics

| Fuel Core Parameter | Value |
|---|-----------------|
| Fuel Material | UO ₂ |
| Enrichment [mass % U ²³⁵ /U] | 20 |
| Erbium Content [mass %] | 0 |
| Micro-sphere Diameter [μm] | 200 |
| Total Uranium Mass [g] | 800 |
| Fill Gas | Helium |
| Packing Factor | 0.676 |
| Solid Fuel Density [g/cm ³] | 10.9 |
| Total Fuel Density [g/cm ³] | 7.37 |
| Total Fuel Volume [cm ³] | 108.55 |
| Annular Fuel Area [cm ²] | 2.18 |
| Total Fuel Height [cm] | 49.79 |

3.4 Molybdenum Element Material Temperature Limits

Any comprehensive reactor safety study regarding the implementation of a core element must consider both the impact of the element on the reactor in reference to licensed limits, such as the OSTR fuel temperature safety limit of 1,150°C [32]; as well as the reactor's impact on the element. As a result of inherent design features, the molybdenum element differs in both form and composition from standard OSTR fuel rods as discussed in Section 3.2 and will therefore exhibit different limitations related to failure. In this study, the failure of the molybdenum element refers to any event which corresponds with a breach of the molybdenum element's aluminum clad.

Mechanisms of relevance to element failure include, but are not limited to, clad failure due to melting, clad failure due to stress-induced deformation, and clad failure due to rupture caused by the internal pressures of the fill gas. Composition temperatures which exceed melting temperatures may indicate molybdenum element failure, described as any event which corresponds with a breach of the aluminum clad. As such, safe implementation of molybdenum elements corresponds with maximum composition temperatures below melting temperatures. Relevant melting temperatures gathered from reference materials are presented in Table 3-5 [51,52].

Table 3-5: Molybdenum element composition melting temperatures

| Material | Function | Melting temperature [°C] |
|-----------------|---------------|--------------------------|
| UO ₂ | Fuel | 2856 ± 30 |
| Aluminum | Cladding | 660 |
| Air | Fuel fill gas | -- |

3.4.1 Shear Stress Limitation

The flow of liquid coolant within a molybdenum element's inner and outer channels will impose shear stresses upon the aluminum cladding [53]. Given that the natural

circulation fluid velocity of coolant passing adjacent to standard OSTR fuel rods has been found to be small [8,32], the magnitude of the associated shear stress imposed by the fluid on the cladding is also expected to be small. As aluminum alloys require high stress levels to exhibit shear effects even at temperatures up to 316°C [54], shear stress induced deformation will not be assumed to be a failure mechanism of relevance in this analysis.

3.4.2 Internal Pressure Limitation

Any positive temperature change which occurs within a molybdenum element's fuel core will cause thermal expansion within both the fuel spheres and surrounding fill gas. This expansion results in an increase of internal molybdenum element pressure and thus subjects the element's aluminum clad to elevated pressure levels. Stresses imposed by elevated pressures may result in material yielding if the magnitude of stress overcomes the elastic limit yield strength of the aluminum. The pressure imposed upon both the inner clad and outer clad is illustrated in Figure 3-8.

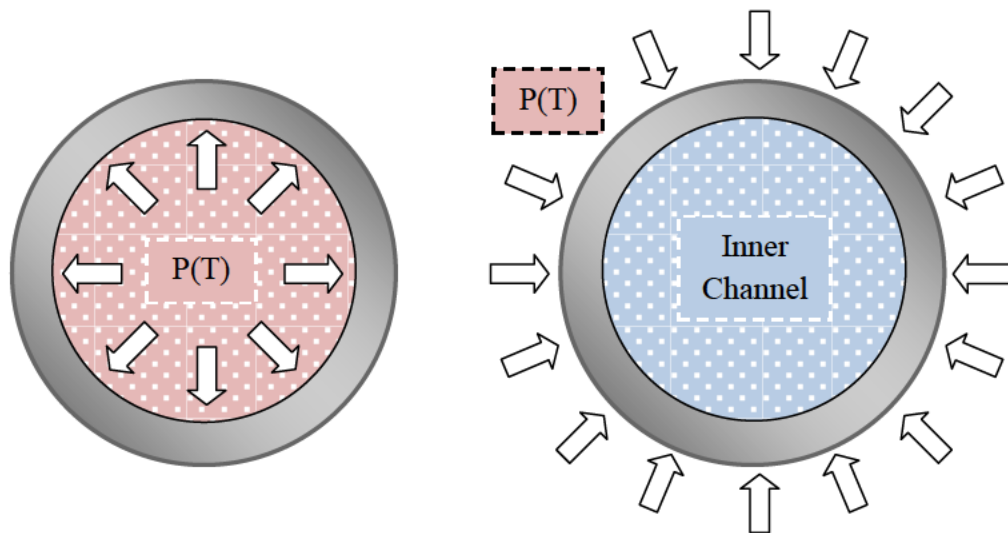


Figure 3-8: Sketch of pressure imposed on (a) outer clad and (b) inner clad

As the molybdenum element design does not contain the UZrH fuel present in the OSTR fuel rods, it is assumed that pressure will not increase via dissociation of

hydrogen in appreciable quantities from the solid fuel at elevated temperatures [55]. The stress caused by an internal pressure pushing “out” on a thin-walled cylindrical vessel may be approximated as [56]

$$\sigma_{\theta} = \left(\frac{Pb}{t} \right), \quad (3-2)$$

note that σ_{θ} is the stress imposed upon the cylinder (Pa), P is the internal membrane pressure on the solid body (Pa), b is the radius (m), and t is the thickness of the cylinder (m). Note that equation (3-2) is appropriate for estimating the stress level of a cylinder when the radius is more than four times the wall thickness. By assuming that the annular cladding may be modeled as one thin-walled cylinder of radius b_{outer} subtracted by another thin-walled cylinder of radius b_{inner} , where $b_{inner} < b_{outer}$, where both cylinder walls have the same thickness and internal pressure, the annular stress may be written as [56]

$$\sigma_{\theta} = \left(\frac{Pb_{outer}}{t} \right) - \left(\frac{Pb_{inner}}{t} \right) = \left(\frac{P(b_{outer} - b_{inner})}{t} \right). \quad (3-3)$$

From Table 3-3, wall thickness is approximately 3.2 mm, b_{outer} is assumed to be 17.1 mm and b_{inner} is represented by 14.9 mm. The elastic limit yield strength of an aluminum material may be conservatively estimated to be at approximately 35 MPa [57]. Therefore, if the internal pressure imposes a stress equal to or greater than 35 MPa the element may fail due to outer clad failure.

The internal gas also imposes a stress upon the inner aluminum cladding by pushing “in” on the clad. If that stress reaches a critical level, the inner cladding may fail via buckling. The critical pressure, P_{crit} , which will cause a thin-walled tube to buckle from an external pressure may be expressed as [56]

$$P_{crit} = \left(\frac{3EI}{R^3} \right), \quad (3-4)$$

note that E is the Young’s Modulus of the cladding (Pa), I is the second moment of area of the cladding (m^4), and R is the centerline radius of the tube (m). The centerline radius of the inner cladding may be seen from Figure 3-4 to be 14.11 mm. The

Young's Modulus of aluminum 6061-T6 may be conservatively estimated as 69 GPa [57]. The value of I for a thin-walled tube may be expressed as

$$I = \pi R^3 t, \quad (3-5)$$

which results in a value of $2.82\text{E-}8 \text{ m}^4$ for the cladding [56].

Based on the computed information provided and the relations presented in (3-3) and (3-4), the critical pressure which will cause buckling of the inner clad is 20.67 MPa and the pressure which will cause rupture of the outer clad is 2.081 GPa. Thus, the limiting pressure is assumed to be 20.67 MPa. The internal pressure levels generated within the annular clad at elevated temperatures is a result of the thermal expansion of the UO_2 fuel and of the surrounding air. Given that the volumetric expansion coefficient of an isotropic sample of UO_2 is approximately $0.00003 \text{ }^\circ\text{C}^{-1}$ at $26.85 \text{ }^\circ\text{C}$ [51] and the volumetric expansion coefficient of air is $0.003 \text{ }^\circ\text{C}^{-1}$ [52], it is assumed that the internal pressure within the cladding is the sole result of thermal expansion of the gas.

By assuming that the air behaves as an ideal gas, the limiting pressure may be written into the ideal gas law as

$$PV_{gas} = n_{gas} R_{gas} T, \quad (3-6)$$

note that V_{gas} is the total gas volume (m^3), which remains constant within the aluminum cladding at 35.17 cm^3 , n_{gas} is the number of moles of gas present (mols), which remains constant at 0.00211 mols due to a loading at room temperature with a density of 1.2 kg/m^3 [57] and an assumed molecular weight of 20 g/mol, R_{gas} is the ideal gas constant 8.314 (J/mol-C) [57], and T is the temperature of the gas ($^\circ\text{C}$).

The corresponding limiting temperature for inner clad failure is approximately $41,300^\circ\text{C}$ as illustrated in Figure 3-9. This temperature is significantly higher than those highlighted in Table 3-5. As a result, it may be assumed that molybdenum element internal pressure is not a cause of concern with regards to cladding failure due to internal overpressure.

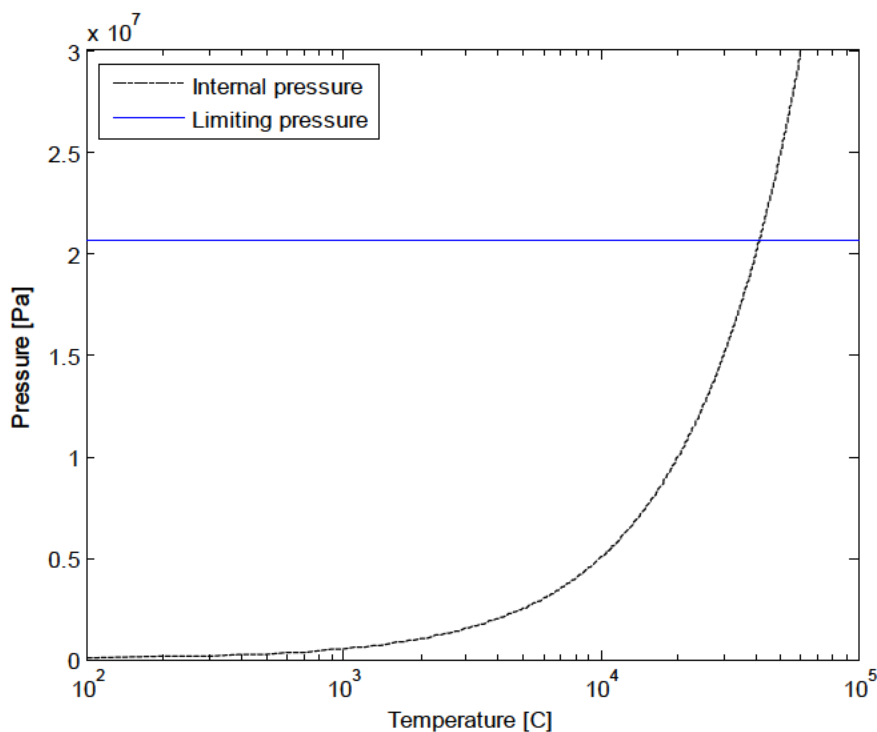


Figure 3-9: Molybdenum element internal pressure as a function of temperature

4 RELAP5-3D MODEL

4.1 Model Summary and Justification

The model constructed for this analysis simulates the placement of a molybdenum element within the “hottest” channel. The hottest channel refers to the location within the core that has the smallest flow area in combination with the element producing the largest power [47]. The decision to perform this analysis with a single channel model approach was based upon previous RELAP5-3D models of the OSTR of both one, two, and eight channel constructions [8,32]. The conclusions reached from those models showed that calculated CHF values did not deviate more than ~1.0% from one channel models to two and eight channel models, and that one channel models produced the most conservative CHF results due to the lack of cross-flow between neighboring coolant channels [8,32]. A single channel model was chosen in order to

acquire the most conservative set of results to ensure safe molybdenum element deployment within a conservative margin of safety.

4.2 Model Description

The RELAP5-3D model constructed for this study is composed of six hydrodynamic volumes, two junction components, two branch components, and four heat structures (HS). The hydrodynamic volumes and junction components allow for continuous fluid flow throughout the model. The hydrodynamic volumes, depicted in Figure 4-1, include the coolant source, the cold leg, the horizontal connector, the inner channel, the outer channel, the inner connector, the outer connector, and the coolant sink.

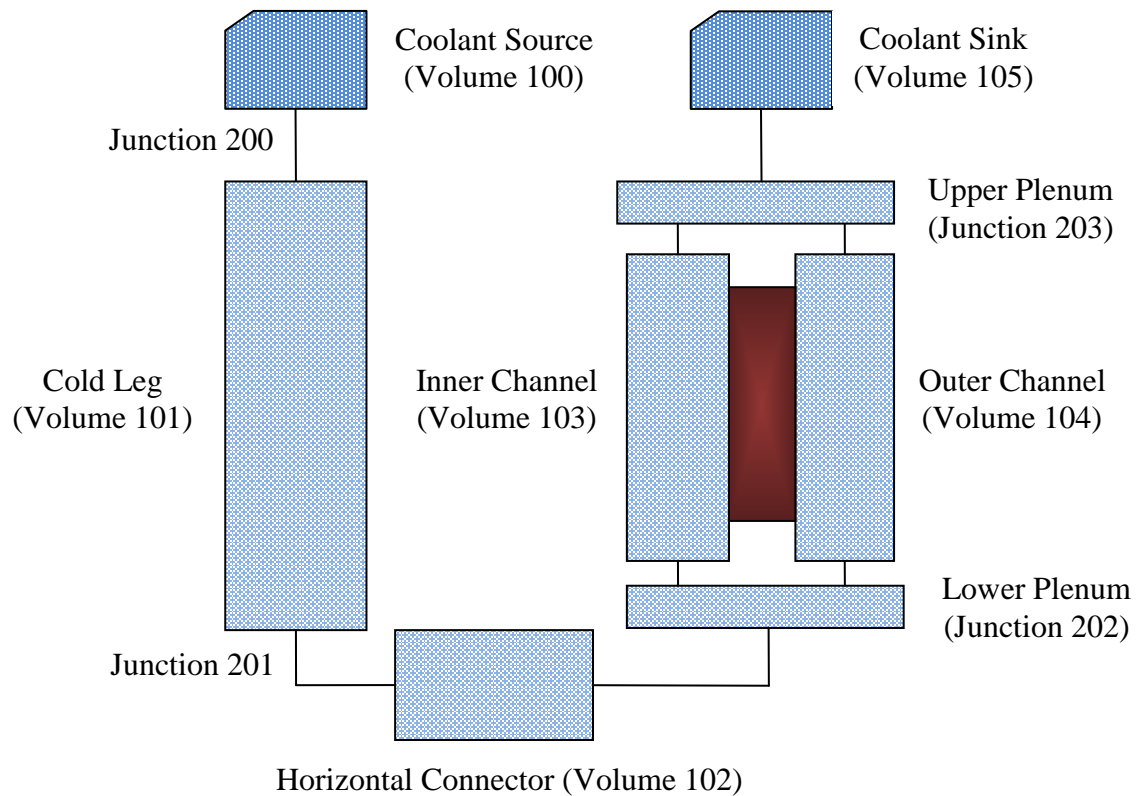


Figure 4-1: Sketch of RELAP5-3D model

Equation Section (Next)

Volumes 100 and 105, the coolant source and coolant sink, are modeled as time-dependent volumes with a prescribed fluid temperature, pressure, and fluid quality (set to values consistent with the technical specifications of the OSTR) which remain

constant throughout simulated scenarios. These volumes exist to provide volume-related boundary conditions for the model [58], which allows for fluid to flow in and out of the system. These volumes contain no form losses.

Volume 101, the cold leg, exists to provide an appropriate water column that allows for natural circulation flow to occur when a heat source is introduced via the heat structure which models the molybdenum element's fuel material. This volume has a height equivalent to that of the OSTR core from lower grid plate to upper grid plate, and contains no form losses.

Volume 102, the horizontal connector, exists to provide a path for fluid flow from the cold leg to the lower plenum. This volume contains no form losses.

Volumes 103 and 104, the inner channel and outer channel, represent the geometry of the molybdenum element's inner and outer flow areas, respectively. The flow area of the outer channel, A_{outer} (m²), may be calculated in accordance with the element's outer diameter as [8]:

$$A_{outer} = \left(\frac{3^{1/2}}{2} \right) Pi^2 - \frac{\pi D_{outer}^2}{4} \quad (4-1)$$

note that Pi is the core pitch (the distance between the centerline of adjacent elements within the core region, m). The flow area of the inner channel, A_{inner} (m²), may be calculated from the element's inner diameter as [48]:

$$A_{inner} = \frac{\pi D_{inner}^2}{4} \quad (4-2)$$

These volumes are sub-divided into 31 sub-volumes, which may each experience differences in conditions such as temperature, pressure, quality, and flow rate. The first and last sub-volume of these volumes act as the channel inlet and outlet, respectively and contain form loss values calculated to best represent form loss values present in a physical molybdenum element [47]. As illustrated in Figure 4-2, sub-volumes 2 through 4 are adjacent to the lower washer, sub-volumes 5 through 24 are

adjacent to the fuel material, sub-volumes 25 through 27 are adjacent to the upper washer, and sub-volumes 28 through 30 are adjacent to the helium region.

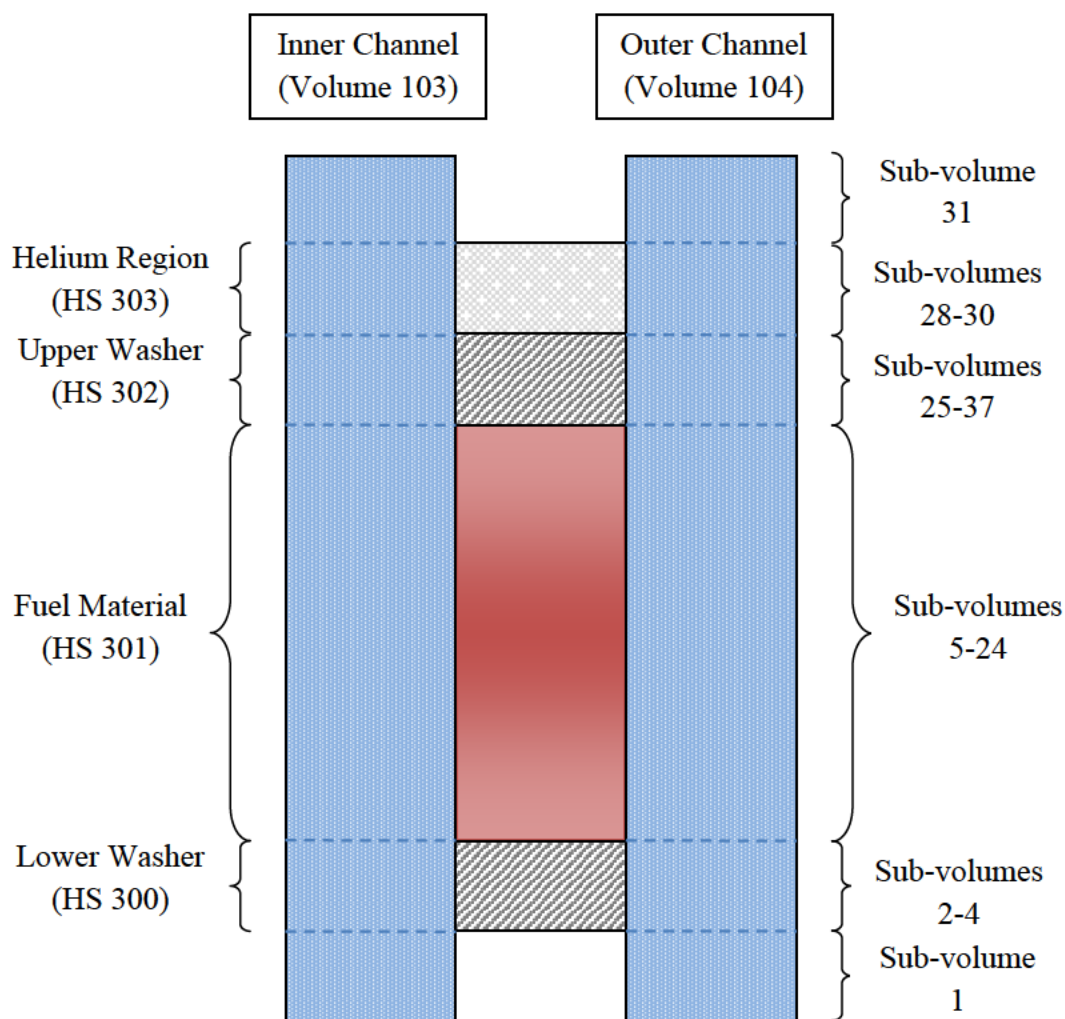


Figure 4-2: RELAP5-3D inner and outer channel sub-volumes

Junctions 200 and 201 provide a path for fluid to flow through the model and connect a single hydrodynamic volume to another. Junction 200 connects the coolant source to the cold leg. Junction 201 connects the cold leg to the horizontal connector. The flow area of these junctions is set to the minimum flow area of two hydrodynamic volumes to which they are connected. These components are nonphysical and contain no explicit form loss values.

Branch 201, denoted as the “lower plenum,” connects the horizontal connector to the inner channel and outer channel. Branch 202, denoted as the “upper plenum,” connects the inner channel and outer channel to the coolant sink. The flow area of the junctions is set to the maximum flow area of the three hydrodynamic volumes to which they are connected. The flow area of each individual single-junction connection within the branch is set to the flow area of the hydrodynamic volume connected to the branch (i.e. the flow area between the outer channel and the lower plenum is equivalent to the flow area of the outer channel). These components contain no explicit form loss values.

Heat structures 300 and 302, the lower washer and upper washer, represent the lower and upper aluminum regions which rest below and above the fuel material within the molybdenum element. The lower washer is in contact with sub-volumes 2 through 4 of the inner channel and outer channel, and the upper washer is in contact with sub-volumes 25 through 27 of the inner channel and outer channel. These structures are coded with three axial and radial sub-volumes, and are fully composed of aluminum throughout. The lower washer and upper washer do not contain any source terms.

Heat Structure 301, the fuel material, represents the fueled length of a molybdenum element. The fuel material is in contact with sub-volumes 4 through 24 of the inner channel and outer channel. This structure contains 20 axial sub-volumes and 22 radial sub-volumes, with a uranium-dioxide composition within radial sub-volumes 2 through 21 and an aluminum composition within radial sub-volumes 1 and 22. The fuel material contains 20 axial and radial source terms. These source terms represent power profiles generated from MCNP5 completed as part of the OSU Molybdenum Project [48]. These source terms, discussed in further detail in Chapter 4.4, allow for heat to be deposited into the model’s structure.

Heat Structure 303, the helium region, represents the gas-filled section above the upper washer within the molybdenum element’s hollow annulus. The gas region is in contact with sub-volumes 28-30 of the inner channel and outer channel. This structure

has three axial and radial sub-volumes, and is composed of helium gas throughout. Helium is chosen as the fill gas in the study described herein as it serves as a conservative substitution for air due to its decreased thermal conductivity and volumetric heat capacity. The gas region contains no source terms.

4.3 Calculated Form Losses

As a lumped-parameter code, RELAP5-3D requires user inputs to specify particular model values, including form loss coefficients in both the “forward” and “reverse” directions [7,8]. Form loss coefficients refer to the group of loss coefficients caused when fluid flows encounter conditions such as sudden expansions, sudden contractions, bends or elbows, fittings, etc [53]. These loss coefficients have an effect on the flow which may be represented as [53]:

$$\sum K = \Delta P \left(\frac{1}{2} \rho v^2 \right)^{-1} \quad (4-3)$$

where K is a loss coefficient in the piping system, ΔP is the change in pressure across the piping system (Pa), ρ is the density of the fluid (kg/m^3), and v is the velocity of the fluid flow (m/s) [53]. Large loss coefficients will result in large pressure drops across sections of pipe, and thus provide a retarding force against the primary flow direction. Thus, the larger the loss coefficient, the more flow will be hindered, causing a reduction in mass flow rates and thus a decrease in the cooling capability of a convection-cooled system.

Previous studies have calculated form loss values for OSTR fuel rod elements in the B-ring hot channel [59]. These values were calculated by considering the path of coolant from the reactor pool through the lower grid plate, around the fuel rod’s fins, around the fuel rod’s “lower nub” (lower end fitting), around the fuel rod’s length, through the upper grid plate, and around the “upper nub” (upper end fitting) back to the reactor pool [59]. This fluid path leads flow through a series of sudden expansions and sudden contractions, which correspond with form loss terms based upon the

magnitude of the sudden change in area [59]. A sketch of vertical fluid flows through sudden expansions and contractions is illustrated in Figure 4-3.

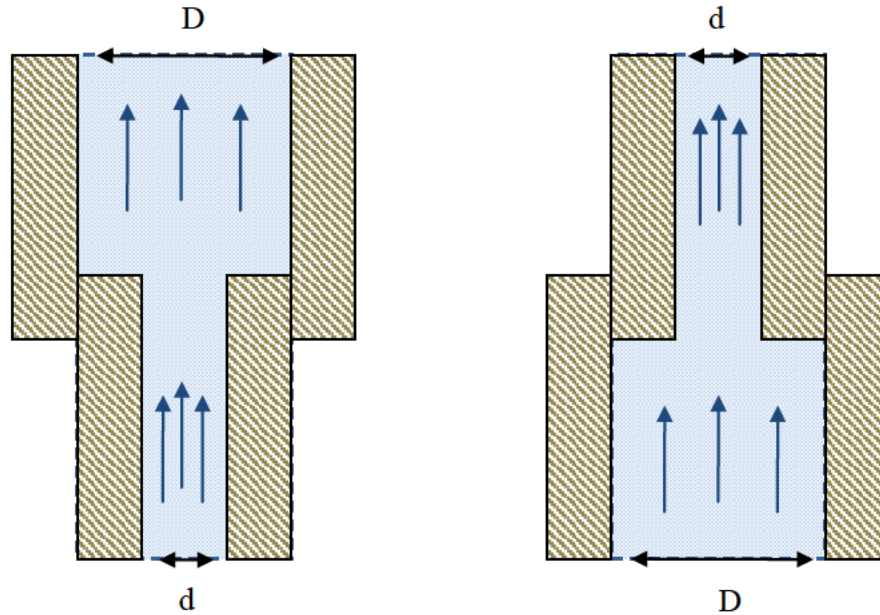


Figure 4-3: Sketch of flow sudden expansion (left) and sudden contraction (right)

The form losses for a sudden expansion or a sudden contraction may be determined as [53,59]

$$K_{\text{Expansion}} = \left(1 - \frac{d^2}{D^2}\right)^2 \quad (4-4)$$

$$K_{\text{Contraction}} = 0.42 \left(1 - \frac{d^2}{D^2}\right) \quad (4-5)$$

note that $K_{\text{Expansion}}$ is the form loss due to a sudden expansion, $K_{\text{Contraction}}$ is the form loss due to a sudden contraction, d is the smaller flow diameter (m), and D is the larger flow diameter (m). As the RELAP5-3D model does not include the level of detail present in a physical system, local form loss values are converted to effective form loss values by referencing channel flow area as [59]

$$K_{\text{Effective}} = K_{\text{Local}} \left(\frac{A_{\text{Chanel}}}{A_{\text{Local}}}\right)^2 \quad (4-6)$$

note that $K_{Effective}$ is the effective form loss value, K_{Local} is the local sudden expansion or sudden contraction form loss value, $A_{Channel}$ is the area of the flow channel (m^2), and A_{Local} is the local area (m^2). Local and effective form losses are calculated separately for both the inlet and outlet of the inner channel and outer channel. As in previous studies using RELAP5 to model the OSTR, inlet form loss values are only coded in the first sub-volume of a channel and outlet form loss values are only coded in the terminal sub-volume of a channel [8,32,59]. Form loss terms are also only coded in the forward direction. Surface roughness terms are included in both the inner and outer channel at each sub-volume, which provide a small contribution to overall flow hindrance.

The inlet and outlet form loss terms for the inner channel and outer channel are dependent upon the flow path through each channel. Each flow path begins with coolant flowing from the reactor pool through the lower grid plate openings and around the molybdenum element's lower nub. At this point, the flow separates as illustrated in Figure 4-4.

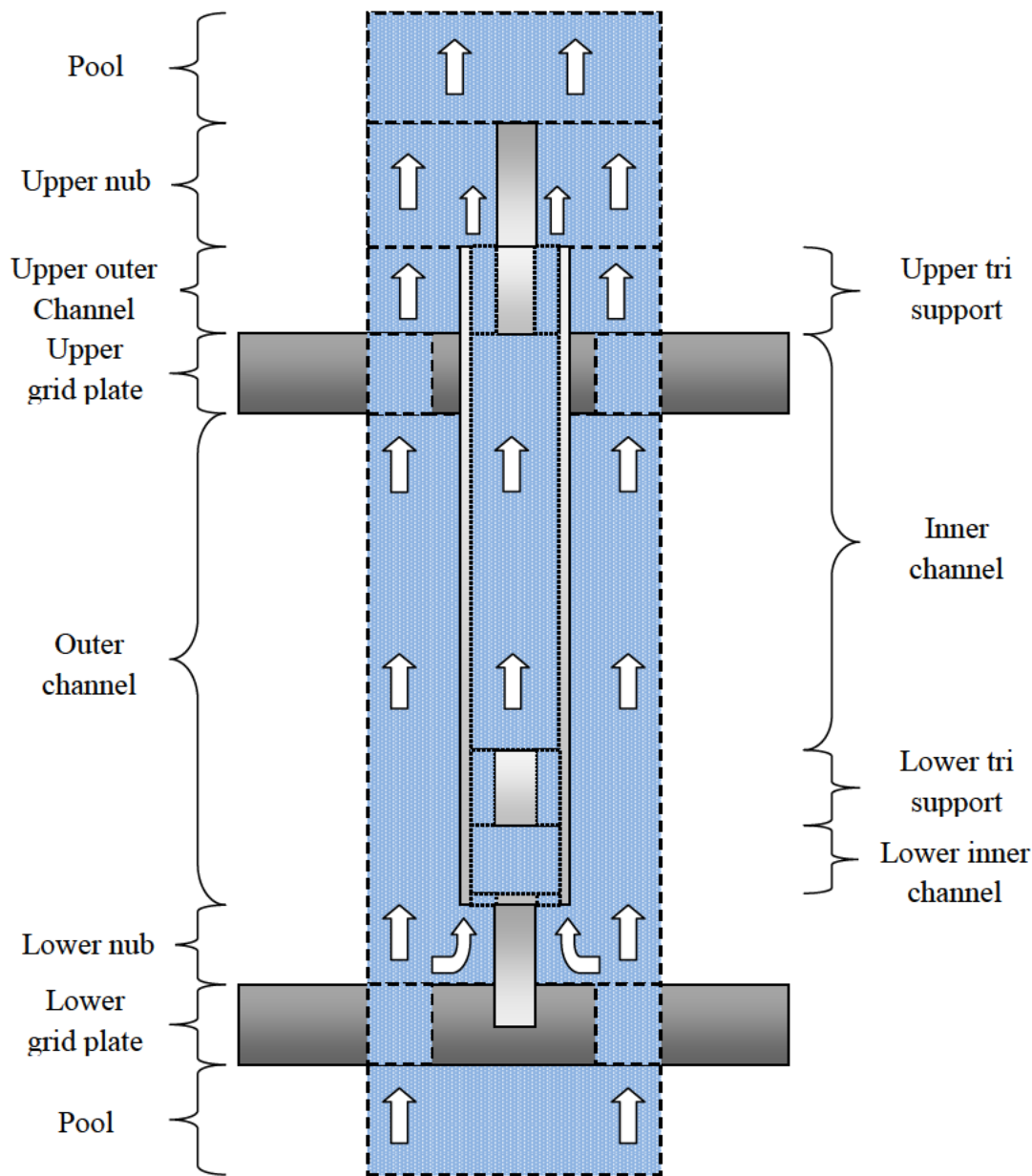


Figure 4-4: Sketch of flow through outer and inner channels

The outer channel flow path continues through the outer channel, through the upper grid plate, around the upper nub, and terminates in the reactor pool. The inner flow path continues into the lower inner channel, through the lower tri support, through the inner channel, through the upper tri support, around the upper nub, and terminates in the reactor pool. Flow areas for each volume within both flow paths are calculated using OSTR core and molybdenum element geometry. Calculated form loss values for

the molybdenum element are given in Table 4-1 with the form loss values of an OSTR fuel rod to serve as a comparison [59].

Table 4-1: Molybdenum element and fuel rod calculated form loss values

| Geometry | Sum of local form losses | Sum of effective form losses |
|-----------------------|--------------------------|------------------------------|
| Outer channel, inlet | 1.215 | 1.115 |
| Outer channel, outlet | 0.983 | 0.862 |
| Inner channel, inlet | 1.797 | 7.188 |
| Inner channel, outlet | 1.112 | 6.970 |
| OSTR fuel rod, inlet | 2.387 | 2.253 |
| OSTR fuel rod, outlet | 1.067 | 0.633 |

The exclusion of fins from the molybdenum element has the effect of decreasing the outer channel inlet form loss term while increasing the outer channel outlet form loss term. The inclusion of tri supports located within the inner flow channel of the molybdenum element has the effect of providing large inner channel inlet and outlet form loss terms when compared with the outer channel.

4.4 Fuel Core Source Profiles

Element power levels vary based on grid position within the OSTR as illustrated in Figure 4-5. Because of this power distribution, the total power generated by the molybdenum element's fuel material is dependent upon the element's placement within the core. The total power level input into the RELAP5-3D model was chosen as the highest value which represents placement in the G-32, G-33, or G-34 core position at core power of 1.1 MW_{th} [32]. These positions represent the three potential deployment locations where OSU intends to place a molybdenum element. The highest power level of a deployed molybdenum element occurs in the G-34 position, at a calculated 11.55 kW [48].

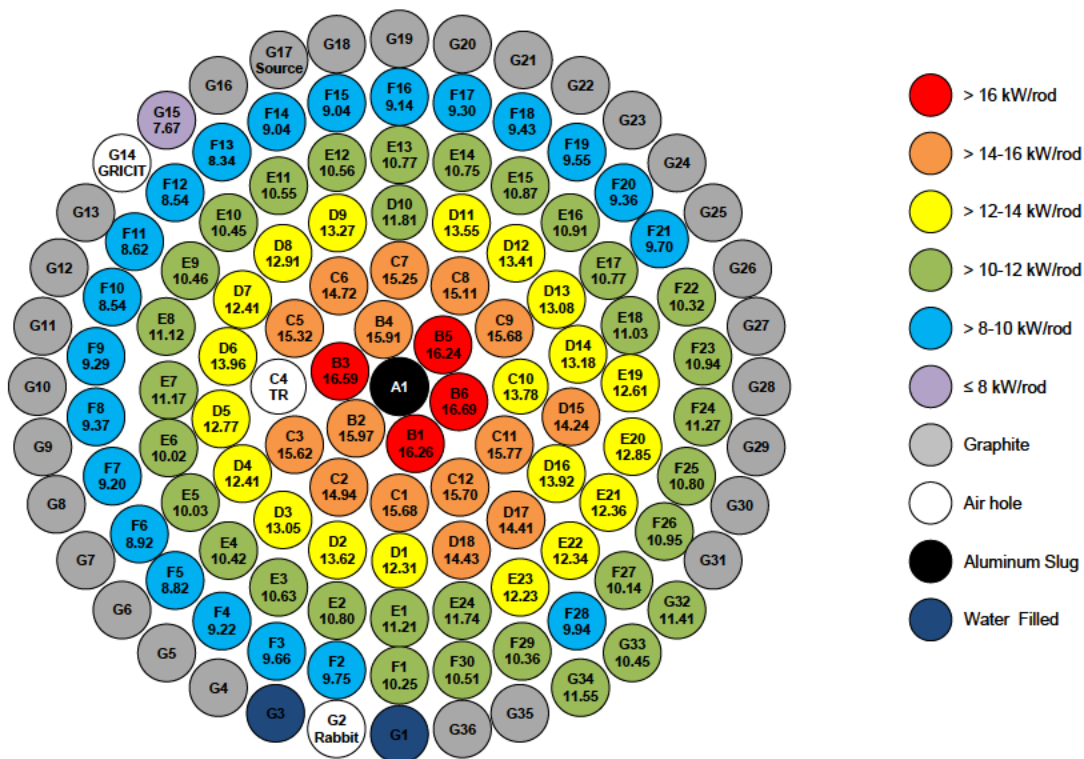


Figure 4-5: MCNP5 calculated OSTR element power at 1.1 MW [48]

The power distribution of a molybdenum element may be expressed as two non-uniform profiles in the axial and radial directions, as illustrated in Figure 4-6 and Figure 4-7. The 20 discrete power fraction data points align with the respective twenty discrete axial and radial nodes in HS 302. MCNP5 was used to produce these power profiles as part of the OSU Molybdenum Production Project in the same manner as those produced for OSTR fuel rods in the 2008 core conversion [8,32,48].

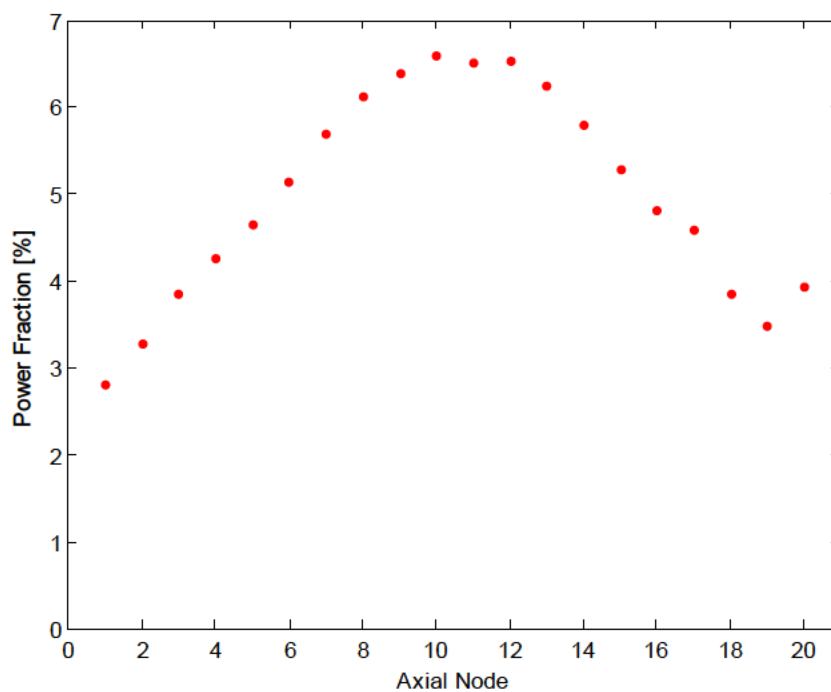


Figure 4-6: Axial power distribution of molybdenum element

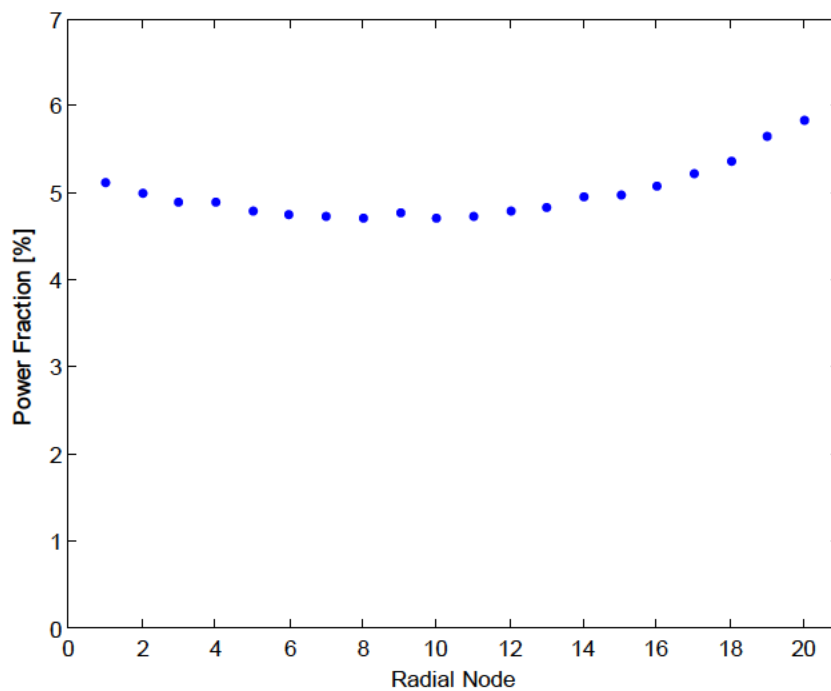


Figure 4-7: Radial power distribution of molybdenum element

4.5 Material Models and Description

Each heat structure modeled by RELAP5-3D must be given a composition [60]. To accurately model the molybdenum element, aluminum was required for the upper washer and lower washers, 200 μ m UO₂ spheres in fill gas were required for the fuel material, and helium gas was needed for the helium region. As RELAP5-3D does not contain data sets for some of these materials, user input data and functions were used. The following sections detail the required thermal properties input for each material composition at specific temperatures.

4.5.1 RELAP5-3D Model Thermal Conductivity Data

The thermal conductivities of aluminum and helium were sourced from existing literature [52]. As a source of thermal conductivity values for 0.676 packing factor sphere-pac UO₂ in helium gas was not available, the thermal conductivity of the UO₂ fuel was calculated through two equations presented in NUREG/CR-7024 [61]. The equation for the thermal conductivity of 95% theoretical density UO₂ fuel pellets as shown below [61]:

$$k_{95} = \frac{1}{A + a \cdot gad + BT + f(Bu) + (1 - 0.9e^{(-0.04Bu)})g(Bu)h(T)} + \frac{E}{T^2} e^{\left(\frac{F}{T}\right)} \quad (4-7)$$

note that k_{95} is the thermal conductivity for a theoretical fuel of 95% density (W/m- $^{\circ}$ C), T is the temperature ($^{\circ}$ C), Bu is the burn-up (GWd/MTU), $f(Bu)$ is the effect of fission products in a crystal matrix as 0.00187-Bu, $g(Bu)$ is the effect of radiation defects as 0.038* $Bu^{0.28}$, Q is a temperature dependence parameter as 6106.85 ($^{\circ}$ C), A is a constant as 0.0452 (m- $^{\circ}$ C/W), a represents a constant as 1.1599, gad represents the weight fraction of gadolinia present (% mass), B represents a constant as 2.46E-4 (m- $^{\circ}$ C/W/ $^{\circ}$ C), E represents a constant as 3.5E9 (W- $^{\circ}$ C/m), and F is a constant as 16087.85 (K).

Given that the UO_2 within the sphere-pac fuel has a total density of one, no loaded gadolinia, and no burn-up, a simplified version of the above equation may be written for non-95% theoretically dense fuels as shown below [61]:

$$k_d = 1.0789 \cdot k_{95} \left(\frac{d}{1 + 0.5(1 - d)} \right) \quad (4-8)$$

note that k_d is the thermal conductivity ($\text{W/m}^\circ\text{C}$) for a theoretically dense fuel of some density d as a fraction of total density (% density). The effective thermal conductivity of the molybdenum element fuel material was calculated by mass averaging the fuel's helium and UO_2 components with an assumed packing factor of 0.676 by:

$$k_{\text{eff}} = \frac{VF \cdot V_T \cdot \rho_{\text{UO}_2} \cdot k_d(T) + (1 - VF) \cdot V_T \cdot \rho_{\text{He}}(T) \cdot k_{\text{He}}(T)}{VF \cdot V_T \cdot \rho_{\text{UO}_2} + (1 - VF) \cdot V_T \cdot \rho_{\text{He}}(T)} \quad (4-9)$$

note that VF is the volume fraction of UO_2 , V_T is the total fuel volume, ρ_{UO_2} is the density of UO_2 (kg/m^3), k_d is described in (4-8), ρ_{He} is the density of helium (kg/m^3), and k_{He} is the thermal conductivity of helium. Figure 4-8 and Figure 4-9 detail the values of thermal conductivity for the aluminum, helium, UO_2 , and sphere-pac fuel compositions within reasonable temperature limits.

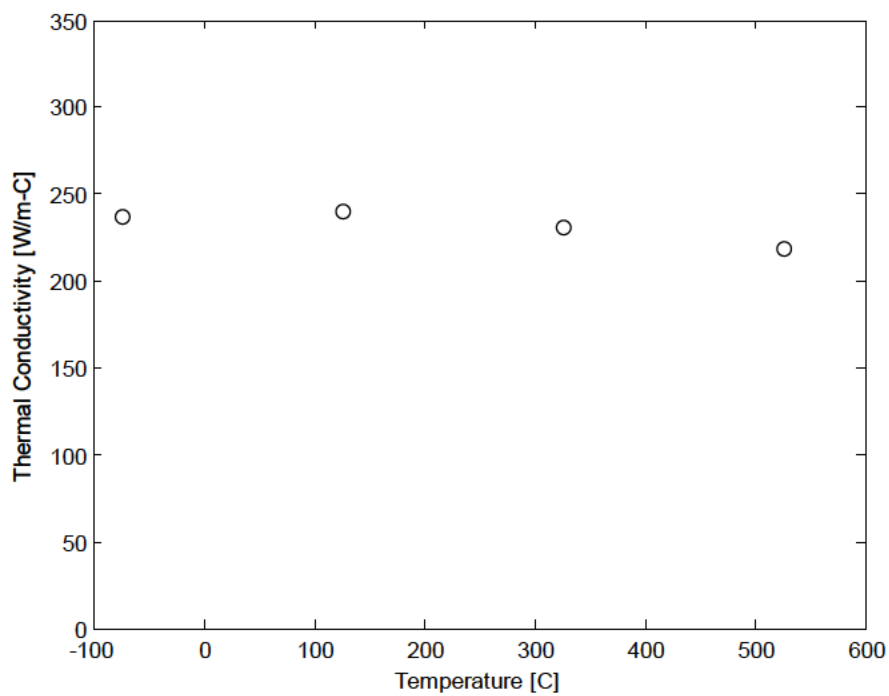


Figure 4-8: Thermal conductivity of aluminum

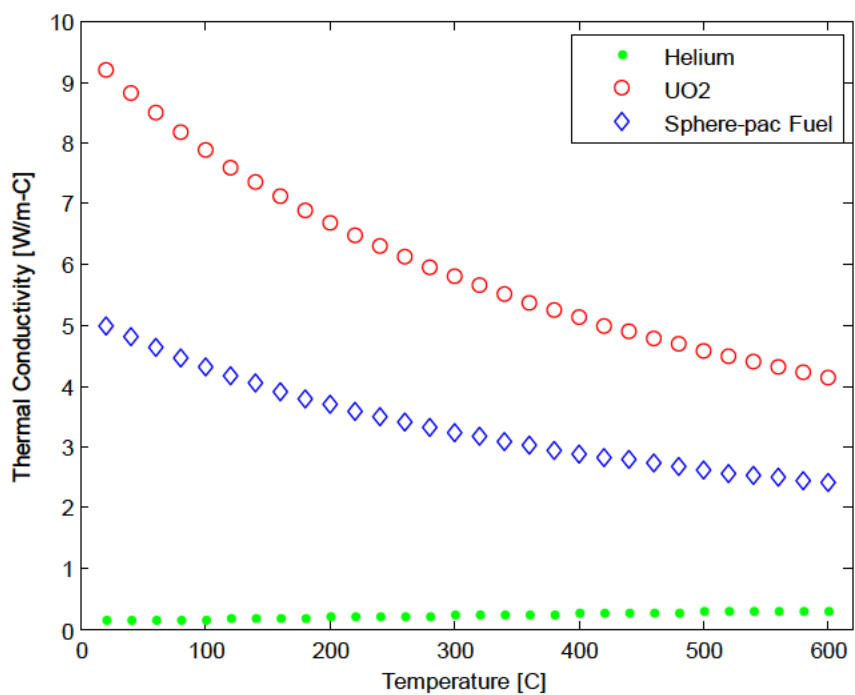


Figure 4-9: Thermal conductivity of fueled region materials

4.5.2 RELAP5-3D Model Volumetric Heat Capacity Data

The values required for the composition volumetric heat capacities were sourced from existing literature in the case of helium, solid UO₂ fuel, and aluminum [51,52]. The volumetric heat capacity of the sphere-pac fuel was calculated via mass averaging values for solid UO₂ and helium densities and heat capacities in the case of the sphere-pac fuel.

A mass fraction approach between the solid UO₂ spheres and the surrounding helium gas was used to calculate the specific heat capacity of the sphere-pac fuel as:

$$C_p = \frac{VF \cdot V_T \cdot \rho_{UO_2} \cdot \rho C_{p,UO_2}(T) + (1-VF) \cdot V_T \cdot \rho_{He}(T) \cdot \rho C_{p,He}(T)}{VF \cdot V_T \cdot \rho_{UO_2} + (1-VF) \cdot V_T \cdot \rho_{He}(T)} \quad (4-10)$$

note that C_p is the specific heat capacity of the sphere-pac fuel (J/m³*K), VF is the volume fraction of the fuel as 0.676, V_T is the total fuel volume (m³), T is the temperature (K), ρ_{UO_2} is the density of UO₂ (kg/m³), C_{p,UO_2} is the specific heat capacity of UO₂ (J/kg*K), ρ_{He} is the density of helium (kg/m³), and $C_{p,He}$ is the specific heat capacity of helium (J/kg*K). The volumetric heat capacities for aluminum, helium, UO₂, and sphere-pac fuel compositions within reasonable temperature limits are presented in Figure 4-10, Figure 4-11, and Figure 4-12.

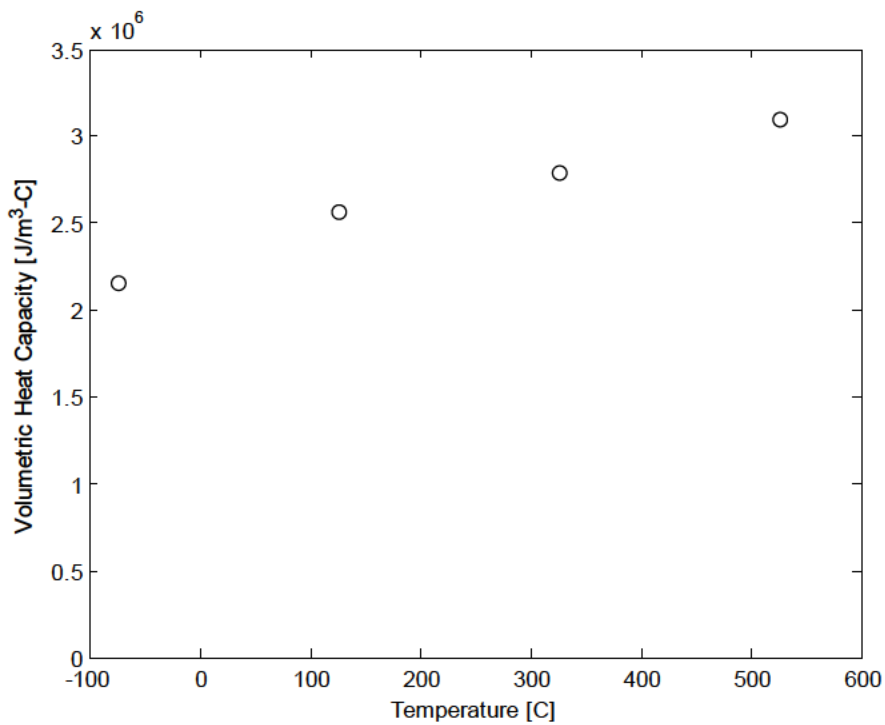


Figure 4-10: Volumetric heat capacity of aluminum

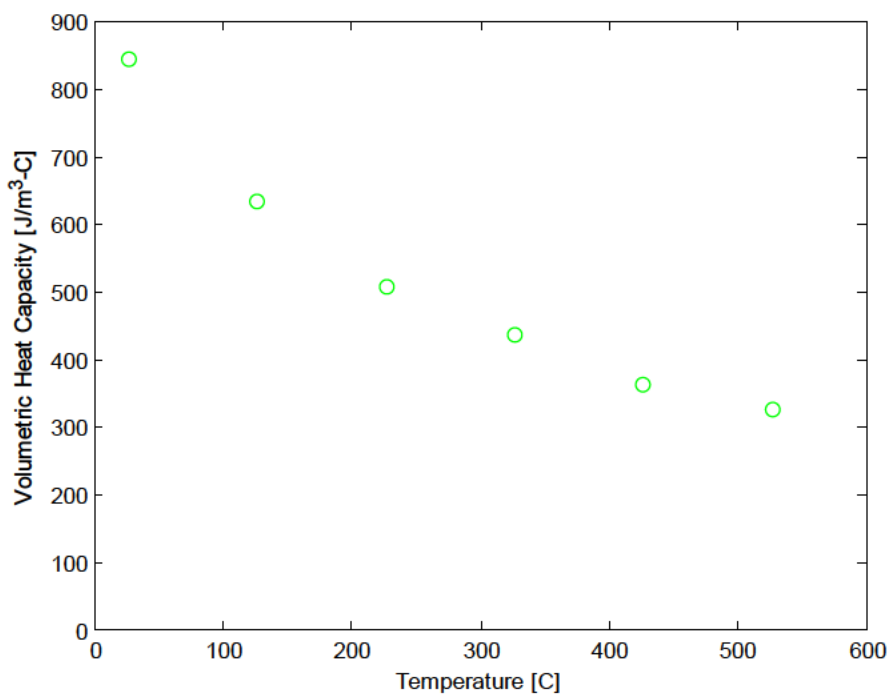


Figure 4-11: Volumetric heat capacity of helium

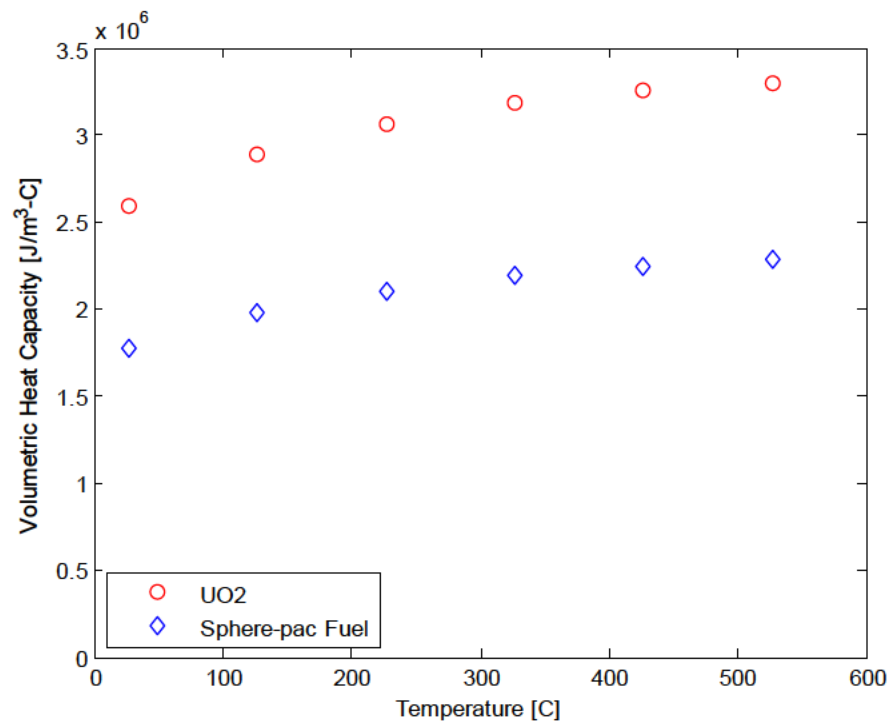


Figure 4-12: Volumetric Heat Capacity of UO₂ vs. Temperature

5 RESULTS AND DISCUSSION

5.1 Steady-State Results

5.1.1 Thermal Hydraulic Characteristics at Full Power

Recall from Section 1.2 that the most important parameters dictating the safety of a deployed molybdenum element are (1) maximum fuel temperature, (2) maximum cladding temperature, and (3) critical heat flux (CHF) ratios during steady-state operation. As CHF ratios are dependent upon flow rate, the mass flow rates and velocities within the inner channel and outer channel flow are of significant importance. Each of these values is presented in the tables and figures in the following section. Table 5-1 summarizes the molybdenum element RELAP5-3D model results during steady state operating conditions within the OSTR at an integral power level of 1.1 MW_{th}.

Table 5-1: Steady-state results

| Steady-state parameter | Inner channel value | Outer channel value |
|---|---------------------|---------------------|
| Maximum fuel temperature [C] | 144.66 | |
| Maximum clad temperature [C] | 121.69 | 119.51 |
| Minimum CHF – 2006 look-up table | 10.21 | 16.43 |
| Minimum CHF – Bernath | 15.18 | 9.64 |
| Minimum CHF – Hall-Mudawar | 21.46 | 27.49 |
| Channel outlet flow rate [kg/s] | 0.0541 | 0.0702 |
| Channel outlet velocity [m/s] | 0.0995 | 0.1891 |
| Exit bulk coolant temperature [C] | 71.63 | 72.53 |
| Exit bulk coolant pressure [kPa] | 147.35 | 147.33 |
| Maximum wall heat flux [kW/m ²] | 166.53 | 143.48 |

The predicted temperature of each heat structure sub-volume within the fuel material is dependent upon two key parameters: the internal source values in and around that sub-volume and the cooling effectiveness of the inner channel and outer channel at the axial location of that sub-volume. Predicted temperatures for each sub-volume within the fuel material heat structure are presented in Figure 5-1 and Figure 5-2. The axial and radial “hot band” temperatures are presented in Figure 5-3, and Figure 5-4.

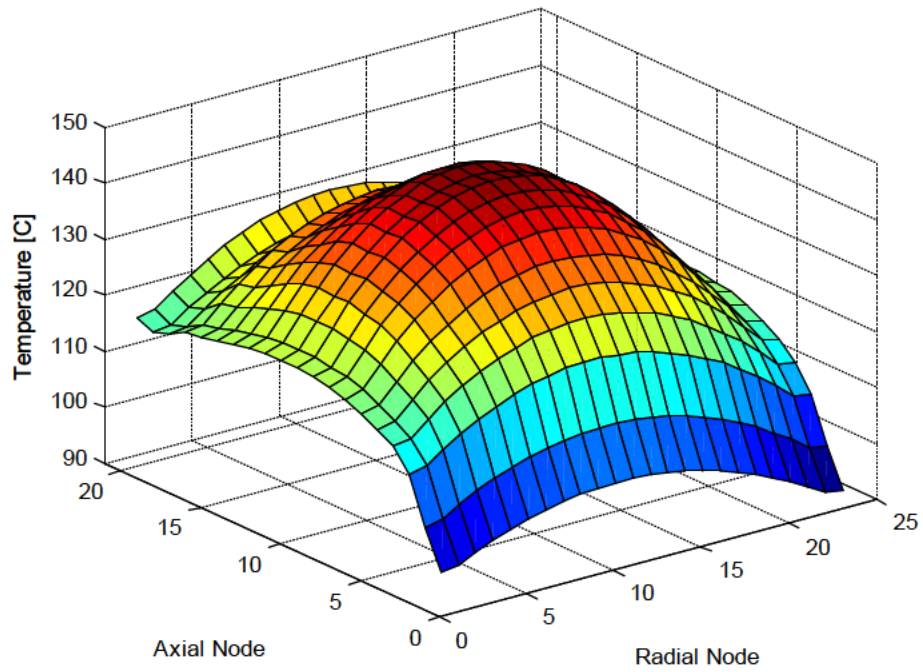


Figure 5-1: Steady state - fuel temperature

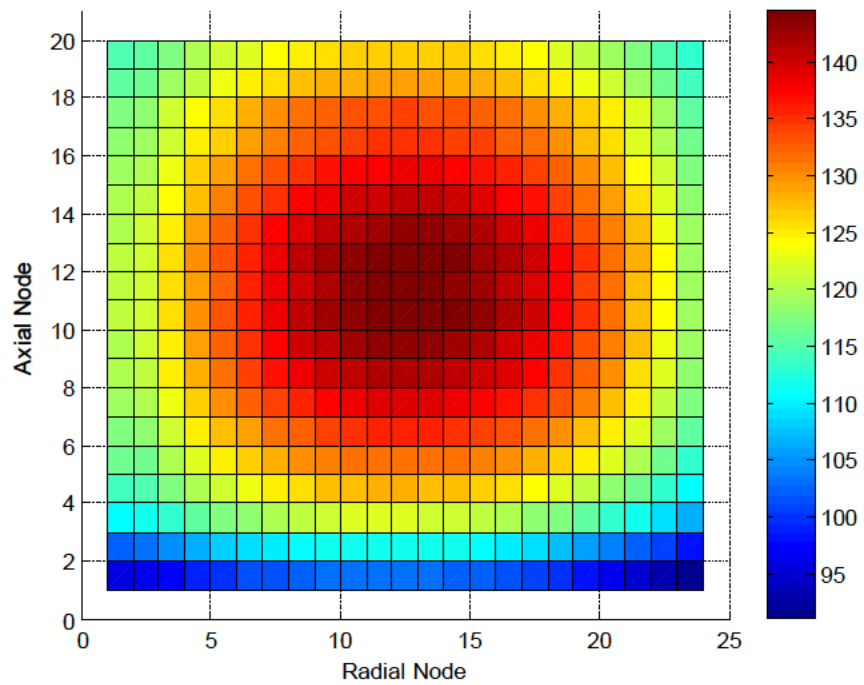


Figure 5-2: Steady state - fuel temperature

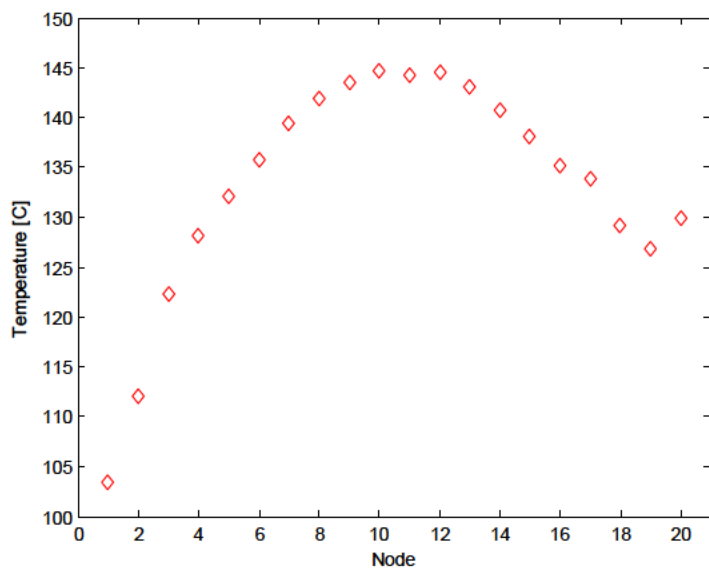


Figure 5-3: Steady state - axial hot band

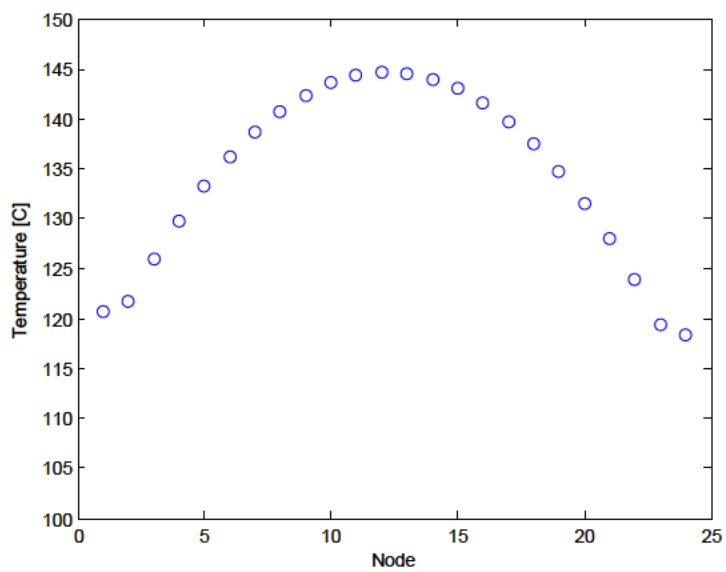


Figure 5-4: Steady state - radial hot band

Predicted maximum fuel temperatures did not exceed 145 °C. This value is well below the melting temperature of UO_2 referred to in Section 3.4 as 2856 ± 30 °C.

Furthermore, the predicted maximum fuel temperature is well below the OSTR technical specification limit of 1,150 °C [32].

Predicted maximum clad temperatures did not exceed 122 °C. This value is well below the melting temperature of aluminum referred to in Section 3.4 as 660 °C.

The predicted fuel material temperature profile presented in Figure 5-1 and Figure 5-2 indicates that maximum fuel temperatures develop within sub-volumes at a location near the heat structure's radial centerline and slightly above its axial centerline. The development of a fuel "hot spot" at this location indicates higher than nominal levels of internal heat generation within the local sub-volumes. This hot spot location is congruent with the molybdenum element source profiles presented in Section 4.4

Regions of maximum cladding temperatures develop within sub-volumes at a location adjacent to the inner channel and slightly above the heat structure's axial centerline. The highest clad temperatures, which appear in-line with the highest fuel temperatures, indicate locations where elevated conductive heat transfer occurs from the fuel material centerline.

The cooling effectiveness provided to the molybdenum element clad sub-volumes is dependent upon the coolant properties in the inner channel and outer channel, respectively, at each hydrodynamic sub-volume. The coolant temperature and velocity profiles, presented in Figure 5-5 and Figure 5-6, respectively, display the coolant characteristics within the inner channel and the outer channel along the axial flow length.

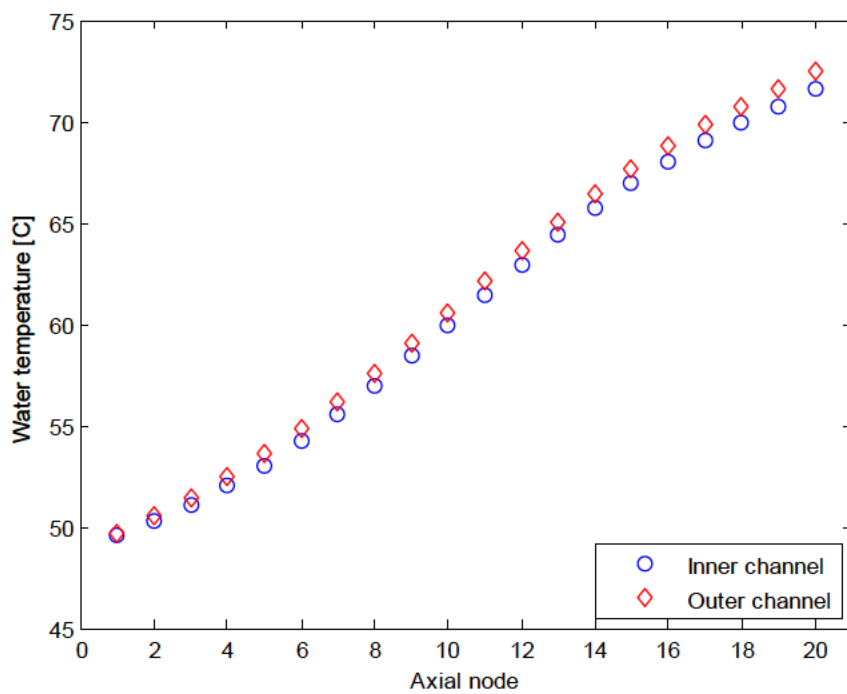


Figure 5-5: Steady state - channel coolant temperature

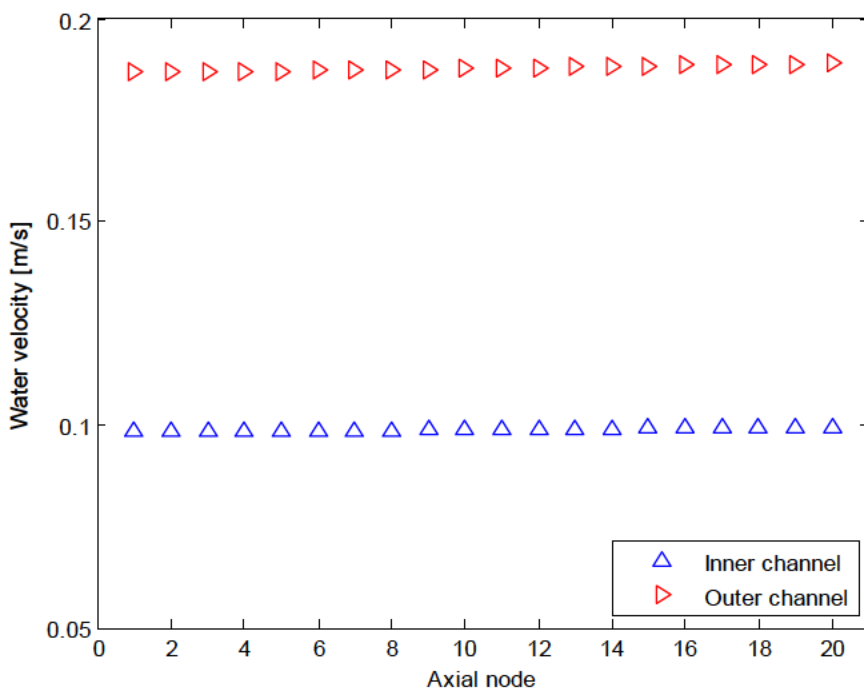


Figure 5-6: Steady state - channel coolant velocity

Predicted coolant temperatures did not exceed 72 °C in the inner channel or 73 °C in the outer channel. Coolant temperatures in the outer channel rose to values slightly higher than those in the inner channel.

Predicted coolant velocities did not exceed 0.2 m/s in the outer channel or 0.1 m/s in the inner channel. Coolant velocity profiles indicate that only slight thermal expansion of the coolant occurred along the heated flow path. Coolant velocities in the outer channel were larger than those in the inner channel. This is primarily due to the much larger form loss values in the inner channel than in the outer channel.

The areas of highest predicted heat flux appeared within the regions of highest predicted clad temperature. Given that the coolant velocity and pressure within the inner channel and outer channel remained relatively constant, heat flux and temperature variations along the axial flow length had a large contribution on the predicted CHF profiles presented in Figure 5-7.

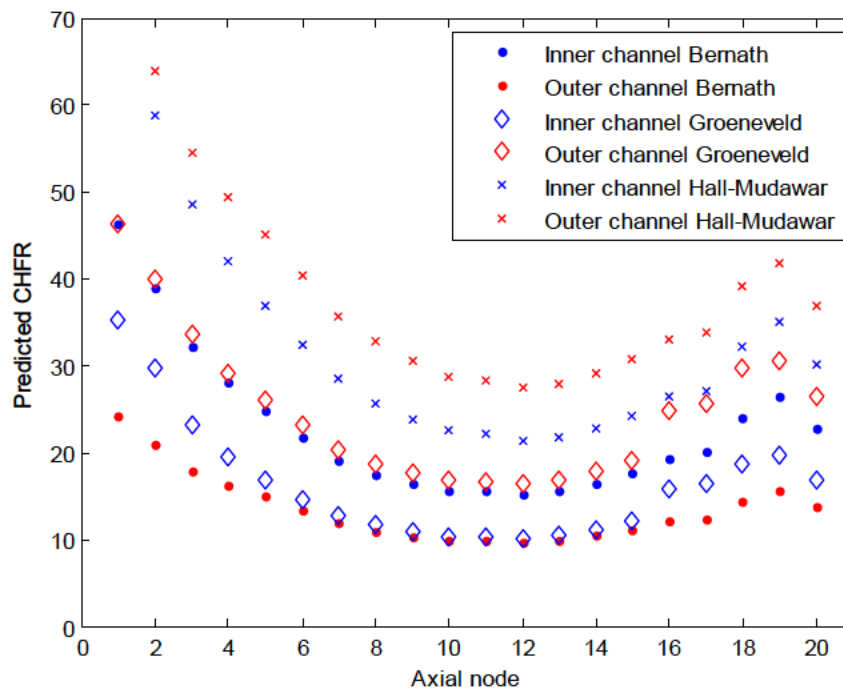


Figure 5-7: Steady-state – CHF

The most conservative predicted MCHFR was found to be 9.64 in the outer channel from the Bernath correlation. This minimum value is well within safe margins. Values from the Bernath and Groeneveld look-up table predicted more limiting CHF profiles than those predicted from the Hall-Mudawar correlation. This difference may be due to low mass fluxes ($\text{kg}/\text{m}^2\text{-s}$) in the inner and outer channel which lie below the minimum value prescribed by the Hall-Mudawar correlation.

5.1.2 Limiting Thermal Hydraulic Characteristics

An examination of the limiting thermal hydraulic parameters for molybdenum elements within the OSTR during steady state operations at varying molybdenum element power levels is included in this section. It is the intent of this study to present the profiles of limiting thermal hydraulic parameters as a function of molybdenum element power. A summary of results predicted at four discrete molybdenum element power levels during steady state operating conditions within the OSTR at an integral power level of $1.1 \text{ MW}_{\text{th}}$ is presented in Table 5-2. The results pertaining to a molybdenum element power level of 11.552 kW are presented in Table 5-1.

Table 5-2: Power variation - steady-state results

| Steady-state parameter | Molybdenum element power level | | | |
|---|--------------------------------|--------|--------|--------|
| | 5 kW | 10 kW | 15 kW | 20 kW |
| Maximum fuel temperature [$^{\circ}\text{C}$] | 110.65 | 139.58 | 155.09 | 169.42 |
| Maximum clad temperature [$^{\circ}\text{C}$] | 102.77 | 120.05 | 124.66 | 128.11 |
| MCHFR – 2006 look-up table | 26.00 | 11.87 | 7.73 | 5.65 |
| MCHFR – Bernath | 22.10 | 11.22 | 7.27 | 5.28 |
| MCHFR – Hall-Mudawar | 46.95 | 24.49 | 16.83 | 12.65 |
| Inner channel outlet flow rate [kg/s] | 0.0391 | 0.0512 | 0.0598 | 0.0666 |
| Outer channel outlet flow rate [kg/s] | 0.0520 | 0.0665 | 0.0775 | 0.0865 |
| Inner channel outlet temperature [$^{\circ}\text{C}$] | 61.73 | 69.50 | 75.85 | 81.34 |
| Outer channel outlet temperature [$^{\circ}\text{C}$] | 63.41 | 70.66 | 76.45 | 81.57 |

Table 5-2 indicates that a change in limiting thermal hydraulic parameters occurs from less limiting values to more limiting values as molybdenum element power levels increase. The largest change in limiting thermal hydraulic parameters occurs between the 5 kW and 10 kW power levels due to a doubling in molybdenum element power. Further increases in molybdenum element power indicated less pronounced changes in limiting thermal hydraulic parameters.

As presented in Figure 5-8, the rise in maximum fuel temperature was on the order of tens of °C per 5 kW increase, while the rise in maximum clad temperature was on the order of several °C per 5 kW increase beyond the 5 kW to 10 kW transition.

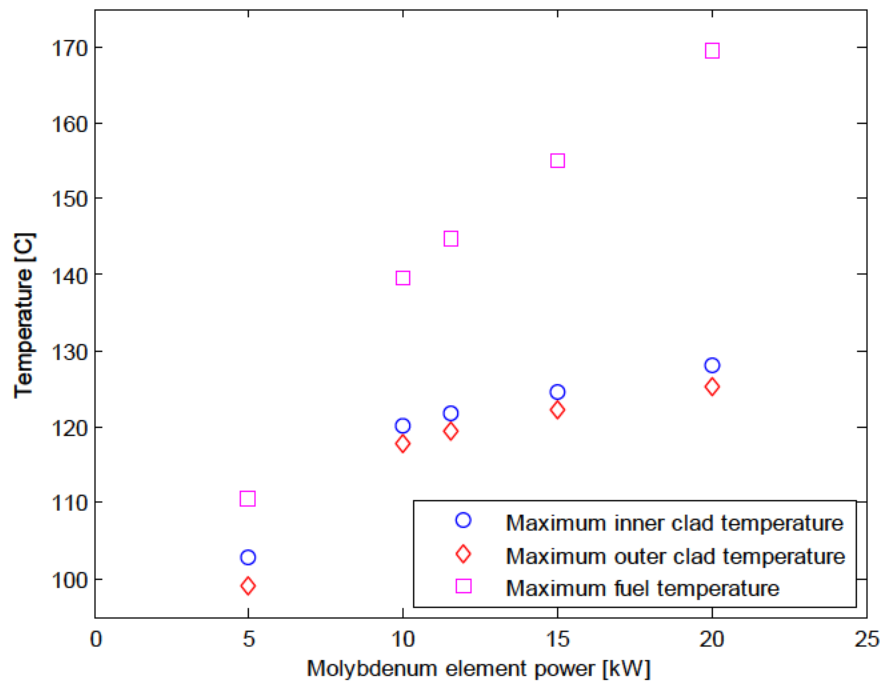


Figure 5-8: Power variation - maximum fuel and clad temperature

The axial and radial “hot band” temperatures at each power level are presented in Figure 5-9 and Figure 5-10.

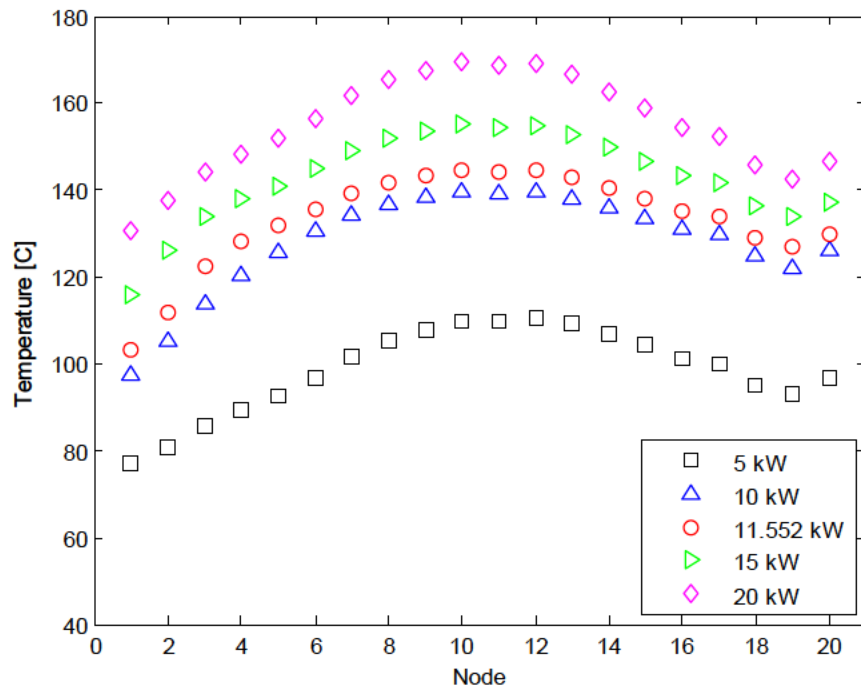


Figure 5-9: Power variation - axial hot bands

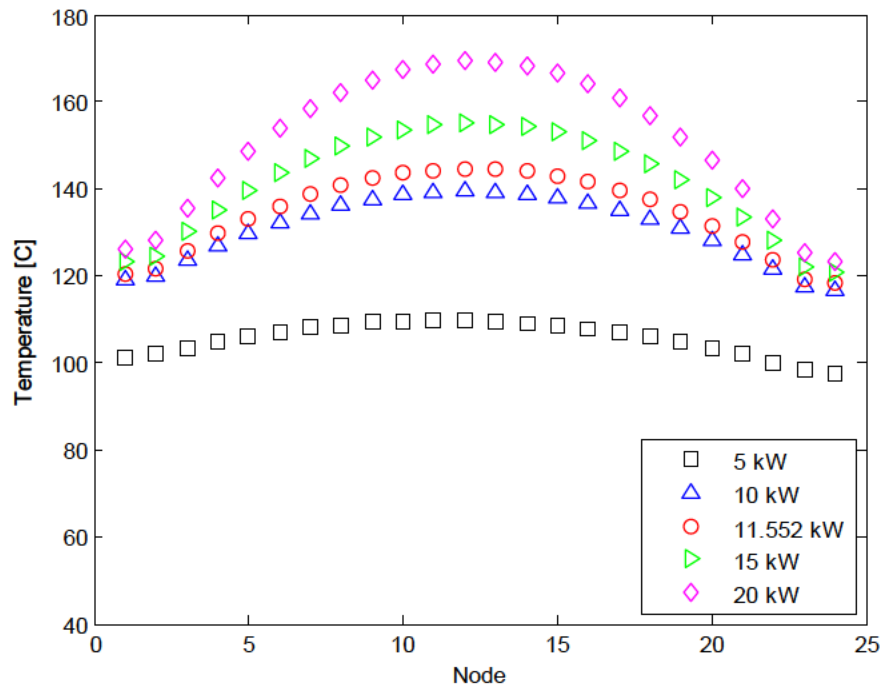


Figure 5-10: Power variation - radial hot bands

Predicted fuel temperatures did not exceed 170 °C and predicted clad temperatures did not exceed 129 °C. The values indicate that operation within the power range of 5 kW to 20 kW will result in maximum temperatures well within the limits described in Section 3.4. The profile of increasing clad temperatures indicates that small increases in maximum clad temperature require larger increases in maximum fuel temperature.

As presented in Table 5-2, coolant outlet temperatures and mass flow rates increased as molybdenum element power levels increased. These profiles indicate that increased molybdenum power levels resulted in larger amounts of heat transferred to the coolant and greater masses of coolant driven through the inner channel and outer channel via natural circulation.

As presented in Figure 5-8, the rise in outlet coolant temperatures was on the order of tens of °C per 5 kW increase.

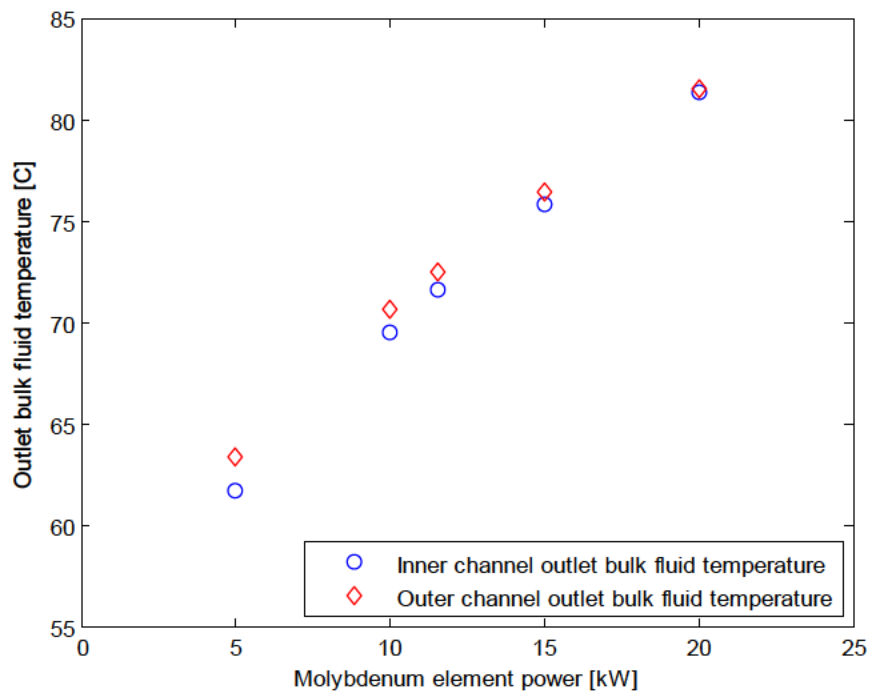


Figure 5-11: Power variation – channel outlet coolant temperature

Predicted coolant temperatures did not exceed 82 °C in the inner channel or outer channel. This value indicates that operation within the power range of 5 kW to 20 kW will result in maximum coolant temperatures below the saturation temperature of liquid water [52]. The inner channel and outer channel outlet temperatures approached a similar value at a molybdenum element power level of 20 kW.

As presented in Figure 5-12, the rise in coolant mass flow rates was on the order of hundredths of a kg/s per 5 kW increase.

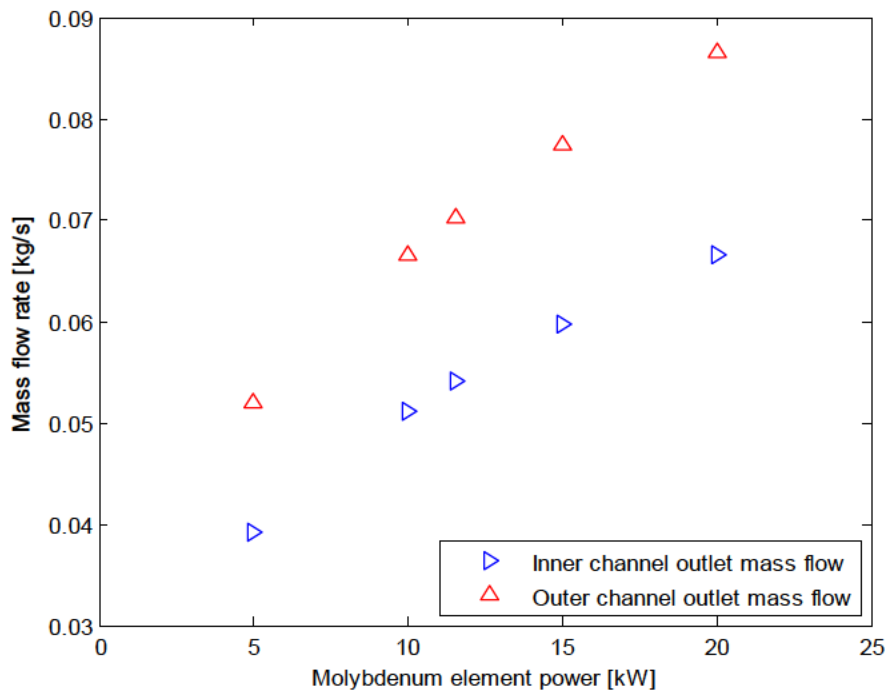


Figure 5-12: Power variation - channel outlet mass flow rate

Predicted coolant mass flow rates did not exceed 0.07 and 0.09 kg/s in the inner channel and outer channel, respectively, and exhibited steady behavior throughout model execution. Higher mass flow rates were predicted in the outer channel due to the larger form loss values within the inner channel. As indicated by Figure 5-12, the

increase in mass flow rate was more pronounced in the outer channel than in the inner channel.

The clad temperature profile presented in Figure 5-8 and the coolant profiles presented in Figure 5-11 and Figure 5-12 indicate that increased molybdenum element power levels resulted in increased heat transfer between the clad and coolant. As presented in Table 5-2, MCHFR decreased as molybdenum element power levels increased.

As presented in Figure 5-13, the magnitude of the decrease in MCHFR varied between the three predictive methods used per 5 kW increase.

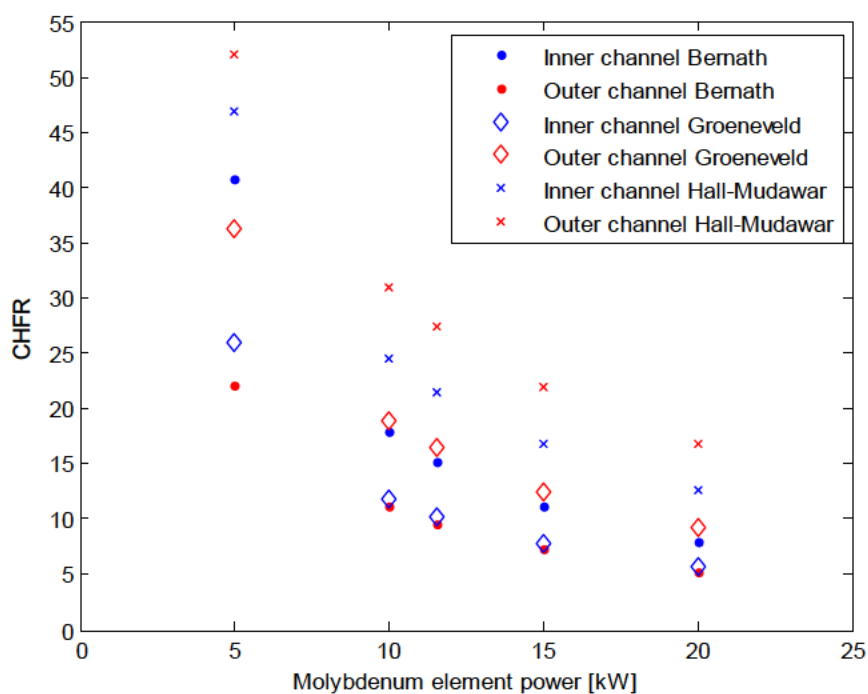


Figure 5-13: Power variation - MCHFR

The most conservative predicted MCHFR was found to be 5.28 in the outer channel from the Bernath correlation. This minimum value indicates that operation within a power range of 5 kW to 20 kW will result in MCHFR values well within safe margins. The Hall-Mudawar correlation predicted less limiting CHF than the Bernath

correlation or the Groeneveld look-up tables. This difference may be due to low mass fluxes ($\text{kg/m}^2\text{-s}$) in the inner and outer channel which lie below the minimum value prescribed by the Hall-Mudawar correlation. Predicted MCHFR profiles from all three methods indicate that MCHFR values decreased to a lesser degree per 5 kW increase as molybdenum element power levels rose.

6 CONCLUSION

6.1 Observations

This study determined and characterized the thermal hydraulic aspects related to the safety of deploying up to three molybdenum elements within the OSTR core during normal, full power operations. Limiting thermal hydraulic parameters include (1) maximum fuel temperature, (2) maximum cladding temperature, and (3) critical heat flux (CHF) ratios during steady-state operation. This objective was accomplished using RELAP5-3D version 2.4.2 through the development of a model representative of a single molybdenum element within the OSTR using the most conservative flow channel geometry possible – the OSTR’s B ring “hot channel.”

Predicted maximum fuel temperatures did not exceed $145\text{ }^\circ\text{C}$. This value is well below the melting temperature of UO_2 referred to in Section 3.4 as $2856 \pm 30\text{ }^\circ\text{C}$. Furthermore, the maximum fuel temperature predicted by RELAP5-3D is below the OSTR technical specification limit of $1,150\text{ }^\circ\text{C}$ [32].

Predicted maximum clad temperatures did not exceed $122\text{ }^\circ\text{C}$. This value is well below the melting temperature of aluminum referred to in Section 3.4 as $660\text{ }^\circ\text{C}$.

The most conservative predicted MCHFR was found to be 9.64 in the outer channel from the Bernath correlation. This minimum value is well within safe margins and correlates with the safe implementation of molybdenum elements within the OSTR core during steady state core operation.

Values from the Bernath and Groeneveld look-up table predicted more limiting CHF_Rs than those predicted from the Hall-Mudawar correlation. This difference may be due to low mass velocities ($\text{kg/m}^2\text{-s}$) in the inner and outer channel which lie below the minimum value prescribed by the correlation.

Examinations of the RELAP5-3D outputs indicate that the high surface area to volume ratio of the molybdenum element design provides very effective heat transfer from the fuel material to the coolant. Higher mass flow rates are maintained within the outer channel than in the inner channel. This difference may be attributed to the larger form loss calculated for the inner channel as opposed to those calculated for outer channel.

The results from this conservative safety analysis study predicted safe maximum fuel temperatures, maximum clad temperatures, and CHF_Rs for a molybdenum element implemented within the OSTR hot channel at an integral power level of 1.1 MW_{th}. The predicted profiles of limiting thermal hydraulic parameters at molybdenum element power levels ranging from 5 kW to 20 kW indicated safe implementation of a molybdenum element within the OSTR core.

The results from theoretical accident scenarios are presented within APPENDIX A: LOCA EVENT ANALYSIS and APPENDIX B: Flow Blockage analysis. Results for steady state and theoretical accident scenarios analyzed within this study are presented in Table 6-1.

Table 6-1: Summary of results

| Implementation condition | Maximum fuel temperature [°C] | Maximum clad temperature [°C] | MCHF _R |
|--------------------------|-------------------------------|-------------------------------|-------------------|
| Steady state | 144.66 | 121.69 | 9.64 |
| Steady state – 20 kW | 169.42 | 128.11 | 5.28 |
| LOCA event | 650.51 | 650.35 | -- |
| Blockage event | 224.40 | 224.40 | 4.84 |

6.2 Assumptions and Limitations

The application of RELAP5-3D, a lumped parameter code [7], introduces a number of assumptions into this thermal hydraulic analysis. Any relatively large component, such as the lower branch which models the OSTR lower plenum, is represented by a single volume, as are the time-dependent volumes which model the coolant source and sink. Heat structures, which are used to model the fueled and unfueled sections of the molybdenum element, are capable of only radial heat transfer and are incapable of any form of axial heat transfer in the scope of these models. This includes axial heat transfer to hydrodynamic volumes, other heat structures, or even adjacent heat structure nodes within the same heat structure. Furthermore, the assignment of specific types of components represented within RELAP such as branch, pipe, and junction components simplifies a physical system into one with specific characteristics expected by the RELAP code.

Results produced from this study pertain only to systems which explicitly mimic both geometric and boundary condition states representative of the OSTR.

6.3 Future Work

This study explored and detailed three limiting thermal hydraulic parameters regarding the implementation of a molybdenum element within the OSTR core during steady-state operations, and concluded that molybdenum elements may be safely implemented. A continuation of this work could contain analyses regarding any number of additional topics, including:

- The effect on molybdenum element limiting thermal hydraulic parameters caused by a positive reactivity insertion within the OSTR. Note however that, as discussed in Section 3, it is not the intent of reactor operators to perform rapid positive reactivity insertion experiment while molybdenum elements are loaded within the OSTR core.
- The effect on molybdenum element limiting thermal hydraulic parameters caused by variations in the assumed packing factor of 200 μm sphere-pac fuel.

- The effect on molybdenum element limiting thermal hydraulic parameters caused by implementation of an OSTR core filled with molybdenum elements.
- The effect on molybdenum element limiting thermal hydraulic parameters caused by a new molybdenum element power profile (if changed) after replacement of the OSTR graphite reflector.
- The effect on molybdenum element limiting thermal hydraulic parameters caused by implementation in TRIGA[®] reactors with parameters dissimilar to the OSTR.
- The effect on OSTR spatially distributed fluxes due to replacement of a fuel rod with a molybdenum element in notable grid-locations.
- The development of a potentially more resolved model via computational fluid dynamics (CFD)

7 REFERENCES

1. National Research Council. "2 Molybdenum-99/Technetium-99m Production and Use." Medical Isotope Production without Highly Enriched Uranium. Washington, DC: The National Academies Press, 2009. 1. Print. Accessed April 2, 2012.
2. Bechtel Marine Propulsion Corporation. Nuclides and Isotopes Chart of the Nuclides, Seventeenth Edition, 2010. Schenectady, New York.
3. IAEA, Technetium-99 radiopharmaceuticals, status and trends, IAEA, 2009, Vienna, Austria.
4. Saey, R.J P, The influence of radiopharmaceutical isotope production on the global radioxenon background, in *Journal of Environmental Radioactivity*, 2009, Vienna, Austria.
5. Steinbrook, R. Drug Shortages and Public Health, in *The New England Journal of Medicine*, 2009, Massachusetts, U.S
6. Eckelman W.C. Unparalleled Contribution of Technetium-99m to Medicine Over 5 Decades. *JACC: Cardiovascular Imaging*. March 10, 2009. Accessed April 2, 2012.
7. RELAP5-3D Code Development Team, Volume 1: code structure, system models, and solution methods, in RELAP5-3D code manual, *Idaho National Laboratory*, 2005. Idaho Falls, Idaho.
8. Marcum, W.R., Thermal Hydraulic Analysis of the Oregon State TRIGA Reactor Using RELAP5-3D, in *Nuclear Engineering & Radiation Health Physics Department*. 2008, Oregon State University: Corvallis, Oregon.
9. Marcum, W. R., B. G. Woods, et al. Experimental and Theoretical Comparison of Fuel Temperature and Bulk Coolant Characteristics in the Oregon State TRIGA Reactor During Steady State Operation, in *Nuclear Engineering and Design*, 2010, Oregon State University, Corvallis, Oregon.
10. Marcum, W. R., T. S. Palmer, et al. A Comparison of Pulsing Characteristics of the Oregon State TRIGA Reactor with FLIP and LEU Fuel, in *Nuclear Science and Engineering*, 2012, Oregon State University, Corvallis, Oregon.

11. Welch and Redvanly. Handbook of Radiopharmaceuticals: Radiochemistry and Applications, 2003, John Wiley and Sons, England, U.K.
12. Shih et al. Discordant Technetium-99m-MIBI and Technetium 99m-HMPAO Uptake of Recurrent Occipital Meningioma on Brain SPECT Images, in *Journal of Nuclear Medicine*, 1996, Lexington, Kentucky.
13. Cook et al. Technetium-99m-Labeled HL91 to Identify Tumor Hypoxia: Correlation with Fluorine-18-FDG, in *Journal of Nuclear Medicine*, 1998, London, U.K.
14. Taki et al. of P-Glycoprotein in Patients with Malignant Bone and Soft-Tissue Tumors Using Technetium-99m-MIB I Scintigraphy, in *Journal of Nuclear Medicine*, 1998, Kanazawa, Japan.
15. Learoyd et al. Technetium-99m- Sestamibi Scanning in Recurrent Medullary Thyroid Carcinoma, in *Journal of Nuclear Medicine*, 1997, St. Leonards, Australia.
16. Rossleigh et al. Technetium-99m Dimercapto succinic Acid Scintigraphy Studies of Renal Cortical Scarring and Renal Length, in *Journal of Nuclear Medicine*, 1998, Sydney, Australia.
17. Lee et al. Technetium-99m(V)-DMSA and Gallium-67 in the Assessment of Bone and Joint Infection, in *Journal of Nuclear Medicine*, 1998, Kaohsiung, Taiwan.
18. Burke, J. The Future Supply of Molybdenum-99, in *The Journal of Nuclear Medicine*, 1995.
19. Davis et al. Modeling the GFR with RELAP5-3D, in *2005 RELAP International Users Seminar*, 2005, the Idaho National Lab, Jackson Hole, Wyoming.
20. Omar et al. Thermal hydraulic analysis of Syrian MNSR research reactor using RELAP5/Mod3.2 code, in *Annals of Nuclear Energy*, 2010, Damascus, Syria.
21. Hedayat et al. Loss of coolant accident analyses on Tehran research reactor by RELAP5/MOD3.2 code, in *Progress in Nuclear Engineering*, 2007, Tehran, Iran.

22. Uspuras et al. Development of Ignalina NPP RBMK-1500 reactor RELAP5-3D model, in *Nuclear Engineering and Design*, 2003. Kaunas, Lithuania.
23. Feltus M. and Miller W. Three-dimensional coupled kinetics/thermal-hydraulic benchmark TRIGA experiments, in *Annals of Nuclear Energy*, 2000, Pennsylvania.
24. Costa et al. Thermal hydraulic analysis of the IPR-R1 TRIGA research reactor using a RELAP5 model, in *Nuclear Engineering and Design*, 2010, Belo Horizonte, Brazil.
25. Jensen R. and Newell D. Thermal hydraulic calculations to support increase in operating power in McClellan Nuclear Radiation Center(MNRC) TRIGA reactor, in *eScholarship University of California*, 1998, College Station, Texas.
26. Meloni P. and Polidori M. A neutronics–thermalhydraulics model for preliminary studies on TRADE dynamics, in *Nuclear Engineering and Design*, 2007, Bologna, Italy
27. Zvirin Y., A Review of Natural Circulation Loops in Pressurized Water Reactors and Other Systems, 1981, Electric Power Research Institute, Palo Alto, California
28. Van Bragt, D. and Van Der Hagen, T., Stability of Natural Circulation Boiling Water Reactors Part I – Description Stability Model and Theoretical Analysis in Terms of Dimensionless Groups, in *Nuclear Technology*, 1996, Mekelweg, The Netherlands.
29. Gebhardt B., Natural Convection Flows and Stability, in *Advances in Heat Transfer*, 1973, Ithaca, New York.
30. D.C. Groenveld, Post-dryout heat transfer at reactor operating conditions, *National topical meeting on water reactor safety, Salt Lake City, Utah, 1973*, Salt Lake City, Utah, 1973
31. Keller, T., Modeling the Oregon State University TRIGA Reactor Using the Three-Dimensional Deterministic Transport Code, 2007, Oregon State University, Corvallis, Oregon.

32. Reese, S., et al., Oregon State University, Safety Analysis Report for the Conversion of the Oregon State TRIGA[®] Reactor from HEU to LEU Fuel, 2007, Corvallis, Oregon
33. Groenveld et al., The 2006 CHF look-up table, in *Nuclear Engineering and Design*, 2007
34. Huda M. and Bhuiyan S. Investigation of thermohydraulic parameters during natural convection cooling of TRIGA reactor, in *Annals of Nuclear Energy*, 2006, Dhaka, Bangladesh.
35. Zuber N. Hydrodynamic Aspects of Boiling Heat Transfer, 1959, Los Angeles, California.
36. Feldman E.E. Fundamental Approach to TRIGA Steady-State Thermal-Hydraulic CHF Analysis, 2007, Argonne National Lab, Chicago, Illinois.
37. Bernath, L., A Theory of Local-Boiling Burnout and its Application to Existing Data, in *Chemical engineering progress symposium series*, 1960.
38. Nijhawan et al., Measurement of vapor superheat in post-critical-heat-flux-boiling, in *Journal of Heat Transfer*, 1980, Bethlehem, Pennsylvania.
39. RELAP5-3D Code Development Team, Volume 4: Models and Correlations, in RELAP5-3D code manual, *Idaho National Laboratory*, 2005. Idaho Falls, Idaho.
40. Groenveld et al., 1986 AECL-UO Critical Heat Flux Lookup Table, in *Heat Transfer Engineering*, 1986.
41. Groenveld et al., The 1995 CHF look-up table for critical heat flux in tubes, in *Nuclear Engineering and Design*, 1996
42. Hall and Mudawar, Critical heat flux (CHF) for water flow in tubes – Subcooled CHF correlations, *International Journal of Heat and Mass Transfer*, 2000, West Lafayette, Indiana
43. Kalimullah et al., An Evaluation of Subcooled CHF Correlations and Databases For Research Reactors Operating at 1 to 50 bar Pressure, *RETR 2012 – 34th International Meeting On Reduced Enrichment for Research and Test Reactors*, 2012, Argonne National Laboratory, Argonne. Illinois

44. Schickler, R., Comparison of HEU and LEU Neutron Spectra in Irradiation Facilities at the Oregon State TRIGA[®] Reactor, 2012
45. Degueudre and Paratte, Basic Properties of a Zirconia-Based Fuel Material for Light Water Reactors, *Nuclear Technology*, 1998
46. Marcum et al., A Comparison of Pulsing Characteristics of the Oregon State University TRIGA[®] Reactor with FLIP and LEU Fuel, *Nuclear Science and Engineering*, 2012.
47. Marcum, W.R., Determination of the Form Losses in the OSTR Molybdenum Element, Oregon State University, 2011, Corvallis, Oregon.
48. Byfield and Marcum, Analysis of the Steady State Thermal Hydraulic Behavior of the Oregon State TRIGA[®] Reactor – Molybdenum Element -, Oregon State University, 2011, Corvallis, Oregon
49. Peddicord et al., Analytical and Experimental Performance of Sphere-pac Nuclear Fuels, *Progress in Nuclear Energy*, 1986
50. Hall, R.O.A., D.G. Martin, and M.J. Mortimer, The Thermal Conductivity of UO₂ Sphere-Pac Beds, in *Journal of Nuclear Materials*, 1990. **173**: p. 130-141.
51. Popov, S.G et al., Thermophysical Properties of MOX and UO₂ Fuels Including the Effects of Radiation, 2000, Oak Ridge National Laboratory, Oak Ridge, Tennessee.
52. Incropera et al., Fundamentals of Heat and Mass Transfer – Sixth Edition, 2007, John Wiley & Sons, Inc.
53. White, Fluid Mechanics – Seventh Edition, 2011, McGraw-Hill Companies, Inc.
54. Moon and Campbell, Effects of Moderately High Strain Rates on the Tensile Properties of Metals, 1962, Defense Metals Information Center, Columbus, Ohio.
55. Simnad et al., Fuel Elements for Pulsed TRIGA Research Reactors, *Nuclear Technology*, 1976.
56. Ashby M., Materials Selection in Mechanical Design – Fourth Edition, 2010, Butterworth-Heinemann.

57. Callister Jr., *Materials Science and Engineering – an Introduction*, 2007, John Wiley & Sons, Inc.
58. RELAP5-3D Code Development Team, Volume 5: User's Guidelines, in RELAP5-3D code manual, Idaho National Laboratory, 2005. Idaho Falls, Idaho.
59. Veca, A.R., TRIGA[®] Reactor Thermal-Hydraulics Study STAT-RELAP5 Comparison, General Atomics, 2008
60. RELAP5-3D Code Development Team, Appendix A: RELAP5-3D[®] Input Data Requirements, in RELAP5-3D code manual, Idaho National Laboratory, 2005. Idaho Falls, Idaho.
61. Geelwood et al., FRAPCON-3.4: A Computer Code for the Calculation of Steady-State Thermal-Mechanical Behavior of Oxide Fuel Rods for High Burnup, 2011, Pacific Northwest National Laboratory, Richland, Washington.

8 NOMENCLATURE

Variables

| | |
|--------------|---|
| CHF | Critical heat flux, [kW/m] |
| k_1 | Diameter factor |
| k_2 | Rod-bundle geometry factor |
| k_3 | Grid spacer factor |
| k_4 | Heated length factor |
| k_5 | Axial flux distribution factor |
| k_6 | Vertical flow factor |
| D_h | Hydraulic diameter, [m] |
| X | Equilibrium quality |
| D_H | Heated diameter, [m] |
| L | Heated length from channel inlet, [m] |
| ρ_g | Density of vapor, [kg/m ³] |
| ρ_f | Density of fluid, [kg/m ³] |
| $(Q/A)_{BO}$ | CHF, [W/m ²] |
| h_{BO} | Limiting film coefficient, [W/m ² -°C] |
| T_w | Temperature of the wall at CHF, [°C] |
| T_b | Bulk temperature of the fluid, [°C] |
| D_h | Hydraulic diameter, [m] |
| D_H | Heated diameter, [m] |
| Δ | “Slope” |
| P_{abs} | Pressure (absolute), [Pa] |
| v | Velocity of the fluid, [m/s] |
| q_c | Critical heat flux [kW/m ²] |
| G | Mass flux [kg/m ² -s] |
| h_i | Enthalpy at the inlet [kJ/kg] |
| $h_{f,o}$ | Enthalpy of the fluid at the outlet [kJ/kg] |
| $h_{fg,o}$ | Latent heat of vaporization, outlet [kJ/kg] |
| σ | Surface tension [N/m] |

| | |
|------------------------|--|
| L | Heated length [m] |
| $A_{\text{fuel core}}$ | Area of the Molybdenum Element Fuel Core, [m ²] |
| D_{outer} | Diameter of the Molybdenum Element's outer cladding, [m] |
| D_{inner} | Diameter of the Molybdenum Element's inner cladding, [m] |
| σ_{θ} | Stress caused by internal pressure, [Pa] |
| P | Internal pressure within the Molybdenum Element, [Pa] |
| b | Radius of a cylinder, [m] |
| t | Cladding thickness of the Molybdenum Element, [m] |
| b_{outer} | Radius of the Molybdenum Element to the outer clad, [m] |
| b_{inner} | Radius of the Molybdenum Element to the inner clad, [m] |
| E | Young's Modulus, [Pa] |
| I | Second moment of area [m ⁴] |
| R | Radius of the tube [m] |
| V_{gas} | Total gas volume within the Molybdenum Element, [m ³] |
| n_{gas} | Number of moles of gas within the Molybdenum Element, [moles] |
| R_{gas} | Universal gas constant, [J/mol*°C] |
| T | Temperature, [°C] |
| A_{outer} | Area of the Molybdenum Element's outer flow channel, [m ²] |
| Pitch | Pitch of the OSTR core [m] |
| A_{inner} | Area of the Molybdenum Element's inner flow channel, [m ²] |
| K | Piping system loss coefficient |
| ΔP | Change in pressure across a piping system, [Pa] |
| ρ | Density, [kg/m ³] |
| v | Velocity, [m/s] |
| d | Small diameter in a sudden expansion/contraction, [m] |
| D | Large diameter in a sudden expansion/contraction, [m] |
| k_{95} | Thermal conductivity for 95% theoretical density fuel, [W/m*°C] |
| Bu | Burn-up, [GWd/MTU] |
| $f(\text{Bu})$ | Effect of fission products in crystal matrix (solution), [GWd/MTU] |
| $g(\text{Bu})$ | Effect of irradiation defects, [(GWd/MTU) ^{2/3}] |
| Q | Temperature dependence parameter, [°C] |

| | |
|---------------|---|
| A | Constant, [$m^{\circ}C/W$] |
| a | Constant |
| gad | Weight fraction of gadolinia [% mass] |
| B | Constant, [$m^{\circ}C/W/^{\circ}C$] |
| E | Constant, [$W^{\circ}C/m$] |
| F | Constant, [$^{\circ}C$] |
| k_d | Thermal conductivity for a theoretical dense fuel, [$W/m^{\circ}C$] |
| d | Density of fuel as a fraction of total density, [% density] |
| C_f | Specific heat capacity, [$J/kg^{\circ}C$] |
| VF | Volume fraction |
| ρ_{UO_2} | Density of UO_2 [kg/m^3] |
| C_{p,UO_2} | Specific heat capacity of UO_2 [$J/kg^{\circ}C$] |
| ρ_{He} | Density of Helium [kg/m^3] |
| $C_{p,He}$ | Specific heat capacity of helium [$J/kg^{\circ}C$] |

Acronyms

| | |
|--------------------|---|
| Tc-99m | Technetium-99 metastable |
| Mo-99 | Molybdenum-99 |
| OSU | Oregon State University |
| TRIGA [®] | Training, Research, Isotope, General Atomic |
| OSTR | Oregon State TRIGA [®] Reactor |
| UO_2 | Uranium oxide |
| HEU | High enriched uranium |
| LEU | Low enriched uranium |
| CHF | Critical heat flux |
| LOCA | Loss of coolant accident |
| IAEA | International Atomic Energy Agency |
| GFR | Gas Fast Reactor |
| MNSR | Syrian Miniature Neutron Source Reactor |
| RBMK | Reaktor Bolshoy Moshchnosti Kanalnyi |
| IPR-R1 | Instituto de Pesquisas Radiativas – Reactor 1 |

| | |
|---------|---|
| MNRC | Davis McClellan Nuclear Radiation Center |
| RC-1 | Reattore Casaccia-1 |
| NRC | Nuclear Regulatory Commission |
| OND | Onset of nucleate boiling |
| DNB | Departure from nucleate boiling |
| CHFR | Critical heat flux ratio |
| AECL-UO | Atomic Energy of Canada Ltd. – University of Ottawa |
| SAR | Safety analysis report |
| UZrH | Uranium-zirconium hydride |
| ICIT | In-core irradiation tube |
| CLICIT | Cadmium-lined in-core irradiation tube |
| BOL | Beginning of life |
| MOL | Middle of life |
| EOL | End of life |
| HS | Heat structure |
| SCRAM | Reactor shutdown, “safety control rod axe man” |
| CFD | Computational fluid dynamics |

9 APPENDIX A: LOCA EVENT ANALYSIS

9.1 Description

The predicted results of a theoretical loss of coolant accident (LOCA) paired with an emergency reactor shutdown (SCRAM) are examined in this appendix. In this postulated event, the OSTR is assumed to be continuously operating at a 1.1 MW steady-state power level until a sudden leak in the OSTR's bioshield occurs. An immediate SCRAM is assumed to take place as a result of leak detection, which causes reactor power levels to drop according to the ANSI/ANS 5.1-2005 standard for Decay Heat Power in Light Water Reactors as shown in Figure 9-1.

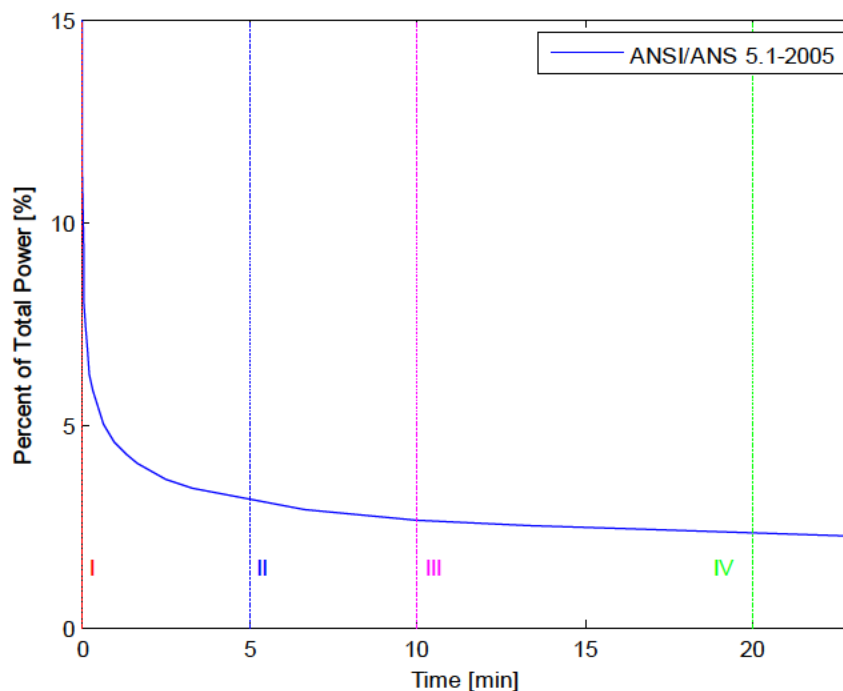


Figure 9-1: Decay power profile

After a specific “cool down period”, the reactor pool is assumed to fully drain as a result of the leak, forcing the reactor core into an air-only environment. Four separate cool down periods were analyzed via the designation of four “scenarios” to determine limiting thermal hydraulic parameters related to the implementation of a molybdenum

element within the OSTR core. This LOCA event transient models a simplified case of one possible accident which may occur while a molybdenum element is present within the OSTR core.

9.2 Approach

The LOCA event analysis is performed by the use of RELAP5-3D “restart” decks. These decks function by loading the conditions found within an RELAP5-3D output file as initial conditions for a new simulation [7]. A total of four restart decks and four output decks were used to perform this LOCA event analysis. Each output deck loaded for an LOCA event scenario is similar to that of the steady-state results presented in Section 5.1, but includes a “cool down” period of varying length which models time between reactor SCRAM and core exposure. Reactor SCRAM power drop-off is modeled by the use of a general table which imposes powers aligned with Figure 9-1 into the fuel material heat structure. A summary of each LOCA event scenario is displayed in Table 9-1.

Table 9-1: LOCA event scenario results

| Control Variables | LOCA event scenario | | | |
|----------------------------|---------------------|----------|----------|---------|
| | I | II | III | IV |
| Cool-down period [s] | 0 | 300 | 600 | 1200 |
| Power at core uncover [kW] | 11.5522 | 0.335476 | 0.308559 | 0.27094 |

Instantaneous core uncovering is modeled by the introduction of non-condensable gas qualities of 1.0 for all hydrodynamic volumes within each restart file. Nitrogen was chosen as the non-condensable gas species to be loaded within RELAP5-3D decks for this study as a means to model an air-only environment. The nitrogen gas modeled in this study is at a pressure of 101 kPa and a temperature of 42 °C. These conditions correspond with the atmospheric pressure value in Corvallis, Oregon, and the highest ever recorded ambient temperature in Corvallis, Oregon.

The “reflood” heat structure option, which allows for axial heat transfer to occur within a heat structure under specific conditions [7], is included in LOCA event scenarios. This option aids in preventing axial temperature “banding” to occur, wherein axially adjacent heat structures sub-volumes may considerably range in temperature while radially-adjacent sub-volumes experience near identical temperatures. The reflood option is restricted in its application to heat structures with adjacent hydrodynamic volumes with pressures lower than 1.2 MPa and void fractions (the volume fraction of gas to the total volume) greater than 0.1 [7]. These restrictions prevent the reflood option being included in other safety analyses performed within this study.

9.3 Results

As stated in section 1.2, the most important parameters dictating the safety of a molybdenum element are (1) maximum fuel temperature, (2) maximum cladding temperature, and (3) critical heat flux (CHF) ratios during steady-state operation. In a non-steady-state system, the values of the maximum fuel temperature and maximum cladding temperature as functions of time are the two most important parameters. These values are detailed for each LOCA event scenario in Table 9-2.

Table 9-2: LOCA event scenario maximum temperatures

| Scenario | Cool down time [min] | Fuel temperature at core uncover [$^{\circ}$ C] | Maximum fuel temperature [C] | Maximum clad temperature [C] |
|----------|----------------------|--|------------------------------|------------------------------|
| I | 0 | 105.77 | 650.51 | 650.35 |
| II | 5 | 57.73 | 614.53 | 614.28 |
| III | 10 | 54.80 | 598.01 | 597.86 |
| IV | 20 | 53.26 | 575.39 | 575.24 |

Table 9-2 indicates that more limiting thermal hydraulic parameters result from models with a decreased cool down periods. Due to the inclusion of the reflood option, the predicted temperature of each heat structure sub-volume within the fuel material is dependent upon the internal source profile within the entire heat structure and the cooling effectiveness of the inner channel and outer channel at every axial location.

Predicted maximum fuel temperatures for each LOCA event scenario as a function of time are displayed in Figure 9-2 along with the molybdenum element clad melting temperature referenced in Section 3.4.

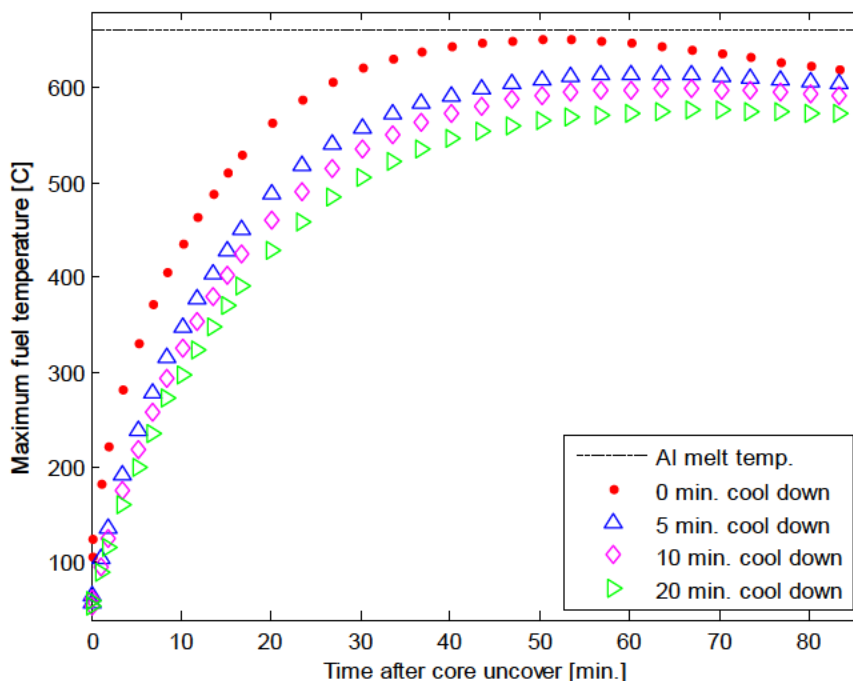


Figure 9-2: LOCA event scenarios - maximum fuel temperature

Predicted maximum fuel temperatures during the LOCA event scenarios did not exceed 651 °C. This value is much larger in magnitude than that predicted for steady state conditions, but well below the melting temperature of UO_2 referred to in Section 3.4 as 2856 ± 30 °C. Furthermore, it is below the technical specification limit of 1,150 °C [32].

Predicted maximum clad temperatures were of similar values to predicted maximum fuel temperatures and did not exceed 651 °C during LOCA event scenario I. This value approached but did not exceed reached the melting temperature of aluminum referred to in Section 3.4 as 440 °C.

Predicted maximum clad temperatures were of similar values to predicted maximum fuel temperatures and did not exceed 615 °C, 598 °C, and 576 °C during LOCA event scenarios II, III, and IV, respectively. These values did not exceed reached the melting temperature of aluminum referred to in Section 3.4 as 440 °C.

The predicted maximum fuel temperature profiles presented in Figure 9-2 vary in temperature development with respect to time. This variation results from a difference in molybdenum element power levels as a function of time between each LOCA event scenario. The slow decrease in fuel temperature after peaking for each LOCA event scenario illustrates the slow rate at which molybdenum element power decreases via the ANSI/ANS 5.1-2005 standard after the initial power drop-off.

RELAP5-3D predicted fuel material temperature profiles at peak temperature for each LOCA event scenario are presented in Figure 9-3, Figure 9-4, Figure 9-5, Figure 9-6, Figure 9-7, Figure 9-8, Figure 9-9, and Figure 9-10, respectively.

The axial and radial “hot band” temperatures are presented in Figure 9-11, Figure 9-12, Figure 9-13, and Figure 9-14.

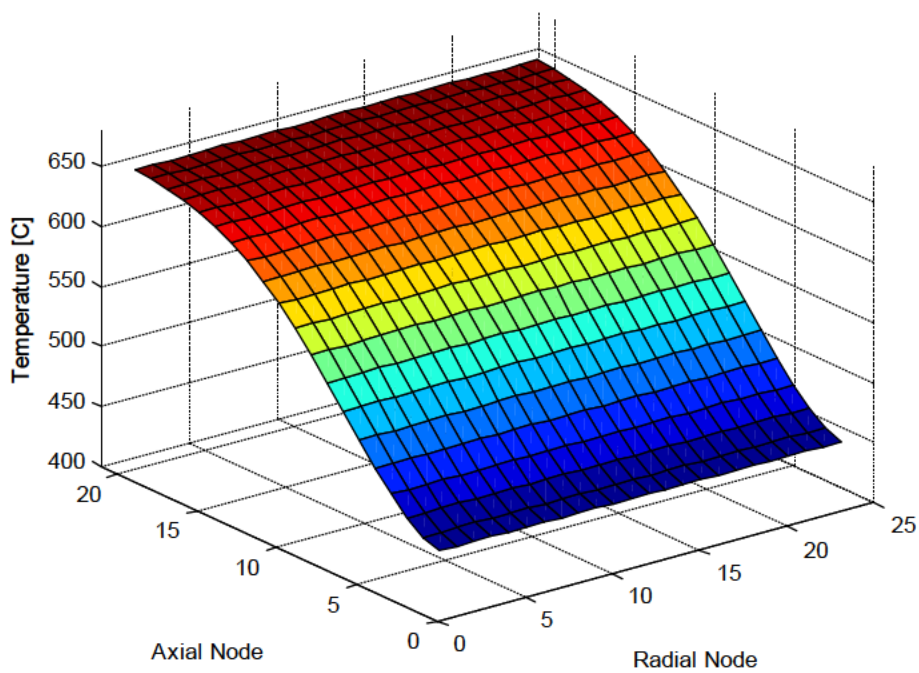


Figure 9-3: LOCA event scenario I - fuel temperature at peak

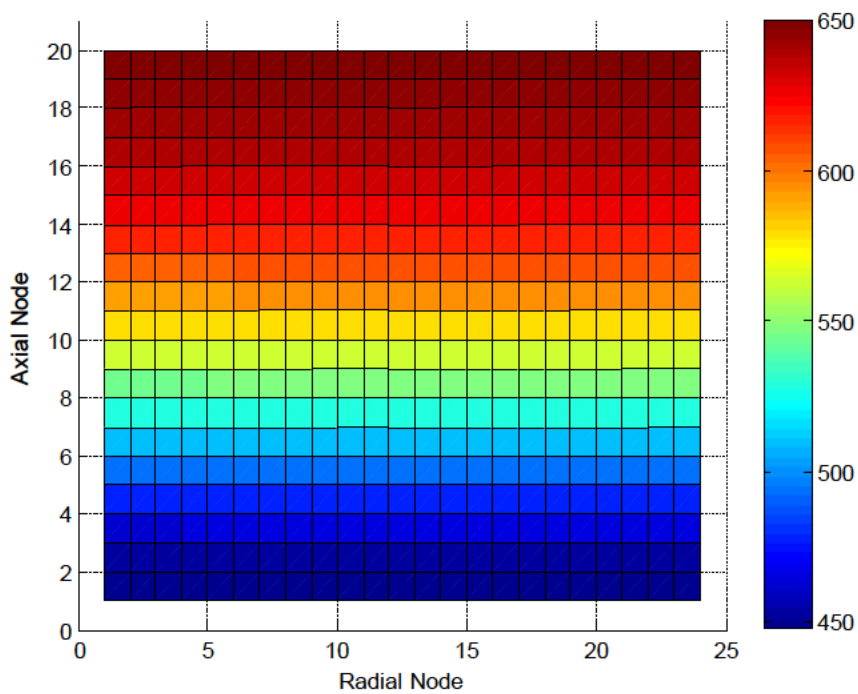


Figure 9-4: LOCA event scenario I - fuel temperature at peak

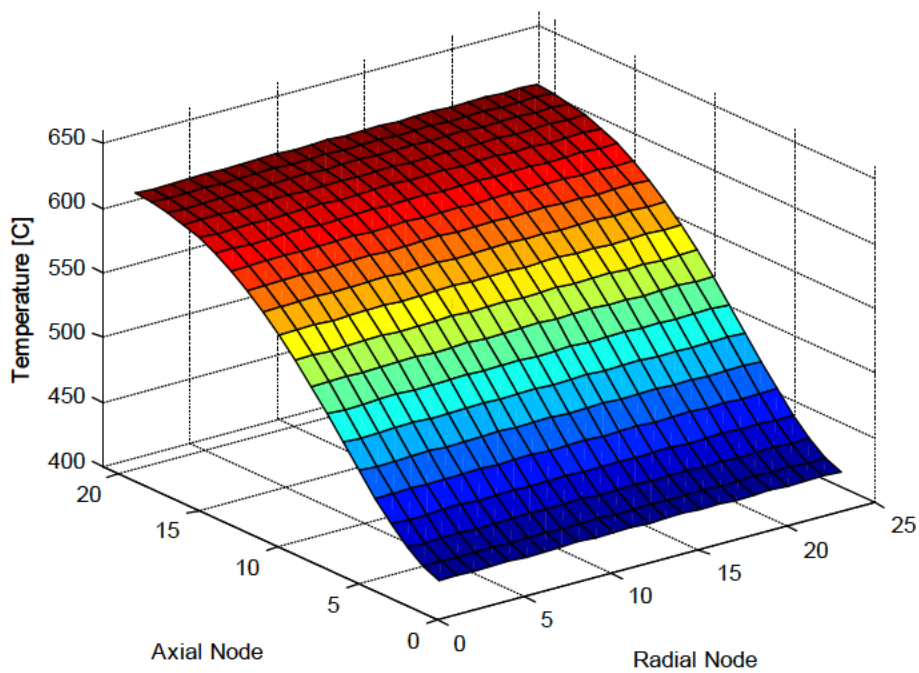


Figure 9-5: LOCA event scenario II - fuel temperature at peak

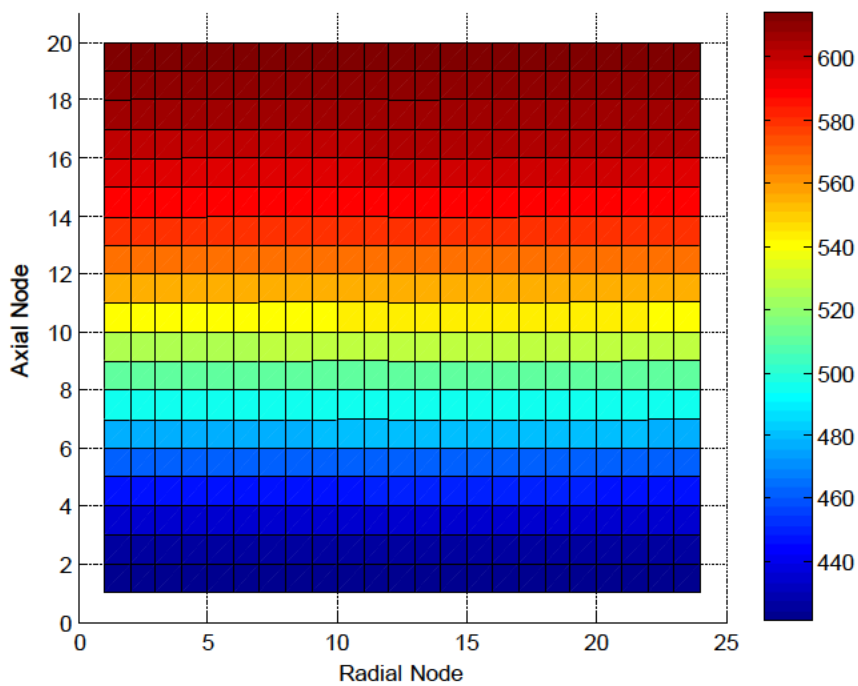


Figure 9-6: LOCA event scenario II - fuel temperature at peak

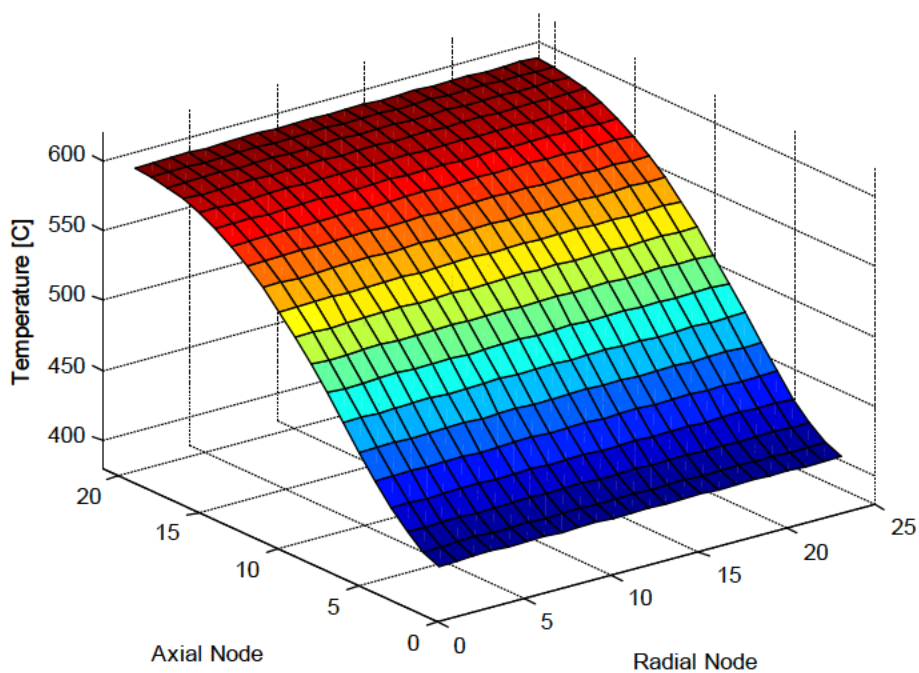


Figure 9-7: LOCA event scenario III - fuel temperature at peak

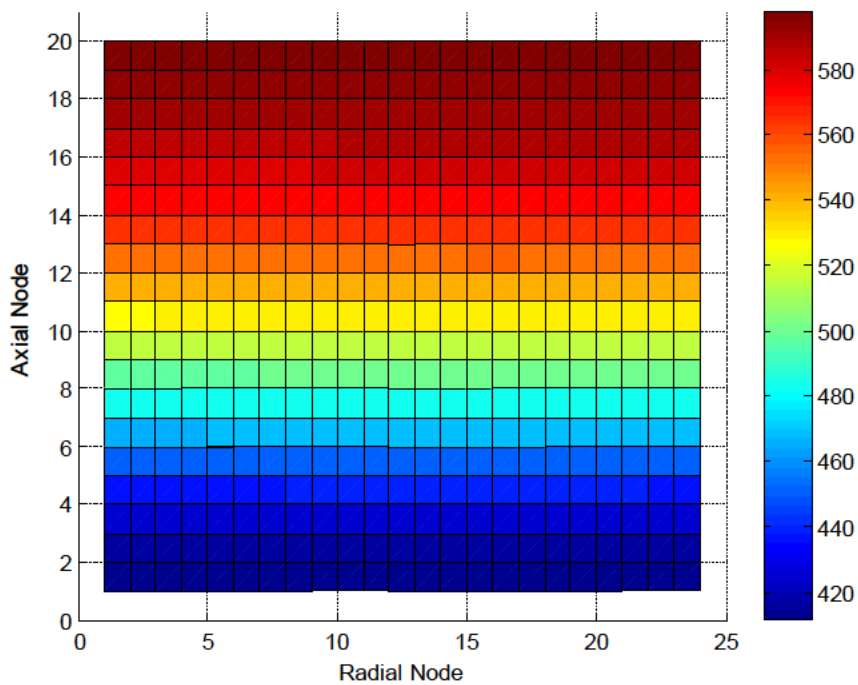


Figure 9-8: LOCA event scenario III - fuel temperature at peak

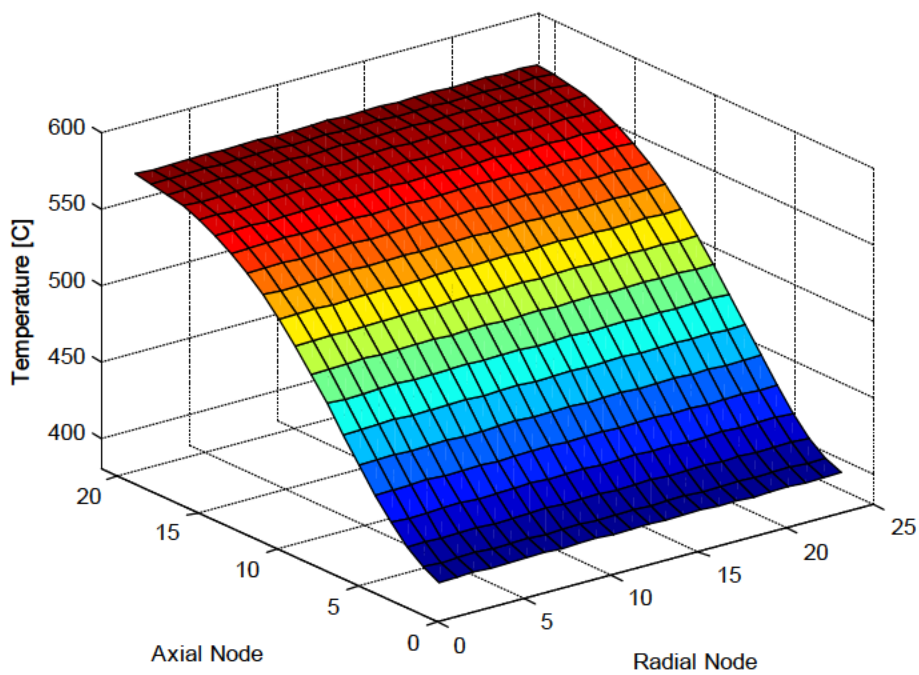


Figure 9-9: LOCA event scenario IV - fuel temperature at peak

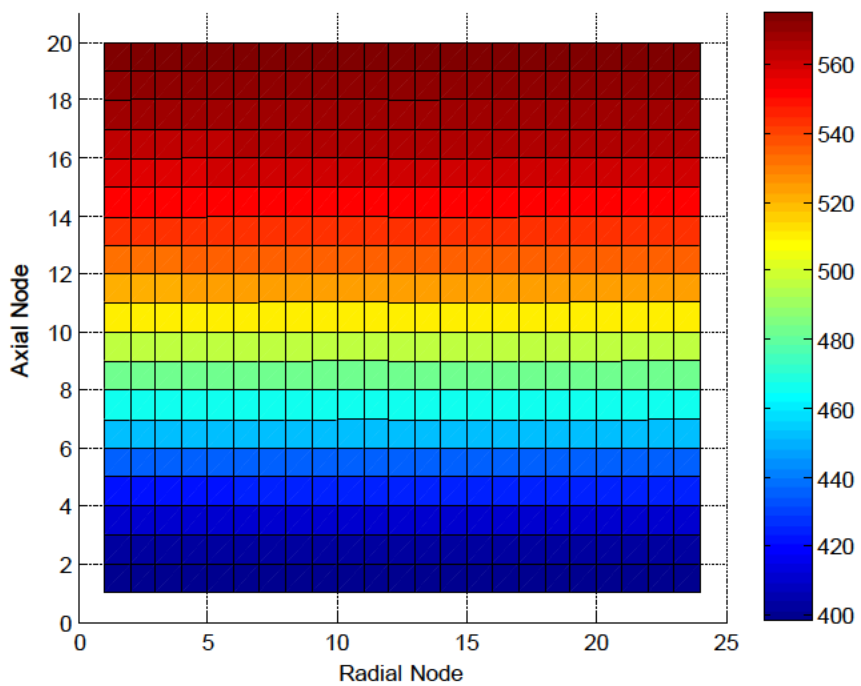


Figure 9-10: LOCA event scenario IV - fuel temperature at peak

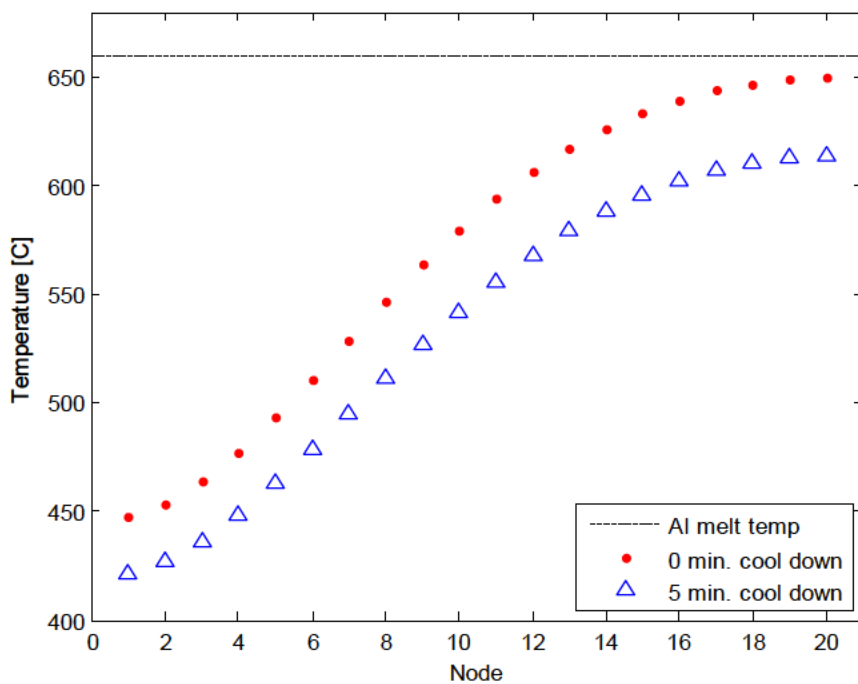


Figure 9-11: LOCA event scenario I & II - axial hot bands at peak

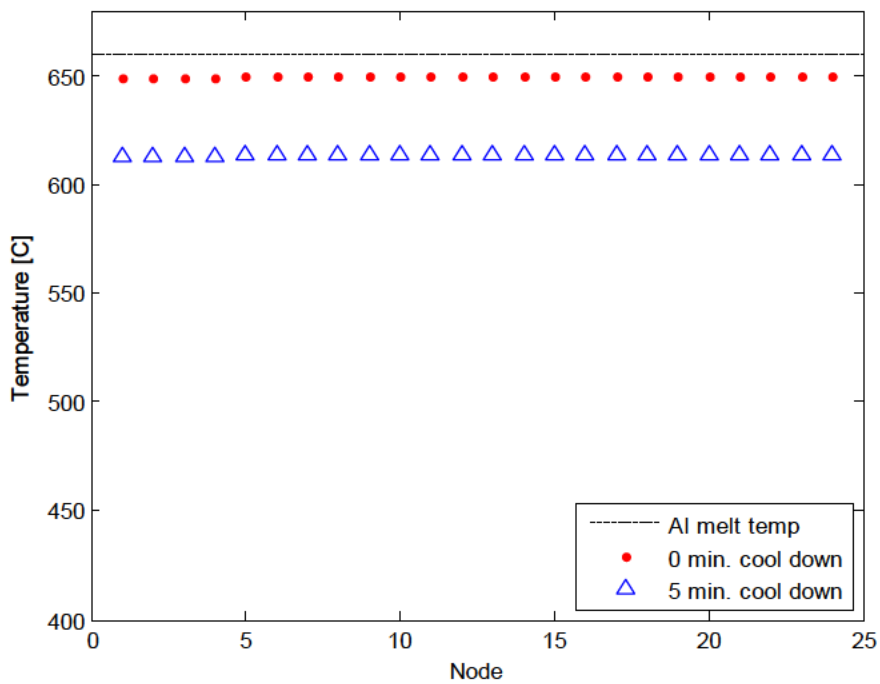


Figure 9-12: LOCA event scenario I & II - radial hot bands at peak

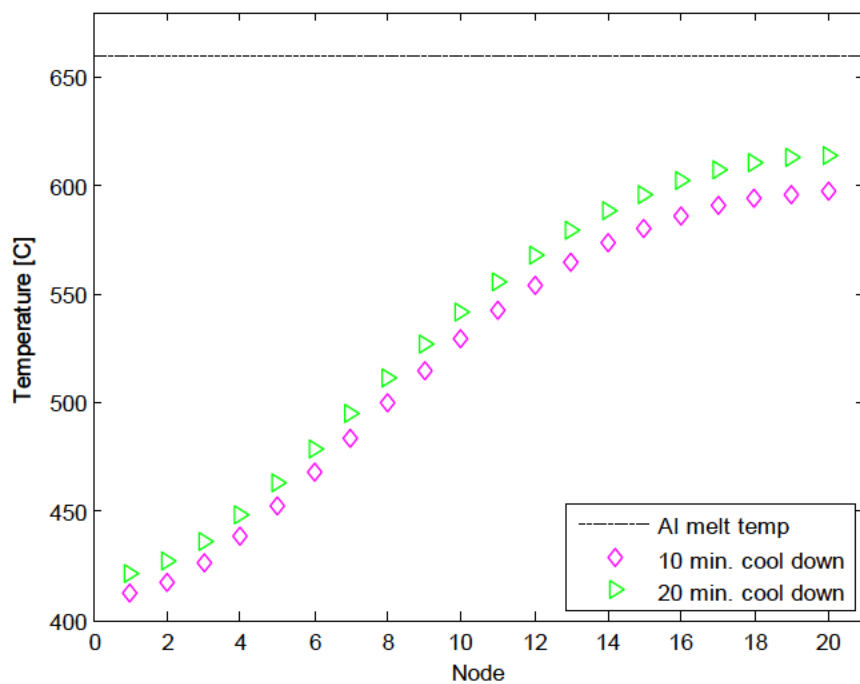


Figure 9-13: LOCA event scenario III & IV - axial hot bands at peak

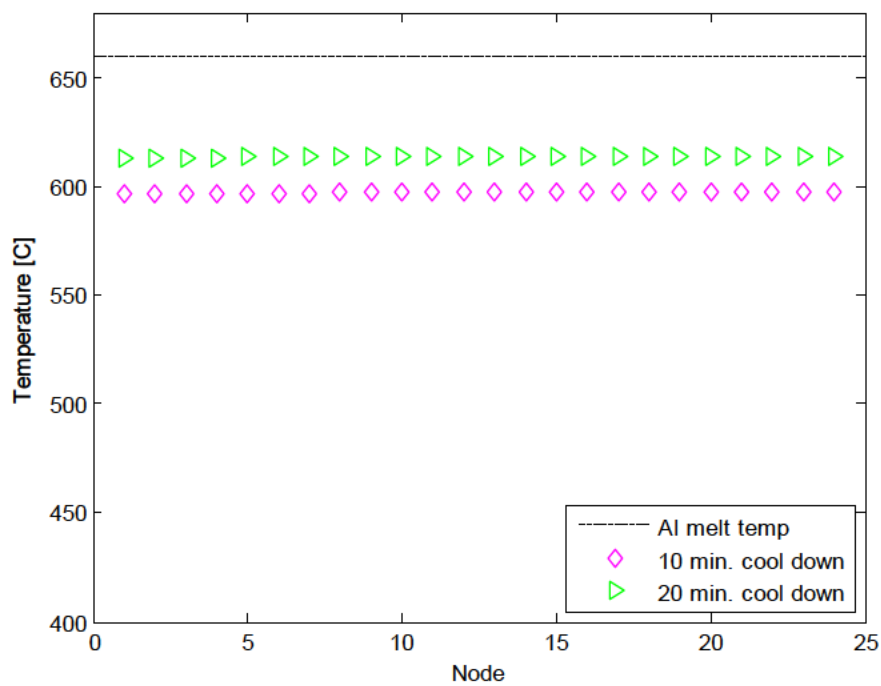


Figure 9-14: LOCA event scenario III & IV - radial hot bands at peak

The predicted fuel material temperature profiles presented in Figure 9-3 through Figure 9-10 indicate that maximum fuel temperatures develop within sub-volumes at a location near the heat structure's topmost axial position. The development of a fuel "hot band" at this location indicates that effective cooling from the nitrogen coolant is not available at these axial locations. The development of a distinct curved profile within the fuel material indicates that heat is axially transferred from the hot band towards the bottommost sub-volumes where cooling is most effective.

The predicted clad temperature profiles presented in Figure 9-3 through Figure 9-10 indicate that maximum cladding temperatures develop within sub-volumes at a location within the same hot band where maximum fuel temperatures develop. Clad sub-volumes adjacent to the outer channel within the hot band develop slightly higher temperatures than those sub-volumes adjacent to the inner channel. Sub-volumes which develop the highest clad temperatures indicate locations of elevated conductive heat transfer from the fuel material centerline and locations of limited cooling effectiveness from the nitrogen coolant.

The cooling effectiveness provided to the molybdenum element clad sub-volumes is dependent upon the coolant properties in the inner channel and outer channel, respectively, at each hydrodynamic sub-volume. The coolant temperature and velocity profiles for each LOCA event scenario, presented in Figure 9-15, Figure 9-16, Figure 9-17, Figure 9-18, respectively, display the coolant characteristics within the inner channel and the outer channel along the axial flow length.

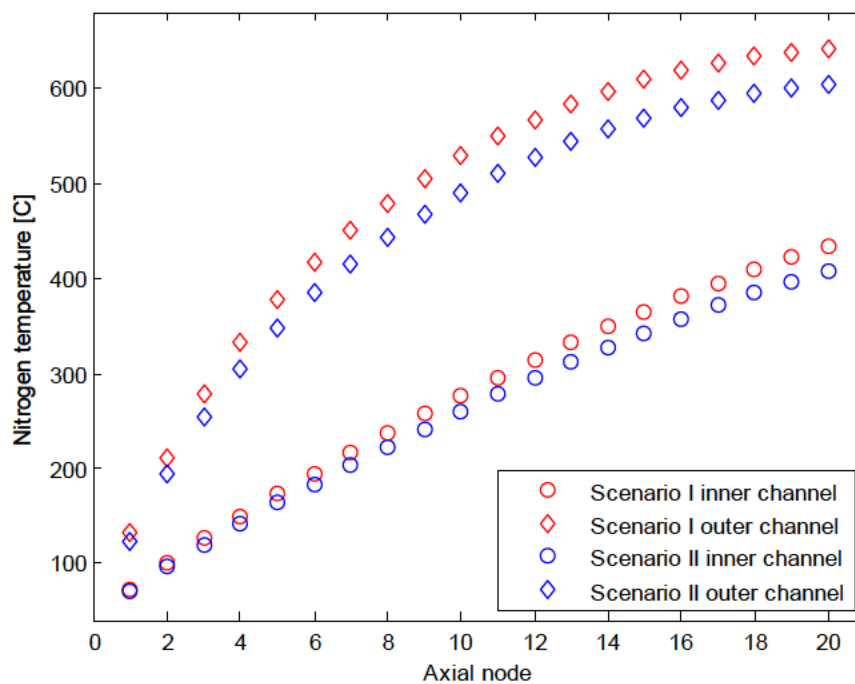


Figure 9-15: LOCA event scenario I & II - nitrogen temperature at peak

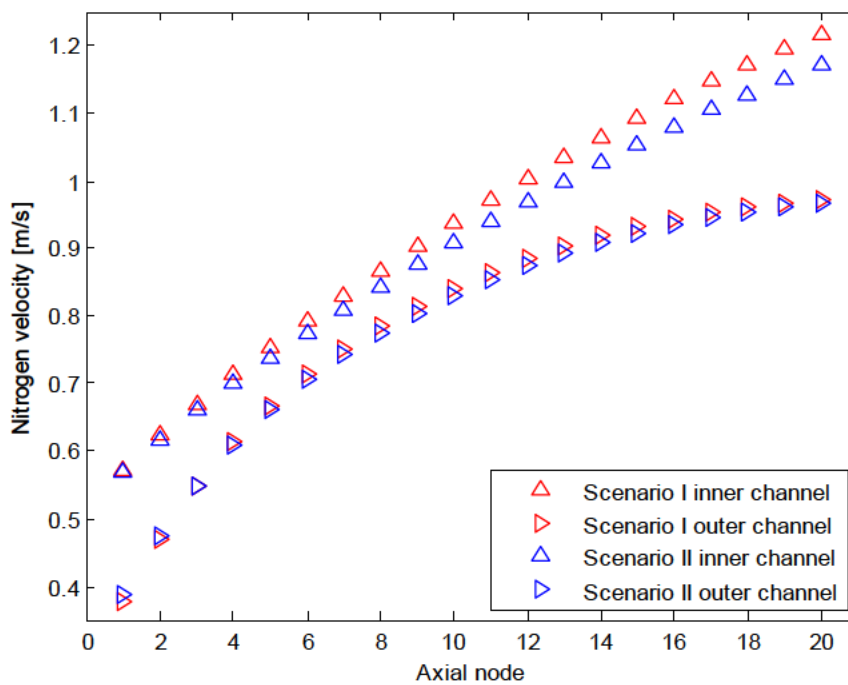


Figure 9-16: LOCA event scenario I & II - nitrogen velocity at peak

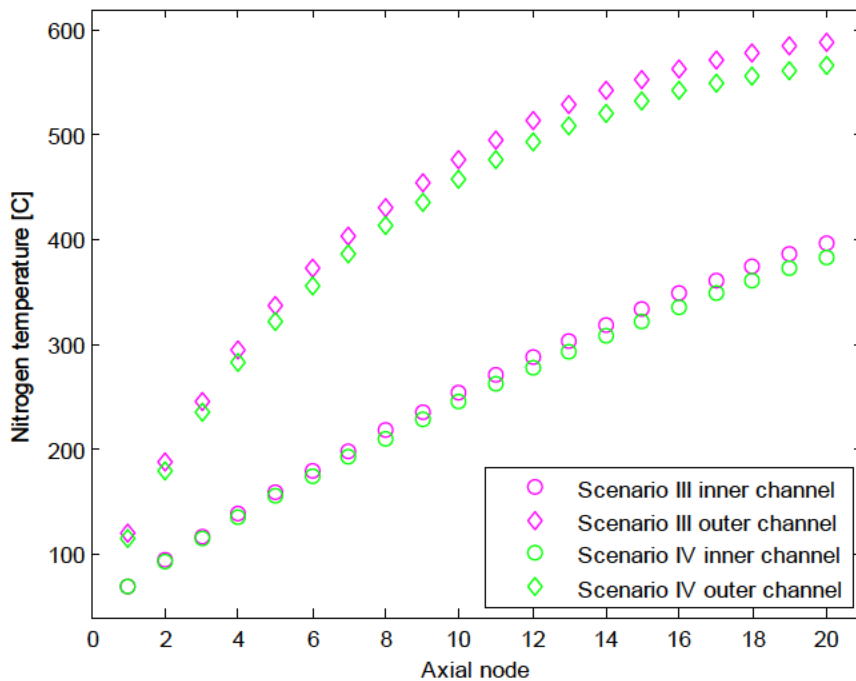


Figure 9-17: LOCA event scenario III & IV - nitrogen temperature at peak

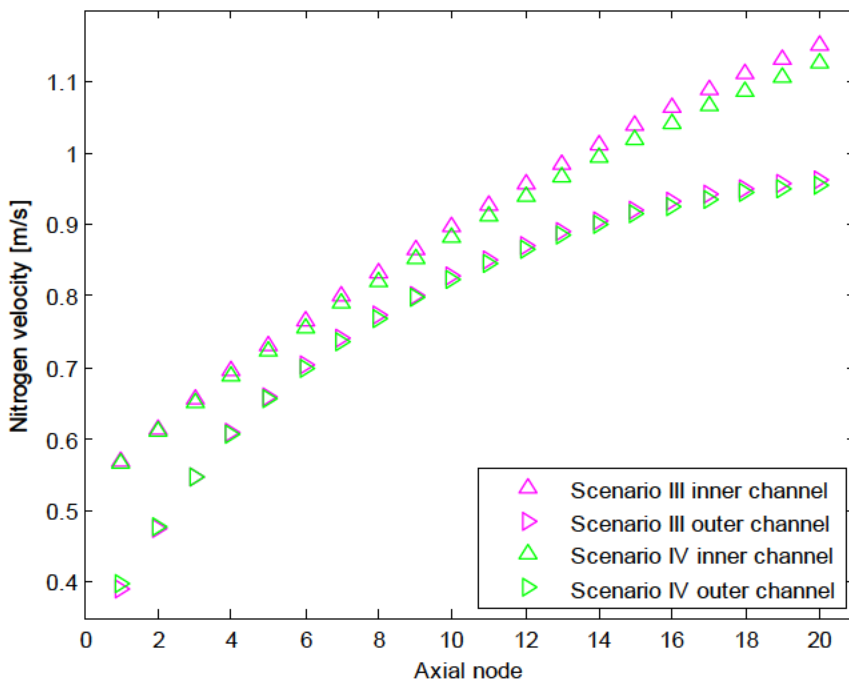


Figure 9-18: LOCA event scenario III & IV - nitrogen velocity at peak

Predicted coolant temperatures did not exceed 435 °C in the inner channel or 643 °C in the outer channel. No temperature limits were associated with the single-phase nitrogen coolant in this study due to its gaseous state. Coolant temperatures in the outer channel rose to values higher than those in the inner channel and rose at a faster rate. The coolant temperature profiles in Figure 9-15 and Figure 9-17 indicate increasing temperatures along the axial flow length. This temperature profile resulted in decreased cooling effectiveness at the topmost heat structure sub-volumes due to lower temperature gradients between the clad and coolant.

Predicted coolant velocities did not exceed 1.22 m/s in the inner channel and 0.98 m/s in the outer channel. Coolant velocity profiles indicate that a high degree of thermal expansion of the coolant occurred along the heated flow path. Coolant velocities in the outer channel were nearly twice those in the inner channel.

Predicted coolant mass flow rates did not exceed 0.00032 kg/s in the inner channel and 0.00012 kg/s in the outer channel.

CHF were not of concern to this analysis due to the lack of potential phase changes in the nitrogen coolant at the temperatures and pressures simulated.

9.4 Closing

This appendix examined the predicted results of a theoretical loss of coolant accident (LOCA) paired with an emergency reactor shutdown (SCRAM). In this postulated event, the OSTR is assumed to be continuously operating at a 1.1 MW steady-state power level, until a sudden leak in the OSTR's bioshield occurs. An immediate SCRAM is assumed to take place as a result of leak detection, which causes reactor power levels to drop according to the ANSI/ANS 5.1-2005 standard for Decay Heat Power in Light Water Reactors.

As stated in section 1.2, the most important parameters dictating the safety of a molybdenum element are (1) maximum fuel temperature, (2) maximum cladding temperature, and (3) critical heat flux (CHF) ratios during steady-state operation. In a non-steady-state system, the values of the maximum fuel temperature and maximum cladding temperature as functions of time are the two most important parameters.

Predicted maximum fuel temperatures during each of the LOCA event scenarios did not exceed 651 °C. This value is much larger in magnitude than that predicted for steady state conditions. This value is below the melting temperature of UO₂ referred to in Section 3.4 of 2856 ± 30 °C. Furthermore, it is below the technical specification limit of 1,150 °C [32]. The profiles of observed fuel material temperatures indicated that the reflood option proved to be effective at allowing axial heat transfer within the axial sub-volumes of the fuel material.

Predicted maximum clad temperatures during LOCA event scenario I did not exceed 651 °C. This value approached but did not exceed the melting temperature of aluminum referred to in Section 3.4 as 660 °C.

Predicted maximum clad temperatures did not exceed 615 °C, 598 °C, and 576 °C during LOCA event scenarios II, III, and IV, respectively. These values did not exceed the melting temperature of aluminum referred to in Section 3.4 as 660 °C.

The assumed atmospheric nitrogen temperature had a pronounced effect on the predicted fuel material temperatures during each LOCA event scenario. It should be noted that the assumed temperature of the nitrogen, 42 °C, within this study is higher than the average temperatures maintained within the OSTR bay, 15 °C to 32 °C, and higher the year-averaged temperature of Corvallis, Oregon, of approximately 11.5 °C.

The results from this conservative safety analysis study predicted safe maximum fuel temperatures and safe maximum clad temperatures for a molybdenum element

deployed within the OSTR hot channel at an integral power level of $1.1 \text{ MW}_{\text{th}}$ during a theoretical LOCA event.

10 APPENDIX B: FLOW BLOCKAGE ANALYSIS

10.1 Description

The predicted results of a flow blockage event are examined in this appendix. In this postulated event, the OSTR is assumed to be continuously operating at a 1.1 MW steady-state power level when an implemented molybdenum element becomes unable to transfer heat via its inner channel due to blockage. The inner channel is modeled as the blocked channel due to its larger flow area when compared to the outer channel. In addition, the selection of the inner channel for blockage approximates a more physically likely scenario given the geometry of the two flow channels.

10.2 Approach

During the blockage event, it is assumed that all mechanisms of heat transfer between the Molybdenum Element and the inner channel halt completely. This adiabatic boundary condition is modeled within RELAP by forcing the left boundary of the fuel material to read heat transfer rates from a general table. This table describes a heat transfer rate of zero (W/m^2) for all time periods considered.

No additional input changes are included in the simulation of this event, including any changes regarding the outer channel geometry or on the boundary condition between the fuel material and the outer channel. This modeling approach is used to simulate more limited mass flow rates in the outer channel as an alternative to allowing the outer channel to accommodate all possible coolant flow which could otherwise pass through the inner channel.

10.3 Results

Table 10-1 summarizes the determined results from the blockage event analysis in the manner described in Section 5.1.

Table 10-1: Blockage event results

| Steady-State Parameter | Inner Channel Value | Outer Channel Value |
|---|---------------------|---------------------|
| Maximum fuel temperature [°C] | 224.40 | |
| Maximum clad temperature [°C] | 224.40 | 126.09 |
| Minimum CHF _R – 2006 look-up table | -- | 7.93 |
| Minimum CHF _R – Bernath | -- | 4.84 |
| Minimum CHF _R – Hall-Mudawar | -- | 14.68 |
| Channel outlet flow rate [kg/s] | 0.0365 | 0.0833 |
| Channel outlet velocity [m/s] | 0.0663 | 0.2261 |
| Exit Bulk coolant temperature [°C] | 49.00 | 84.61 |
| Exit Bulk coolant pressure [kPa] | 147.35 | 147.32 |
| Maximum wall heat flux [kW/m ²] | 0.0 | 261.83 |

Table 10-1 indicates that more limiting thermal hydraulic parameters result from the blockage event than from the steady-state results presented in Table 5-1.

The predicted temperature of each heat structure sub-volume within the fuel material is dependent upon two key parameters: the internal source values in and around that sub-volume and the cooling effectiveness of the outer channel at the axial location of that sub-volume. The heat structure's left adiabatic boundary condition results in the development of increased fuel and clad temperatures at the left boundary. Predicted temperatures for each sub-volume within the fuel material heat structure are presented in Figure 10-1 and Figure 10-2. The axial and radial "hot band" temperatures are presented in Figure 10-3 and Figure 10-4.

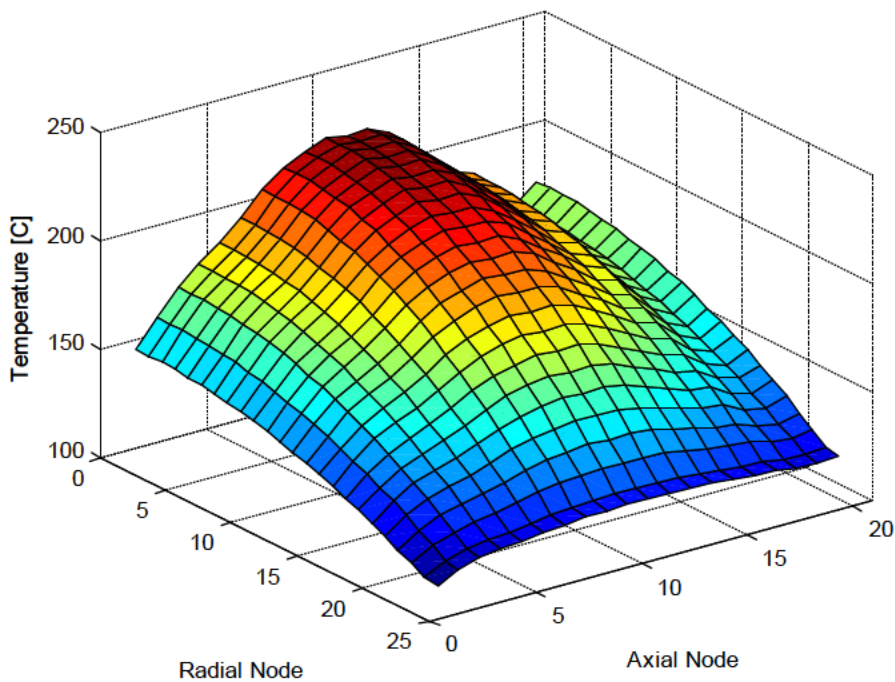


Figure 10-1: Blockage event - fuel temperature

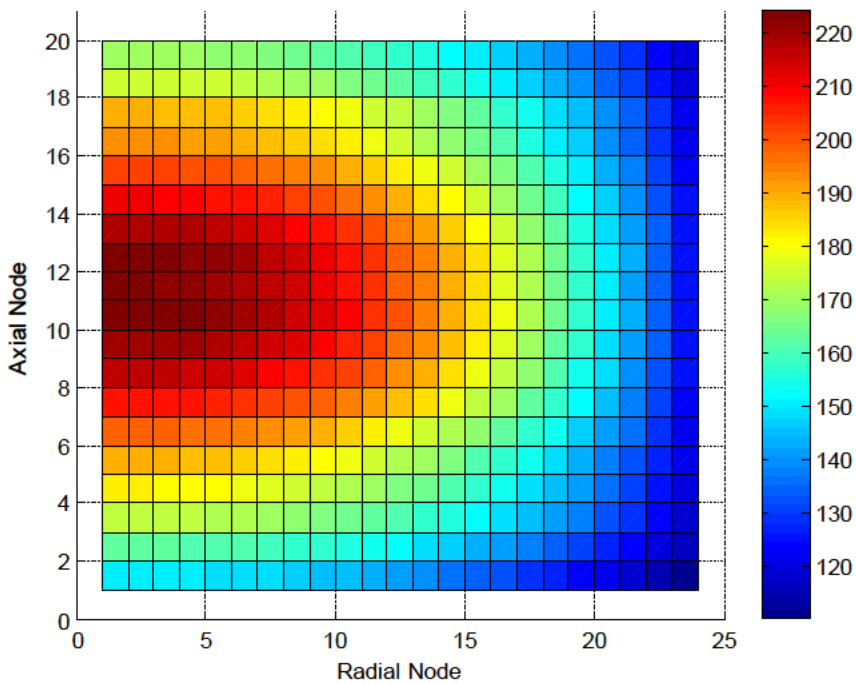


Figure 10-2: Blockage event - fuel temperature

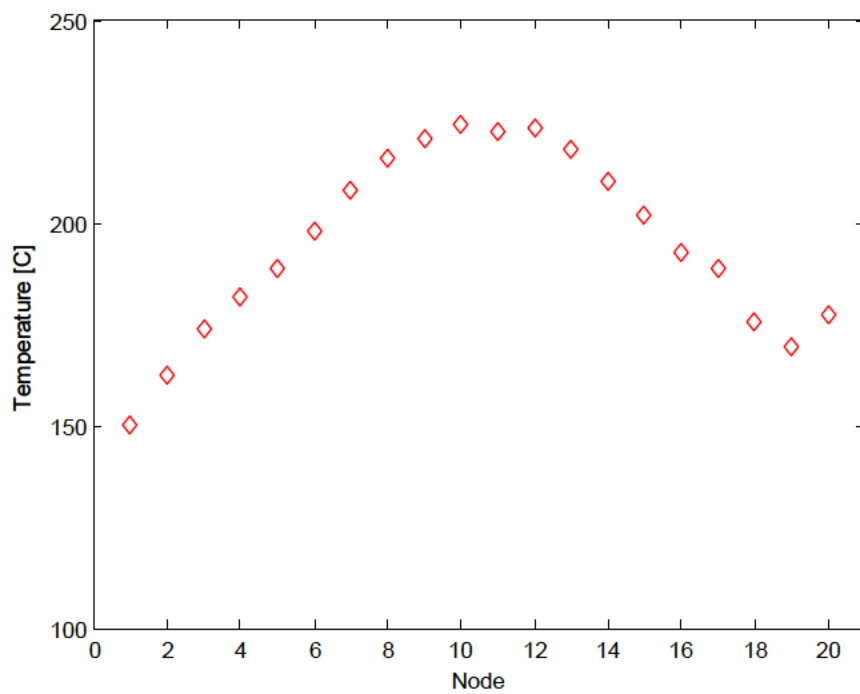


Figure 10-3: Blockage event - axial hot band

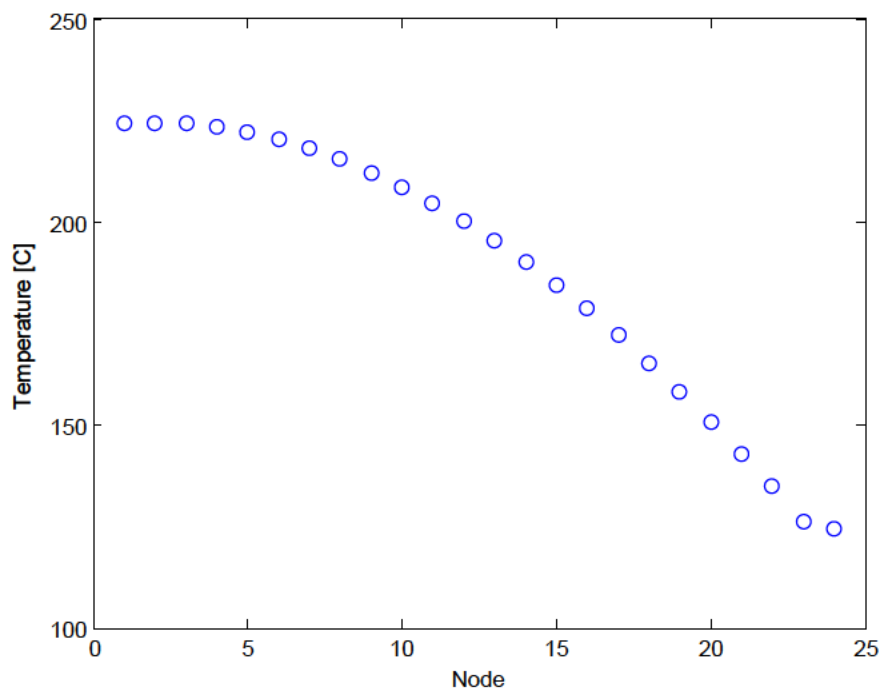


Figure 10-4: Blockage event - radial hot band

Predicted maximum fuel temperatures did not exceed 225 °C. This value is larger in magnitude than that predicted for steady state conditions, but well below both the melting temperature of UO₂ referred to in Section 3.4 as 2856 ± 30 °C. Furthermore, the predicted maximum fuel temperature is well below the OSTR technical specification limit of 1,150 °C [32].

Predicted maximum cladding temperatures did not exceed 225 °C. This value is larger in magnitude than that predicted for steady state conditions, but well below the melting temperature of aluminum referred to in Section 3.4 as 660 °C.

The predicted fuel material temperature profile presented in Figure 10-1 and Figure 10-2 indicate that maximum fuel and clad temperatures develop within sub-volumes at a location against the heat structure's left boundary and slightly above its axial centerline. The development of a "hot spot" at this location the unavailability of cooling at the heat structure's left boundary. This hot spot axial location is congruent with the molybdenum element axial source profiles presented in Section 4.4. Hot spot radial location is caused by the heat structure's adiabatic left boundary condition.

The cooling effectiveness provided to the molybdenum element clad sub-volumes is dependent upon the coolant properties in the outer channel at each hydrodynamic sub-volume. The coolant temperature and velocity profiles, presented in Figure 10-5 and Figure 10-6, respectively, display the coolant characteristics within the inner channel and the outer channel along the axial flow length.

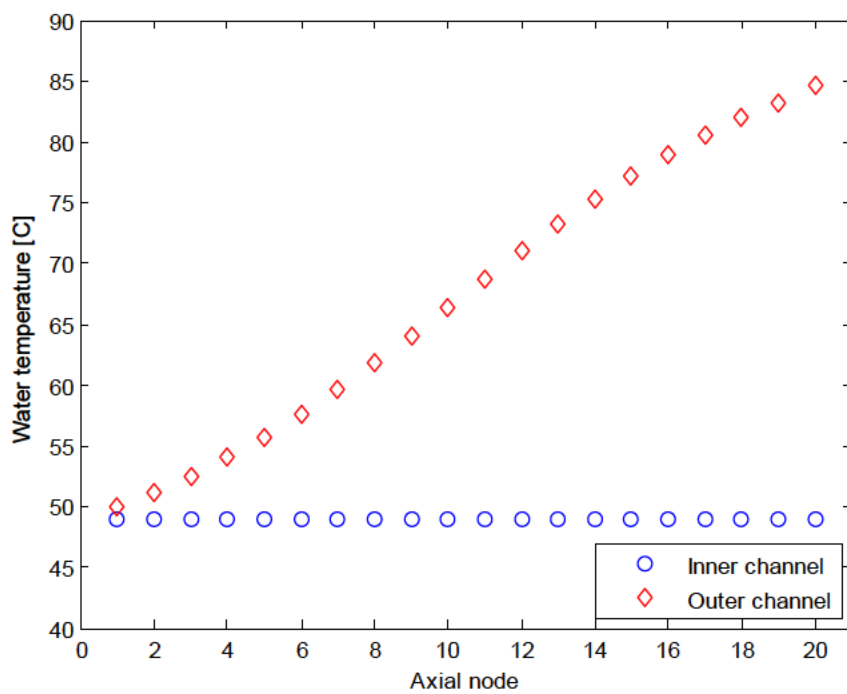


Figure 10-5: Blockage event - channel water temperature profile

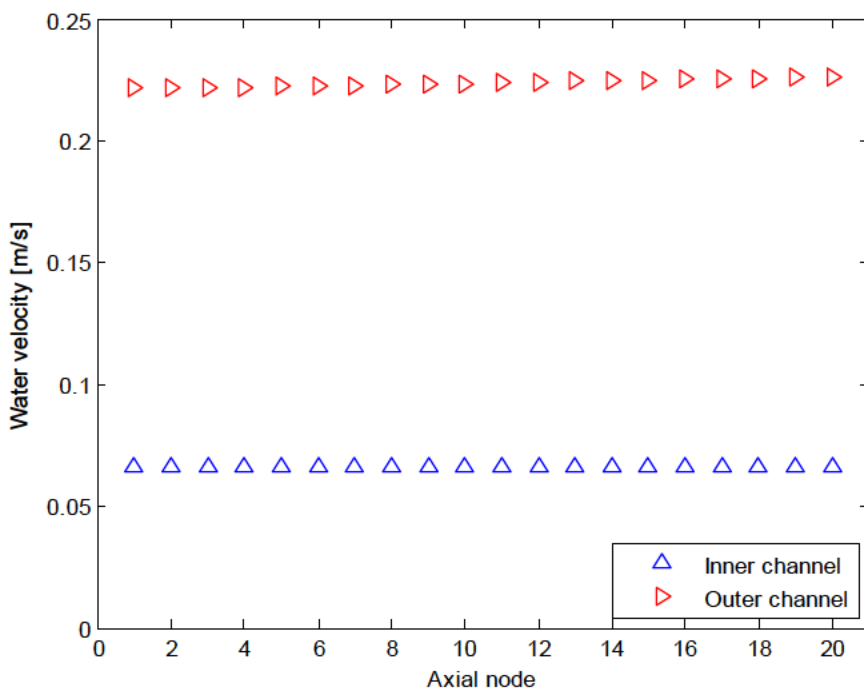


Figure 10-6: Blockage event - channel water velocity profile

Predicted coolant temperatures did not exceed 85 °C in the outer channel and did not vary from the inlet temperature of 49 °C in the inner channel. Coolant temperatures in the outer channel rose to values higher than those in the inner channel due to the adiabatic boundary condition between the inner channel and the fuel material.

Predicted coolant velocities did not exceed 0.23 m/s in the outer channel or 0.067 m/s in the inner channel. Coolant velocity profiles indicate that only slight thermal expansion of the coolant occurred within the outer channel along the axial flow length. Coolant velocities in the outer channel were more than 300% of those in the inner channel. The driving force established by natural circulation between the fuel material and the outer channel caused entrainment within the inner channel with magnitudes of nearly two-thirds of steady-state inner channel coolant velocities.

The areas of highest predicted heat flux appeared within the areas of highest predicted clad temperature at the heat structure's right boundary. Given that the coolant velocity and pressure within the outer channel remained relatively constant, heat flux and temperature variations along the axial flow length had a large contribution on the predicted CHF profiles presented in Figure 5-7.

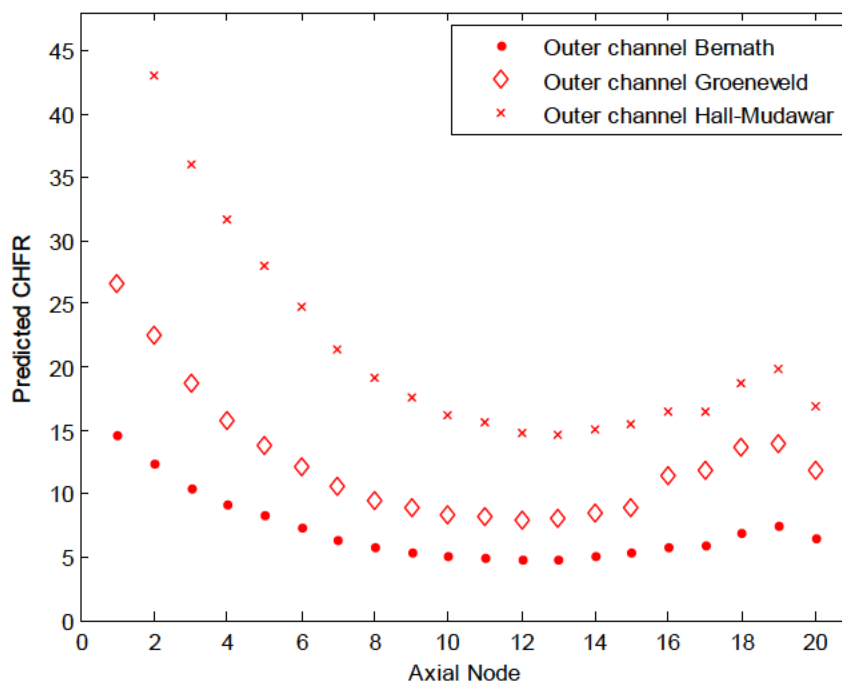


Figure 10-7: Blockage event - CHF

The most conservative predicted MCHF was 4.84 in the outer channel with the Bernath correlation. This minimum value is lower than that produced for the steady-state analysis but within safe margins. Predicted CHF profiles exhibited the same general trend visible in the steady state analysis presented in Section 5.1 wherein the most limiting values were predicted between the fuel material sub-volumes 10 through 14. Values from the Bernath and Groeneveld look-up table predicted more limiting CHF values than those predicted from the Hall-Mudawar correlation. This difference may be due to low mass velocities ($\text{kg/m}^2\text{-s}$) in the inner and outer channel which lie below the minimum value prescribed by the correlation.

CHF values within the inner channel were not of concern to this analysis due to the forced adiabatic boundary condition between the heat structure and inner channel.

10.4 Closing

This appendix determined and characterized the thermal hydraulic aspects related to a theoretical blockage event involving an implemented molybdenum element within the OSTR core at a 1.1 MW steady-state power level. Limiting thermal hydraulic parameters include (1) maximum fuel temperature, (2) maximum cladding temperature, and (3) critical heat flux (CHF) ratios during steady-state operation. This objective was accomplished using RELAP5-3D version 2.4.2 through the development of a model representative of a single molybdenum element within the OSTR using the most conservative flow channel geometry possible – the OSTR’s B ring “hot channel,” and a forced adiabatic boundary condition between the molybdenum element fuel material and the inner channel.

Predicted maximum fuel temperatures did not exceed 225 °C. This value is larger in magnitude than that predicted for steady state conditions, but well below the melting temperature of UO₂ referred to in Section 3.4 as 2856 ± 30°C. Furthermore, the predicted maximum fuel temperature is well below the OSTR technical specification limit of 1,150 °C [32].

Predicted maximum cladding temperatures did not exceed 225 °C. This value is larger in magnitude than that predicted for steady state conditions, but well below the melting temperature of aluminum referred to in Section 3.4 as 660 °C.

The most conservative predicted MCHFR was 4.84 in the outer channel with the Bernath correlation. This minimum value is well within safe margins and correlates with the safe implementation of molybdenum elements within the OSTR core during steady state core operation.

Values from the Bernath and Groeneveld look-up table predicted more limiting CHF_Rs than those predicted from the Hall-Mudawar correlation. This difference may be due to low mass velocities ($\text{kg/m}^2\text{-s}$) in the inner and outer channel which lie below the minimum value prescribed by the correlation.

Examinations of the RELAP5-3D outputs indicate that the high surface area to volume ratio of the molybdenum element design provides very effective heat transfer from the fuel material to the coolant even when the outer channel provides the only form of cooling. Higher mass flow rates and velocities are maintained within the outer channel than in the inner channel. This difference may be attributed to the larger form loss calculated for the inner channel as opposed to those calculated for outer channel and to the natural circulation driving force present only in the outer channel.

The results from this conservative safety analysis study predicted safe maximum fuel temperatures, maximum clad temperatures, and CHF_Rs for a molybdenum element deployed within the OSTR hot channel during a theoretical blockage event at an integral power level of $1.1 \text{ MW}_{\text{th}}$.